Order Number 1348498

Two-dimensional Navier Stokes simulations of instability waves in a flat plate boundary layer flow at $M = 4.5$

Gottmann, Matthias, M.S.

The University of Arizona, 1992

U·M·I
300 N. Zeeb Rd.
Ann Arbor, MI 48106

TWO-DIMENSIONAL NAVIER STOKES SIMULATIONS OF INSTABILITY WAVES IN A FLAT PLATE BOUNDARY LAYER FLOW AT $M = 4.5$

by
Matthias Gottmann

A Master Thesis Submitted to the Faculty of the
DEPARTMENT OF AEROSPACE AND MECHANICAL ENGINEERING
In Partial Fulfillment of the Requirements
For the Degree of
MASTER OF SCIENCE
WITH A MAJOR IN MECHANICAL ENGINEERING
In the Graduate College
THE UNIVERSITY OF ARIZONA

1 9 9 2

STATEMENT BY AUTHOR

This thesis has been submitted in partial fulfillment of requirements for an advanced degree at The University of Arizona and is deposited in the University Library to be made available to borrowers under rules of the library.

Brief quotations from this thesis are allowable without special permission, provided that accurate acknowledgement of source is made. Requests for permission for extended quotation from or reproduction of this manuscript in whole or in part may be granted by the head of the major department or the Dean of the Graduate College when in his or her judgement the proposed use of the material is in the interests of scholarship. In all other instances, however, permission must be obtained from the author.

SIGNED: M. Gottmann

APPROVAL BY THESIS DIRECTOR

This thesis has been approved on the date shown below:

Hermann Fasel — 5/7/92

H.F. Fasel
Professor of Aerospace
and Mechanical Engineering

Date

TABLE OF CONTENTS

LIST OF ILLUSTRATIONS

ABSTRACT

This thesis addresses the investigation of mechanisms involved in the transition from laminar to turbulent flow. The flow studied is a compressible flat plate boundary layer at a free stream velocity of $M = 4.5$. The two-dimensional compressible unsteady Navier Stokes equations are solved numerically in a rectangular region at a distance downstream from the leading edge. Disturbances are introduced by periodical suction and blowing through a slot in the wall. These disturbances propagate downstream in the flow field. At every point in the flow field the response of the flow is analyzed using a Fourier analysis in time. Results obtained are interpreted with reference to linear stability theory. One important result is the existence of multiple undamped waves for one wave frequency. The second important result demonstrates that an amplified wave of a certain frequency can generate disturbances at multiples of its frequency which may then be amplified more strongly.

VARIABLES AND SUBSCRIPTS

VARIABLES

x – streamwise coordinate

y – platenormal coordinate

L – reference length

t – time coordinate

u – streamwise velocity

v – normal velocity

ρ – density

T – temperature

p – pressure

e – internal energy

φ – any of the dependent variables

μ – viscosity

ϑ – heat conduction coefficient

Re – Reynolds number (with reference lenght)

Pr – Prandtl number

M – Mach number

$R = \sqrt{(\bar{u}_\infty \bar{\rho}_\infty \bar{x})/\bar{\mu}_\infty}$

a – speed of sound

α – wavenumber

ω – frequency

c_p – specific heat capacity for constant pressure

c_v – specific heat capacity for constant density

SUBSCRIPTS AND SUPERSCRIPTS

Shown for u:

$\bar{u}$ – dimensional value

u_∞ – freestream value

u' – fluctuation

u_0 – steady value

u_M – value at freestream boundary

u_N – value at outflow boundary

1 INTRODUCTION

One of the remaining issues to be resolved in the field of aerodynamics is the transition from laminar to turbulent flow. The transition has a crucial influence on aerodynamic and thermodynamic characteristics such as pressure coefficients, drag coefficients, and heat transfer. The influence of transition on these characteristics accounts for the relevance of this topic for technical application. However, certain fundamental questions must be answered. Specifically, researchers seek to understand where and why a particular flow changes from laminar to turbulent. Answers to such questions would enable them to predict flow patterns and to eventually influence the transition location.

There are many ways to approach such a problem. One can treat the problem as either a compressible or incompressible flow. In historic perspective, transition was first investigated for incompressible flows. As scientists progressed in their research, they began to extend their interest into the more complex realm of compressible transition. The following study investigates transition in a compressible flow.

Fast advances in compressible transition were made before 1970. Thereafter, due to reduced financial support for space projects, interest began to fade. However,

recent hypersonic space vehicle projects such as the American NASP have created a renewed interest in compressible boundary layer transition. Understanding of transition is now thought to be crucial to the realization of such projects. In order to come closer to the realization of hypersonic space vehicles one must be willing to abandon conservative assumptions concerning heat transfer in the boundary layer which would cause severe weight penalties. Only more detailed research on compressible boundary layer behavior, as performed in this thesis, allows to replace conservative assumptions with a more detailed knowledge.

For compressible flows experimental investigation of transition is very difficult. A huge technical effort is necessary to minimize unwanted disturbances and obtain meaningful results. Theoretical analysis on the other hand allows to study a flow situation where all influences are controlled by the chosen mathematical model. Within the field of theoretical analysis, there exist two ways in which researchers can approach problems of transition: linear stability theory and full Navier Stokes simulations. Both approaches regard transition as a stability phenomenon. The concept is to introduce disturbances into a laminar flow and to determine whether these disturbances are amplified or damped. Instability in this sense, is a necessary, but not a sufficient condition for transition. Linear stability theory makes use of an important simplification: It considers small sinusoidal disturbances. This assumption allows to compute stability properties for a variety of flows. However, the linear

stability theory suffers severe restrictions – the most prominent being the exclusion of the actual transition region, where disturbances are generally non-linear. Navier Stokes simulations allow to treat flow problems more general. For a Newtonian flow, that is where the continuum hypothesis is valid, the actual flow problem is described by the Navier Stokes equations. By solving the Navier Stokes equations it is possible to investigate the development of small and nonlinear disturbances. Therefore, Navier Stokes simulations have been chosen as the method of investigation for this project.

Studying compressible transition with full Navier Stokes simulations is a relatively new approach. This approach opens a vast research area where only little is known so far, but it has a tremendous potential.

2 PHYSICAL MODEL

This chapter gives a brief description of the physical model chosen to study compressible transition mechanisms. The flow configuration is a flat plate boundary layer. The research performed for this thesis was one of the first attempts to study compressible transition solving the full Navier Stokes equations. Therefore, the most basic configuration was chosen. The flat plate boundary layer geometry is relatively easy to model and there is a similarity solution that can serve as an initial guess for the computation.

The physical situation is reduced to two dimensions. Velocities in spanwise direction are therefore implicitly set to zero. This reduction is a deviation from many actual flow situations, but it allows to perform basic investigations and observe two-dimensional phenomena isolated from three-dimensional effects.

It is impossible to compute the complete flow problem of a compressible flat plate boundary layer flow with a resolution sufficient to study transition phenomena. Figure 1 shows the computational box located downstream of the leading edge which allows to focus the computational efforts on the probable transition region.

Disturbances have to be introduced to study the stability properties of the

flow. There are three common ways to create disturbances: They can be introduced at the inflow- or free stream boundaries of the computational box or at the wall. For this project a suction slot in the wall was chosen. Numerical experiments with disturbances superimposed on the inflow boundary were also conducted, but only to a small extent.

One of the key parameters of the physical model is the free stream Mach number. One fixed Mach number was chosen and kept throughout the work. The reasons why $M = 4.5$ was chosen can be explained by linear stability theory. The existence of a second instability region is one of the important features predicted by linear stability theory for a boundary layer flow. The second instability region can be observed starting at $M = 2.2$ and grows with increasing Mach number. At $M = 4.5$ there are two separate instability regions (figure 2), but above approximately $M = 4.6$ the neutral curves merge. Disturbances amplified in the two regions have different physical properties and different names; "first-" and "second mode waves". The conditions at $M = 4.5$, exhibiting the largest possible, yet clearly separated second mode region, are ideally suited for this purpose.

3 NUMERICAL FORMULATION

This chapter will provide an overview of the numerical formulation implemented in the code. A detailed discussion can be found in [3].

3.1 GOVERNING EQUATIONS

The unsteady flow over a flat plate at high Mach number is described by the unsteady compressible Navier Stokes equations, the energy equation and the continuity equation. These equations are used in conservative formulation with the variables ρ, ρu, ρv and ρe. The fluid is modeled as a perfect gas, a relation for the viscosity is obtained from Sutherlands law. All variables are nondimensionalized:

$$
\begin{array}{llllllll}
x = \bar{x}/L & u = \bar{u}/\bar{u}_\infty & T = \bar{T}/\bar{T}_\infty & \vartheta = \bar{\vartheta}/\bar{\vartheta}_\infty \\
y = \bar{y}/L & v = \bar{v}/\bar{v}_\infty & p = \bar{p}/(\bar{\rho}_\infty \bar{u}_\infty^2) & e = \bar{e}/\bar{u}_\infty^2 \\
t = \bar{t}\bar{u}_\infty/L & \rho = \bar{\rho}/\bar{\rho}_\infty & \mu = \bar{\mu}/\bar{\mu}_\infty
\end{array}
$$

$$
\begin{aligned}
Re &= (\bar{\rho}_\infty \bar{u}_\infty L)/\bar{\mu}_\infty \\
Pr &= (c_p \bar{\mu}_\infty)/\vartheta_\infty \\
M &= \bar{u}_\infty/\bar{a}_\infty
\end{aligned}
$$

The nondimensional equations are

$$\frac{\partial \mathbf{A}}{\partial t} + \frac{\partial \mathbf{B}}{\partial x} + \frac{\partial \mathbf{C}}{\partial y} = 0 \quad ,$$

with

$$\mathbf{A} = \begin{bmatrix} \rho \\ \rho u \\ \rho v \\ \rho e \end{bmatrix}$$

$$\mathbf{B} = \begin{bmatrix} \rho u \\ p + \rho u^2 - [\mu(4/3\ \partial u/\partial x - 2/3\ \partial v/\partial y)]/Re \\ \rho uv - [\mu(\partial v/\partial x + \partial u/\partial y)]/Re \\ u(\rho e + p) - \vartheta/N\ \partial T/\partial x - \tau_1/Re \end{bmatrix}$$

$$\mathbf{C} = \begin{bmatrix} \rho v \\ \rho uv - [\mu(\partial v/\partial x + \partial u/\partial y)]/Re \\ p + \rho v^2 - [\mu(4/3\ \partial v/\partial y - 2/3\ \partial u/\partial x)]/Re \\ v(\rho e + p) - \vartheta/N\ \partial T/\partial y - \tau_2/Re \end{bmatrix} ,$$

where

$$N = PrReM^2(\kappa - 1)$$

$$\tau_1 = \mu\left[u\left(\frac{4}{3}\frac{\partial u}{\partial x} - \frac{2}{3}\frac{\partial v}{\partial y}\right) + v\left(\frac{\partial v}{\partial x} + \frac{\partial u}{\partial y}\right)\right]$$

$$\tau_2 = \mu\left[v\left(\frac{\partial v}{\partial x}+\frac{\partial u}{\partial y}\right)+v\left(\frac{4}{3}\frac{\partial v}{\partial y}-\frac{2}{3}\frac{\partial u}{\partial x}\right)\right]$$

$$\begin{aligned} p &= \frac{\rho T}{\kappa M^2} \\ \kappa &= \frac{c_p}{c_v} = 1.4 \\ e &= c_v T + \frac{1}{2}(u^2+v^2) \\ \mu &= T^{3/2}\left(\frac{1+S_1}{T+S_1}\right) \\ S_1 &= \frac{110.4\text{K}}{\bar{\text{T}}_\infty} \\ Pr &= 0.71 \\ c_p &= 1.0049157 \end{aligned}$$

Below $\bar{T} = 110.4$K Sutherlands law is linearly extrapolated.

3.2 COMPUTATIONAL DOMAIN

Figure 1 shows the two-dimensional rectangular computational domain. The downstream length is in the range of 10–20 wavelengths of the expected wave. The height of the domain contains approximately two boundary layer thicknesses at the end of the domain. The suction slot is about one wavelength (of the expected wave) downstream of the inflow boundary and has a width of about one wavelength.

3.3 BOUNDARY CONDITIONS

The steady baseflow is computed using the unsteady code with slightly different boundary conditions, and using a similarity solution as initial guess and iterating until convergence is reached. This baseflow is the initial condition for the unsteady computation. The convergence criterion for the baseflow is a change of less than 10^{-6} of all flow variables within 1000 iterations.

3.3.1 BOUNDARY CONDITIONS FOR BASEFLOW ITERATION

Inflow Boundary: u, v, T and ρ are held constant at the similarity solution values. For the pressure, which is not contained in the similarity solution

$$\frac{\partial p}{\partial x} = 0$$

is prescribed.

Plate Surface: Impermeable, adiabatic wall:

$$u = 0$$

$$v = 0$$

$$\frac{\partial T}{\partial y} = 0$$

$$\begin{aligned}\frac{\partial p}{\partial y} &= -\frac{\partial(\rho v^2)}{\partial y} \\ &+ \frac{1}{Re}\left\{\frac{\partial}{\partial x}\left[\mu\frac{\partial u}{\partial y}\right] + \frac{\partial}{\partial y}\left[\mu\left(\frac{4}{3}\frac{\partial v}{\partial y} - \frac{2}{3}\frac{\partial u}{\partial x}\right)\right]\right\}\end{aligned}$$

Outflow Boundary: For all variables we use

$$\frac{\partial^2 \varphi}{\partial x^2} = 0 \quad ,$$

where

$$\varphi = \{u, v, T, p\}$$

Free Stream Boundary:

$$\begin{aligned}\frac{\partial u}{\partial y} &= -\alpha_M\sqrt{1 - M^2(1-c)^2}\,(u-1) \\ \frac{\partial v}{\partial y} &= 0 \\ \frac{\partial T}{\partial y} &= -\alpha_M\sqrt{1 - M^2(1-c)^2}\,(T-1) \\ \frac{\partial \rho}{\partial y} &= -\alpha_M\sqrt{1 - M^2(1-c)^2}\,(\rho-1)\end{aligned}$$

where α_M is the wavenumber of the expected wave for the unsteady computation and c is the phase velocity.

3.3.2 BOUNDARY CONDITIONS FOR UNSTEADY COMPUTATION

Initial Condition: as initial condition we use the converged solution of the base-flow iteration.

Inflow Boundary: All disturbances and its derivatives are set to zero

$$\varphi' = 0 \quad ,$$

where

$$\varphi' = \{u', v', T', p'\}$$

Plate Surface (at Suction Slot):

$$\begin{aligned}
u' &= 0 \\
v' &= f(x)\sin\omega t \\
T' &= 0 \\
\frac{\partial p}{\partial y} &= -\frac{\partial(\rho v^2)}{\partial y} + v\frac{\partial \rho v}{\partial y} - \rho\frac{\partial v}{\partial t} \\
&+ \frac{\partial}{\partial x}\left[\frac{\mu}{Re}\left(\frac{\partial u}{\partial y} + \frac{\partial v}{\partial x}\right)\right] + \frac{\partial}{\partial y}\left[\frac{\mu}{Re}\left(\frac{4}{3}\frac{\partial v}{\partial y} - \frac{2}{3}\frac{\partial u}{\partial x}\right)\right]
\end{aligned}$$

$f(x)$ is a 5^{th} order polynomial shown as in figure 3. This distribution guarantees that no mass is added to or subtracted from the boundary layer. The temperature fluctuation is set to zero as the wall has a finite heat capacity and the fluctuations have a high frequency.

Plate Surface (away from Suction Slot):

$$
\begin{aligned}
u' &= 0 \\
v' &= 0 \\
T' &= 0 \\
\frac{\partial p}{\partial y} &= -\frac{\partial(\rho v^2)}{\partial y} \\
&+ \frac{1}{Re}\left\{\frac{\partial}{\partial x}\left[\mu\frac{\partial u}{\partial y}\right] + \frac{\partial}{\partial y}\left[\mu\left(\frac{4}{3}\frac{\partial v}{\partial y} - \frac{2}{3}\frac{\partial u}{\partial x}\right)\right]\right\}
\end{aligned}
$$

Outflow Boundary: For all variables

$$\frac{\partial^2 \varphi'}{\partial x^2} = -\alpha_N^2 \varphi'$$

where

$$\varphi' = \{u', v', T', p'\}$$

is used. This condition caused relatively small reflections from the outflow boundary.

Free Stream Boundary: For all variables

$$\frac{\partial \varphi'}{\partial y} = -\alpha_M \sqrt{1 - M^2(1-c)^2}\, \varphi'$$

$$\varphi' = \{u', v', T', \rho'\}$$

with predicted wavenumber α_M and phase speed c is used. The basic idea is that the fluctuations decay exponentially in y-direction.

3.4 DISCRETIZATION

The equations are solved on an equally spaced rectangular grid. In time, a modified MacCormack scheme is applied. Modifications were made with regard to accuracy, where the scheme was modified such that it is 4^{th} order accurate in space and only convective terms in y-direction are approximated with one sided alternating differences. The sequence of the one sided differences alternates from step to step. This means in one step, the first half step is discretized with "upwind" and the second with "downwind" differences and vice versa in the next step.

All space derivatives are approximated by 4^{th} order central differences. The wall boundary is treated with 5^{th} order accurate differences while all other boundary conditions are discretized with second and first order accurate approximations.

4 INPUT/OUTPUT SYSTEM (IOS)

An essential requirement for computational fluid dynamics is postprocessing software. At the University of Stuttgart where the Navier Stokes code was developed, a complete system of libraries and utilities exists for this purpose. Unfortunately, this software is specifically tailored to the local Cray2 and only a small portion can be implemented on machines available at the Aerospace and Mechanical Engineering Department at the University of Arizona. The section which can be transferred is the input/output interface fortran library in a version suitable for any standard fortran compiler. The performance of these routines on a Sun4 workstation was not satisfactory; with data files of several megabytes, as they occur in this project, access to data may take up to several minutes and the storage requirement of those formatted files is four times as large as the optimal binary format.

Encouraged by colleagues who faced the same situation, a new input/output system including postprocessing software was developed. Hubert Meitz, also a student at the Aerospace and Mechanical Engineering Department contributed to this part of the project. From now on this input-output system will be referred to as IOS.

4.1 IOS FORTRAN LIBRARY

The fortran library is the core of the system. It provides all necessary routines to read and write data from fortran programs. As mentioned before the main goals of the IOS are to improve speed and storage requirements. As this project started from scratch, an optimal solution with regard to data access time and storage requirement was attempted. Many basic features of the system from Stuttgart are included as they proved to be efficient. In addition to speed and storage optimisation, portability, at least for three mainly used machines Sun Vax and Convex, was a major concern.

The key decision is the choice of the write format. Typically, CFD data are given at certain time levels for certain parameters in one-, two- or three dimensional arrays. The most sophisticated and promising data access is binary and direct access as opposed to formatted writing and sequential access. Unfortunately binary files are a priori not portable between different machines and direct access requires block size specification which is also machine dependent. Abandoning the concept of only one file format and including conversion programs, it is possible to avoid sacrificing the big advantages of binary direct access files to a simpler solution. To read a direct access file, the record length has to be known before the first access. On the other hand, the record length depends on the characteristics of the data to be

read. To circumvent this difficulty and provide readability of essential information, even for binary files, the data is split into two files. One file is written formatted with sequential access and it contains only global information, like the number of time steps, number of parameters, dimensions of array and eventually user specified comments. In a second file the actual data is stored and for this one several formats are available. As a naming convention the user supplies the basic filename without an extension and IOS creates or reads first the so called "control data" file with the global information and the extension ".cd" and then the actual file with a file type dependent ending.

One of the parameters deciding the format of binary output is the calling program internal data representation. For general application the variables are either represented by real*4 or real*8 arrays. The binary files are marked with a 4 or 8 accordingly.

The following file types, given by their extension, are implemented:

- .s4 .s8 Sun binary format (IEEE standard) direct access files with record length limited to sun fortran specifications
- .c4 .c8 IEEE binary format direct access files with unlimited record length as used in convex fortran
- .v4 .v8 vax binary format direct access files with record length limited to VMS

fortran standards

- .fm formatted sequential access files
- .ea format compatible to the the one used in Stuttgart, called EAS

In practical use .s8 turned out to be most convenient, as this format is portable between Sun and Convex. The .fm is necessary for file transfer to a Vax machine and to make data readable.
Standard procedure to read or write is to call "readcd" or "writecd" once to transfer global informations and have one or multiple calls to "readd" or "writed" for the actual data.

In addition to these IOS formats there are subroutines included in the library which use the NASA-Plot3d definitions. They are built around existing C-routines with fortran interfaces. A detailed description of the IOS usage is installed on the Sun workstations and can be read calling "man ios".

The coding effort to use IOS can be bigger than applying simpler "write" statements. Nevertheless it has already gained popularity because of the standardization and reliability it provides.

4.2 IOS UTILITIES

A number of essential post processing programs for IOS files have been developed. The development was motivated by the needs of the Navier Stokes computations in this thesis. Nevertheless, an effort was made to make the utilities as versatile and general as possible, while keeping the user interface simple and self guided. All programs have a UNIX interface between the user and the actual executable, handling different modes of operation and providing certain default files. Output media for the black and white plotting programs is the screen, a printer or a postscript file.

4.2.1 TRANSFORM AND CUT FILES (IOSCUT)

Ioscut is a program to cut and copy IOS data. It can read any of the IOS formats, manipulate data, by means of choosing certain time steps or parameters or cut out parts of an array and write any IOS format independent of the input. Therefore it can handle file type conversion. To minimize user input a menu type selection with defaults for all parameters is implemented. Ioscut can be used interactively as well as as batch job.

4.2.2 COMBINE DATA FROM MULTIPLE FILES (MERGE)

Merge combines certain parameters and time steps from multiple input files to one output file. All in- and output files are handled separately and therefore different file types can be used. The problem of combining arrays with different dimensions is solved by taking the largest value of each dimension of all input files for the output file. The user interface is simple with the disadvantage of being unable to recover from mistakes made by the user.

4.2.3 SAMPLE DATA ALONG LOCAL MAXIMA (MAXLINE)

Maxline is a program to sample data along a local maximum in one grid direction of a two-dimensional array. Every column is searched for up to 10 local maxima and the values at those points are stored as one line. E.g. all first local maxima form one line as well as all second maxima etc.. This utility is rather specific for postprocessing Fourier analysis of two-dimensional CFD-data and no attempt has been made to write it more general.

4.2.4 LINE PLOTTING UTILITY (IOS2D)

Ios2d is the line plotting program for IOS data. Data can be plotted along grid lines or sampled diagonally in the array. Each coordinate axis is handled separately to allow plotting of one parameter versus another one. For the special case of constant intervals, the program can generate the values for one axis. There is a switch in the program to plot phase data normalized between $-\pi$ and π unnormalized and continuously. The subroutine involved was provided by Peter Dittrich. The program is designed to plot up to 10 curves and up to 500 points per curve. These limits can be altered, but the code needs to be recompiled. As opposed to most other IOS utilities, ios2d is controlled by a fixed format input file instead of interactively. This concept was chosen because of the variety of parameters needed and a lack of reasonable default values. The only interactive choice is the output medium. This choice can be circumvented with the appropriate calling parameter. The default plot format is read from an external file. The user has the option to create his own default file and tailor plot size and appearance to his specific needs.

4.2.5 SURFACE PLOTTING UTILITY (IOS3D)

Ios3d plots data given in a two-dimensional array in an IOS file as a surface in three-dimensional perspective. It is especially tailored for comfortable interactive use with features like self guided menus. Presentation includes a hidden line algorithm. The plot format is read from an external file and as for ios2d, the user has the option to create his own format file.

4.2.6 CONTOURING UTILITY (CONTOUR)

Contour computes and plots lines of constant values, so called contour lines, from two-dimensional data. It offers three different modes to generate the contour levels to be plotted:

- place a user specified number of values equally spaced between the minimum and maximum of the array.
- generate a specified number of equally spaced contour values starting with a value given by the user.
- read the contour values from an external file.

The user interface is menu guided. The information about the plot format is read from an external file and can be changed by the user.

4.2.7 COLOR CONTOURING UTILITY (COLCON)

Colcon can represent two parameters by contouring in one plot. One parameter is shown by color shading the plotting domain, the other by contour lines. The essential graphic routines were coded by Uli Rist from the University of Stuttgart. Hubert Meitz and the author adapted the code to IOS data and added features like the possibility to save the picture as a screendump file. The program is controlled by a fixed format input file.

4.2.8 COLOR SURFACE UTILITY (IOSC3D)

This program has two possibilities to represent data from two dimensional arrays. The data are plotted as a surface in three dimensions and colors can be used to show values. This offers the opportunity to display two parameters in one picture. In practical use, pictures are much easier to interpret if only one parameter is used for the surface and the colors. The basic code was again written by Uli Rist. The program is controlled by a fixed format input file, but there is an interactive interface to change viewpoint, zoom and get screendumps.

5 RESULTS

5.1 SECOND MODE, COARSE GRID COMPUTATION (FIRST CASE)

The computational domain of this calculation relative to the instability regions is shown in figure 4. This case should show the second mode characteristics: a pronounced phase jump of the pressure in y-direction and a strong amplification. The specifications for case 1 are the following:

Integration Domain:				
inflow boundary		R	=	1500
outflow boundary		R	=	1900
number of grid points:	in x-direction	mx	=	341
	in y-direction	ny	=	81
grid spacing:	in x-direction	Δx	=	0.04
	in y-direction	Δy	=	0.006
grid points per wavelength in x-direction		mx_{wave}	=	12
Disturbance Input:				
amplitude of v at slot		$v_{\max}$	=	0.04
frequency of disturbance $(\bar{\omega}\bar{L})/\bar{u}_\infty$		ω	=	12
time steps per period of disturbance		mt	=	200
free stream temperature		$\bar{T}_\infty$	=	61.1 K

The chosen resolution is required to guarantee convergence of the baseflow. Another consideration is to be able to provide enough data for a Fourier analysis of the data. Only three Fourier modes were determined here and the second consideration was not as restrictive as the first. *Fourier analysis* refers to a Fourier decomposition of the signal at every grid point over one period of the disturbance.

Figures 5 to 8 show the baseflow in the entire domain. Remarkable is the weak shock seen in the v-velocity (figure 6) and pressure (figure 8) near the left boundary. This is due to the left boundary condition, which is not an actual Navier Stokes solution. The variation in pressure in the domain is very small and might be caused by the weak shock from the left boundary.

Figures 9 to 12 show the fluctuations for $t = const.$ at the end of the computation. Qualitatively the two second mode characteristics mentioned at the beginning of this chapter can be seen. Especially T shows a strong amplification. The phase jump in y-direction can be seen in the pressure plot. A grid line that starts at a wave crest at the wall ends off the peak at the free stream boundary. The behavior of these two properties becomes even clearer when looking at the Fourier components. Figures 13 to 16 show the spatial development of the Fourier components of the fluctuations.

Not shown are the zeroth harmonics which are almost identical to the baseflow and the higher harmonics which are more than one order of magnitude smaller. This indicates linear behavior. Figure 17 shows the phase angle over y as obtained from

the Fourier analysis.

This first calculation was used to demonstrate how the disturbance input affects the flow field. Figures 18 and 19 show contour plots of the pressure fluctuation, one from the Fourier analysis and one from the instantaneous signal. The instantaneous signal shows "bubbles" of high and low pressure starting from the slot all the way to the edge of the domain. Unfortunately it was not possible to mark positive and negative values unambiguously, however color plots clearly identify those bubbles as consecutive highs and lows. The plot from the Fourier analysis shows the path these "bubbles" travel. The straight part of this path in the outer flow region has almost exactly the Mach angle for $M = 4.5$. To better understand the nature of the "bubbles" one can consider the suction slot a source of disturbances in a unidirectional $M = 4.5$ flow field. This is a valid model for the region outside the boundary layer. Weak disturbances, such as sound waves, generated by the source, propagate within an envelope formed by the Mach cone.

Using the NASA PLOT3D and GAS graphic software it was possible to create an animation of the unsteady solution. This animation verified that the "bubbles" travel along the Mach line out to the free stream boundary.

Assuming that after some time the flow response in the integration domain is periodic, using contour plots of the outer flow region such as figure 20, the traveling speed of the structures within the shock could be determined. It turned out to be

$0.997\bar{u}_\infty$, which was not expected, as a sound wave would propagate along the same path with $\cos\Theta\bar{u}_\infty = 0.97\bar{u}_\infty$, where Θ is the Mach angle. In an attempt to check if the waves are acoustic waves the vorticity fluctuation was computed and plotted in figures 21 to 23. An acoustic wave is longitudinal by nature and would not create vorticity, while an instability wave has transversal components generating vorticity. Figure 21, showing the vorticity of the fluctuations in the entire domain, is dominated by wall vorticity as expected for instability waves in a boundary layer. Filtering out this high vorticity region close to the wall figure 22 was obtained. Within the boundary layer vorticity generated by the instability waves can be detected. To trace the question of the physical nature of the "bubbles", the region within the dashed rectangle was examined. This rectangle is the same part of the domain that was used to determine the wave speed (figure 20). There is no vorticity visible within the dashed box, hence this region has been magnified and plotted in figure 23. There is vorticity in figure 23, but it is one order of magnitude less than in figure 22. A possible explanation for the weak vorticity can be found with the model of acoustic waves propagating enveloped by a Mach cone. Acoustic waves in a stagnant fluid do not create vorticity. In the present case they propagate into a supersonic flow field and form a shock. If a shock is infinitely weak, it does not create vorticity. A shock of finite strength does create vorticity. The shock that occurs in this computation is weak, because it follows "almost" exactly the Mach angle. "Almost" means the shock is a real flow phenomenon and cannot be ideal.

Therefore, the shock cannot be infinitely weak. However, this argument partly contradicts the idea of examining vorticity to explain the nature of the "bubbles". There is vorticity in the "bubble" region, but it is not necessarily an indication of instability waves. The vorticity is very weak and could as well be explained by the presence of the shock. Therefore, the physical nature of the "bubbles" is not yet completely clarified.

In the beginning of this work it was not clear if the free stream boundary conditions are able to absorb the shock waves. Reflections were expected, but could not be found. Variable scaling of contour lines for the first harmonic of p (figure 24) finally verified the existence of a reflection. Careful inspection shows even a second reflection from the wall. It should be noted that in figure 24 extremely narrow scaling was necessary, thus this effect is small. It is obviously too small to affect the amplification rate of the waves, as no change can be observed in the vicinity of the reflection.

A problem with the introduction of disturbances by blowing and suction is, that the front of the shock wave formed by the envelope of the "bubbles" can become a noticeable shock (as opposed to "weak") and might alter the boundary layer as the disturbances become stronger. Therefore, an alternate way of disturbance input was implemented. The integration domain is cut in y-direction approximately two

wavelenghts downstream of the suction slot. The area downstream of the cut is used for further computations. At the new inflow boundary sinusoidal fluctuations as obtained from a computation with the full length domain are superimposed to the baseflow profiles. This strategy did not fulfill the expectations. This was possibly due to the fact that only the first harmonic of the Fourier analysis for the sinusoidal disturbance input at the inflow boundary was used which is not a solution of the Navier Stokes equations. The flow reacts with a weak shock from the left boundary into the field (figure 25). Increasing amplitudes will increase the strength of this shock, thus altering the boundary layer.

Decreasing the step size of this case to $\Delta y = 0.003$, yet keeping the size of the integration domain, altered the computed amplitudes considerably. The qualitative behavior remained unchanged. Research conducted in Stuttgart indicates that step sizes not larger than $\Delta y = 0.002$ are required for quantitative accuracy. Using such a small stepsize for the same computational domain results in prohibitive computing times. Therefore, a new computational domain was chosen for further work. The results discussed so far were checked on the refined grid ($\Delta y = 0.003$) and proved to be unchanged.

5.2 SECOND MODE, FINE GRID COMPUTATION (SECOND CASE)

The second case is based on tighter restrictions than the first one. The goal was to use a step size small enough to obtain accurate results. The computation time of the baseflow presented a restriction on the maximum size of the integration domain. The minimum length of the domain is ten wavelengths in order to be able to observe the spatial development . At the beginning of the computations for this second case it was still planned to utilize the inflow boundary disturbance input as described in the previous chapter. Thus, the length of the domain was extended to 15 wavelengths to get a starting solution. 15 wavelengths, each divided into 16 intervals to meet increased accuracy requirements, resulted in 241 grid points in x-direction. With an estimate for the computing time per grid point and time step obtained from case 1 a maximum of 121 grid points in y-direction was chosen. With given number of grid points, $\Delta y = 0.002$ (see end of previous chapter) and the condition to capture two boundary layer thicknesses at the end of the domain, the outflow boundary can be no further downstream than $R = 1000$. Applying these restrictions, case 2 is located such that it lies completely within the second mode unstable region.

Integration Domain:				
inflow boundary		R	=	780
outflow boundary		R	=	1000
number of grid points:	in x-direction	mx	=	241
	in y-direction	ny	=	121
grid spacing:	in x-direction	Δx	=	0.017
	in y-direction	Δy	=	0.002
grid points per wavelength in x-direction		mx_{wave}	=	16
Disturbance Input:				
amplitude of v at slot		$v_{\max}$	=	$.0004 \div .11$
frequency of disturbance $(\bar{\omega}\bar{L})/\bar{u}_\infty$		ω	=	22
time steps per period of disturbance		mt	=	300
free stream temperature		$\bar{T}_\infty$	=	61.1 K

The amplitudes at the suction slot varied from $v_{\max} = 0.0004$ to $v_{\max} = 0.11$ to demonstrate how the flow responds, when the fluctuations are no longer small and therefore the behavior is no longer linear. The highest value for $v_{\max}$ is the maximum for which the algorithm converges.

For the maximum input amplitude the zeroth harmonic is plotted in figures 26 and 27. For small fluctuations the zeroth harmonic is indistinguishable from the base-flow. In figure 26 there is a slight distortion of u near the suction slot. For T (figure 27) the distortion is more severe and visible over the whole length of the domain. For brevity only u and T for the minimum and maximum input disturbance amplitude are shown in figures 28 to 39. For both, minimum and maximum input

amplitude, the first to third harmonic of the Fourier analysis are presented.

Looking at the first harmonic of T at $v_{\max} = 0.11$ (figure 31), a fluctuation of 50% of the free stream value is reached and comparing with figure 30 ($v_{\max} = 0.0004$) a saturation can be observed. The amplification at the end of the domain is considerably smaller than in the linear case. For u (figures 28 and 29) this effect is less obvious, due to the lower amplitude (only 10% of the free stream value), but it can still be detected.

At the lower amplitude level the second and third harmonic are dominated by numerical noise (figures 32,36,34,38). The spikes might be caused by the jump in the second derivative of μ at 110K. At the maximum level the second and third harmonics of the temperature have already reached saturation (figures 35,39). In order to demonstrate that the low amplification at the end of the domain in figure 35 is a sign of saturation, a plot at an intermediate amplitude level (figure 40) is included.

There is a slight modulation visible in the first harmonic of u and even more in the first harmonic of p at the wall. Figures 41 and 42 show this effect at a linear and a nonlinear amplitude level. The oscillations of the amplitudes are present in both plots in the whole domain. In figure 41, starting from approximately grid line 100, the modulation is constant while the mean amplitude is increasing. For the nonlinear fluctuation level (figure 42), the growth of the mean amplitude is

decreasing towards the end of the domain, which is an indication of saturation. The presence of modulation indicates that there are two waves with the same frequency but different wavelength present. The fact that the modulation is constant while the mean amplitude is increasing suggests that one wave is amplified, the other nearly neutral. The interaction of two waves with the same frequency will be discussed later in connection with case 3.

Figures 43 to 58 show Fourier analysis amplitudes and phases of u, v, T and p over y for the minimum and maximum input amplitude level at an x-location corresponding to the the 180^{th} of 241 lines of the computational grid (left boundary is first grid line). Higher harmonics are included only in the phase angle plots for the maximum input amplitude level. All amplitude level plots are normalized by the maximum local amplitude. The small wiggles occurring at the lower input amplitude level ($v_{\max} = 0.0004$) are due to numerical noise. Comparing the amplitude level signals of u, v, T, and p between the minimum and maximum input amplitude level reveals only small changes, although the the input level differs by almost three orders of magnitude. For u (figures 43 and 44) the local minimum moves to lower amplitude values for higher input levels. v (figures 45 and 46) remains qualitatively unchanged. For T the shape of the second local maximum changes slightly, and for p the amplitude difference between the first local minimum and maximum gets larger with larger input amplitude levels. These changes are relatively small compared to

what can be observed in figures 51 and 52. The phase angle of the first harmonic of u changes drastically between the two input amplitude levels. The comparison of the phase angles at the minimum and maximum input amplitude levels for v, T, and p (figures 53 to 58) reveals only minor changes.

5.3 FIRST MODE COMPUTATION (THIRD CASE)

The main parameters for case 3 where selected to meet the same restrictions as in case 2, except that here the integration domain is chosen to be inside the first mode instability region. The parameters are:

Integration Domain:				
inflow boundary		R	=	530
outflow boundary		R	=	1000
number of grid points:	in x-direction	mx	=	241
	in y-direction	ny	=	121
grid spacing:	in x-direction	Δx	=	0.028
	in y-direction	Δy	=	0.002
grid points per wavelength in x-direction		mx_{wave}	=	16
Disturbance Input:				
amplitude of v at slot		$v_{\max}$	=	$.0004 \div .125$
frequency of disturbance $(\bar{\omega}\bar{L})/\bar{u}_\infty$		ω	=	12
time steps per period of disturbance		mt	=	300
free stream temperature		$\bar{T}_\infty$	=	61.1 K

Figures 59 to 62 show the first harmonic of the amplitude level of u and T for the minimum and maximum amplitude level. For u (figures 59 and 60) the surface plots are qualitatively similar. The only prominent difference is the height of the "humps" compared to the shock amplitude. The second local maximum of T at $v_{\max} = 0.0004$ (figure 61) is weakly amplified, while it is almost neutral at

$v_{max} = 0.125$ (figure 62). A surprise is the development of the second harmonic. At $v = 0.0004$ it is two orders of magnitude lower, but more amplified than the first harmonic at least in parts of the domain (figures 63,65). The possible explanation for this is simple and striking: The second harmonic represents a wave with a dimensionless frequency $\omega = 24$. For this particular domain the wave with the double frequency is in the second mode instability region (figure 4, slightly left of the $\omega = 22$ line). To support this explanation figures 67 to 72 show a comparison of the amplitudes and phases over y for an x-location equivalent to the 180^{th} grid line between the second mode wave from case 2 (first harmonic) and the first and second harmonic of case 3. The phases and amplitudes of the 1st harmonic of case 2 (second mode) resemble those of the second harmonic of case 3 at high and low amplitude levels. For brevity, only one fluctuation level is presented. $u(y)$, $v(y)$, $T(y)$ and $p(y)$ are plotted for $v_{max} = 0.0004$. For the phase plots, the high amplitudes had to be used, as the phase signal of higher harmonics in the small amplitude range is dominated by random noise. The phase angles of u and v change with increasing input amplitudes and do not enable a support of the given explanation. Therefore, a comparison of the phase angles of u and v is not explicitly shown.

In figures 63 and 65, in the last third of the domain, the waves propagate nearly neutrally, indicating the end of the instability region. An exception is the second maximum of T which is amplified throughout the domain. This different behavior is not unusual as the location of the neutral curve depends on the criterion used

[4]. Thus for the second maximum the neutral location may be different than for the first maximum.

With the explanation suggested before it is logical that the second harmonic is amplified even for small amplitude levels (second harmonic is inside second mode instability region). There has to be an initial signal for a disturbance to be amplified. If the input disturbance was purely one frequency, which would be expected for a linear case, there would be no initial disturbance for the second harmonic, but yet there is a noticeable signal (figures 63 and 65). A possible explanation for this paradox is the shock wave created by the disturbance input. A shock is a nonlinearity in the flow field and this nonlinearity occurs already for low input amplitude levels considered "linear". This nonlinearity can generate higher harmonic disturbances which are amplified.

For higher amplitudes case 2 indicated already that higher harmonics increase strongly. With the addition of strong amplification as in case 3 the second harmonic reaches amplitude levels comparable to the first harmonic (figures 64,66). In figures 64 and 66 another nonlinear effect becomes visible: In the last third of the domain (streamwise) the disturbances that were amplified at lower input amplitude levels are damped instead.

The outflow boundary condition was chosen to allow disturbances to pass without reflections. In the formulation used the boundary condition contains a wavenumber which is set according to the expected disturbance wave. In case 3 there is not only the expected first mode disturbance wave but also a second mode wave with a different wave number present. Although the second mode wave has approximately 2.2 times the wavelength of the first mode in this case the outflow boundary condition causes only little problems. In figures 63 to 66 there are small wiggles, but they occur only in the close vicinity of the outflow. For the third harmonics (figures 73,74,75,76) the signal is well above numerical noise already for the lowest input amplitude levels. For the highest input amplitude level the signal is in the same order of magnitude as the first mode.

One special feature of this case is the strong modulation seen in the first harmonic of the Fourier signal (figure 59). This effect shows up already for the lowest amplitude level and can therefore be regarded as a linear phenomenon. This modulation may occur due to the interaction of two waves. In a first step towards verifying this idea the frequencies of the waves involved were determined. The time-wise Fourier decomposition would resolve all frequencies contained in the disturbance signal if this signal is periodic with respect to the period of the lowest frequency of the decomposition. A simple check for periodicity is to compare the signal of consecutive (assumed) periods of the disturbance signal. If the signal over consec-

utive intervals is identical, the assumed period length is "correct" and the signal is periodic. Figure 77 shows the signal of u sampled at one single grid point over three periods in time. Each period is plotted starting at the same location in the plot. There is only one line visible. Therefore, the signal is periodic. Considering the sine shape of the signal and the strong decay from the first to the higher harmonics, all waves included in the signal must have one frequency. This frequency is the input disturbance frequency.

The next step was to assume the signal is composed of two waves with the same frequency, different wavenumber and no amplification. The assumption of no amplification can be justified by figure 78. This plot shows the first harmonic of p at the wall including its image mirrored at the x-axis and the p' signal for one time step. The pattern of modulation stays practically unchanged so that neglecting amplification is a reasonable assumption to obtain further information. The equation for a disturbance composed of two such waves is:

$$\varphi'(x,t) = \varphi_1 e^{i(\omega t - \alpha_1 x)} + \varphi_2 e^{i(\omega t - \alpha_2 x)} \quad .$$

Applying a Fourier transform and evaluating the real (physical) part:

$$\mathrm{Re}(\hat{\varphi}(x)) = \sqrt{\varphi_1^2 + \varphi_2^2 + 2\varphi_1\varphi_2 \cos[(\alpha_1 - \alpha_2)x]}$$

Determining the extrema of this function:

$$\varphi_{\max} = \varphi_1 + \varphi_2$$

$$\begin{aligned} \varphi_{\min} &= |\varphi_1 - \varphi_2| \\ \Delta x &= 2\pi/(\alpha_1 - \alpha_2) \quad . \end{aligned}$$

Here Δx is the distance between two consecutive minima or maxima. Using $\varphi_{\min} \approx 0$ from figure 78 one further assumption can be made:

$$\varphi_1 = \varphi_2 = \varphi_{12}$$

and therefore

$$\varphi(t) = 2\varphi_{12} \cos\left(\frac{\alpha_1 - \alpha_2}{2} x\right) \cos\left(\frac{\alpha_1 + \alpha_2}{2} x\right) \quad .$$

The first cosine term represents the modulation as already derived from Fourier analysis. The second cosine term represents the wavelength which is $(\alpha_1 + \alpha_2)/2$. If we use the formulas derived here together with figure 78 both wavenumbers can be determined:

$$\begin{aligned} \alpha_1 &= 13.47 \\ \alpha_2 &= 10.13 \quad , \end{aligned}$$

where $\alpha = \bar{\alpha} L$. Both waves are shown in figure 79 (different nondimensionalisation of α). The first wave matches the expected wave, the second is obviously an additional solution, which is probably weakly damped as the minima in figure 78

increase slightly with increasing x. In private communication between Dr. Fasel and Dr. Mack, Dr. Mack verified that this second solution can also be obtained from linear stability theory.

In figures 80 and 81 the modulation at the highest and lowest amplitude level is compared. In Figure 80 the mean amplitude and the minima are increasing. The difference between minima and maxima remains nearly unchanged. Therefore, one of the waves is amplified, the second approximately neutral. Figure 81 demonstrates a distinctively different situation. Here the modulation and the mean amplitude remain constant, suggesting that both waves propagate neutrally because of saturation.

Figures 82 to 97 present phases and amplitudes as a function of y. Phases of the second harmonic at the linear amplitude level are dominated by random noise and are therefore not plotted. Here, for u and v the phase angles change considerably between the linear and nonlinear case. All other phase and amplitude plots indicate only minor changes for the two disturbance input levels.

6 CONCLUSIONS

Concluding this thesis it can only be reemphasized that stability of a compressible flow is indeed an involved area of research. Three phenomena could be demonstrated:

- disturbances propagating along the Mach line, forming a shock
- nonlinear responses of the boundary layer to increasing input disturbances
- multiple waves for one frequency

It is far too early to even speculate about the importance of these phenomena in the process of transition. Further research should mainly follow three tracks:

- extend computations to three dimensions
- follow the spatial development for longer distances, further into the nonlinear regime.
- try to influence the development of waves, or in a first step, see how they react to wall cooling or heating.

The direct Navier Stokes simulations have proven to be an accurate and powerful tool to study compressible instability mechanisms.

A FIGURES

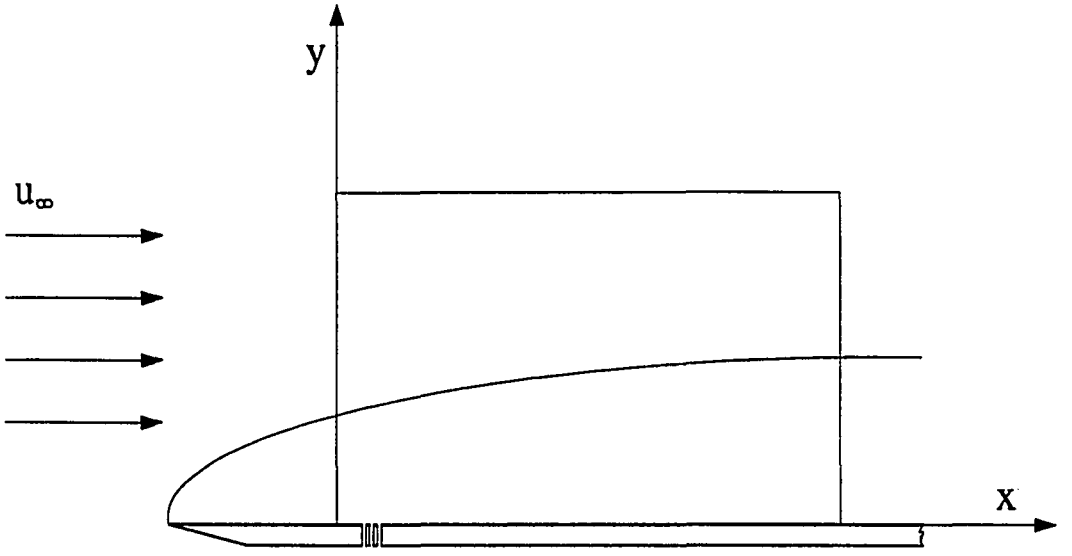

Figure 1: flat plate model

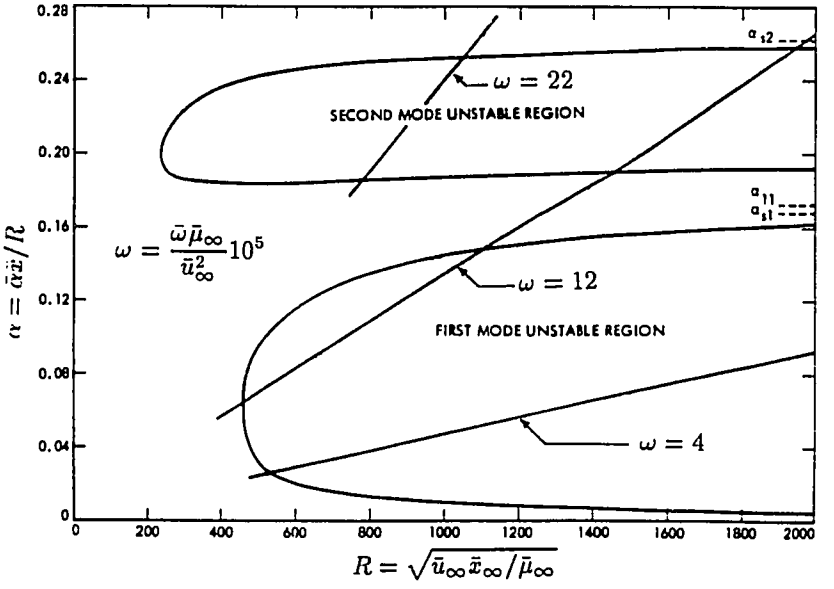

Figure 2: neutral curves at M=4.5 (taken from [1])

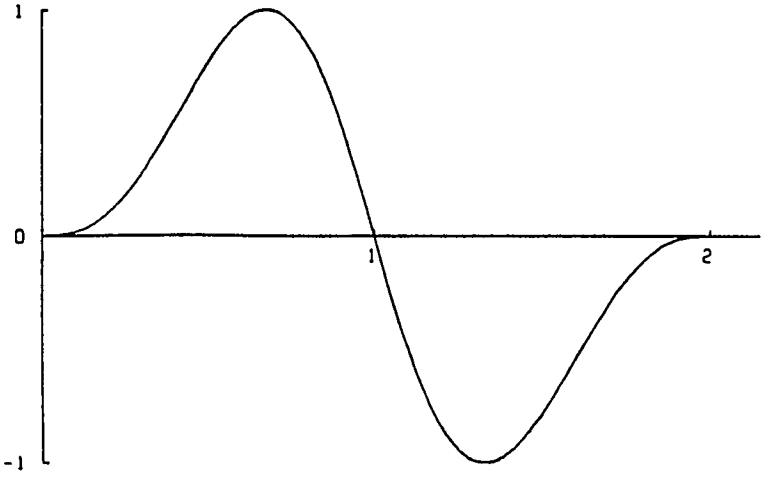

Figure 3: 5^{th} order polynomial for blowing

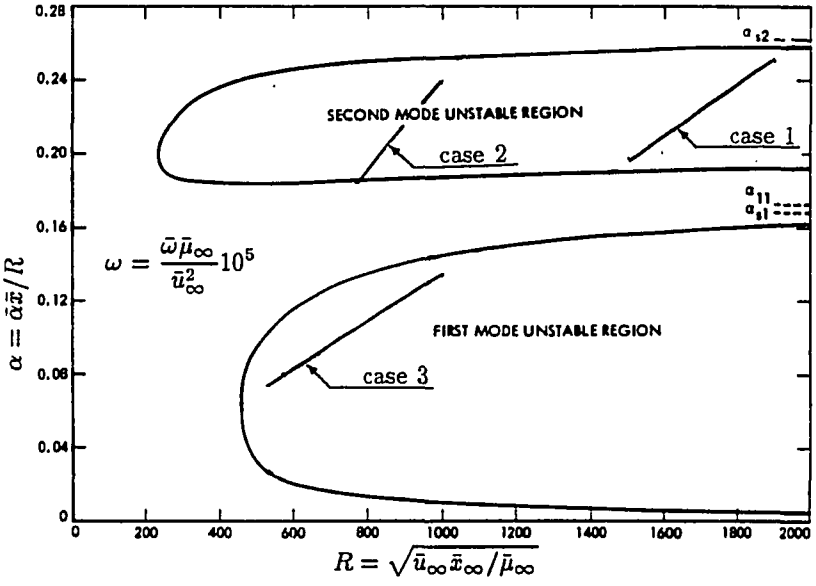

Figure 4: computational domains in the stability diagram

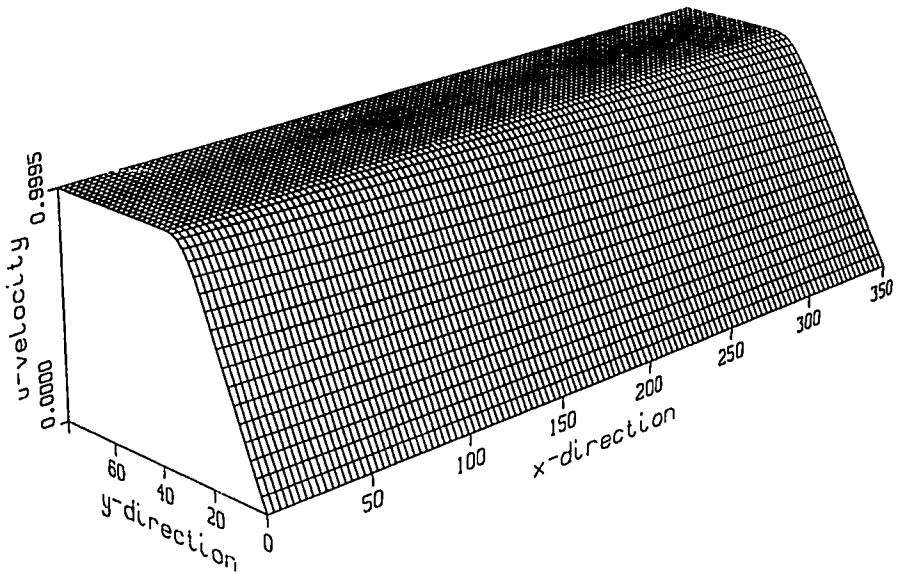

Figure 5: baseflow profile of u for the first case

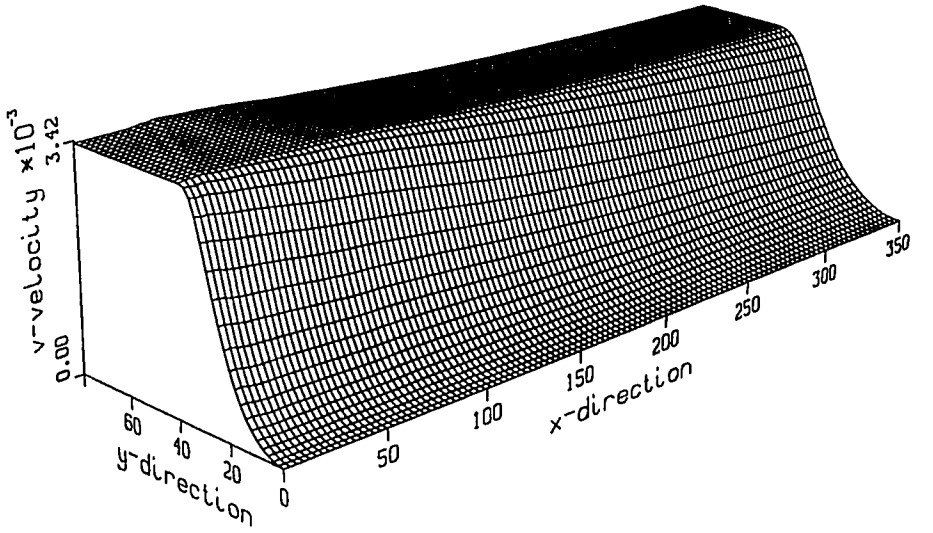

Figure 6: baseflow profile of v for the first case

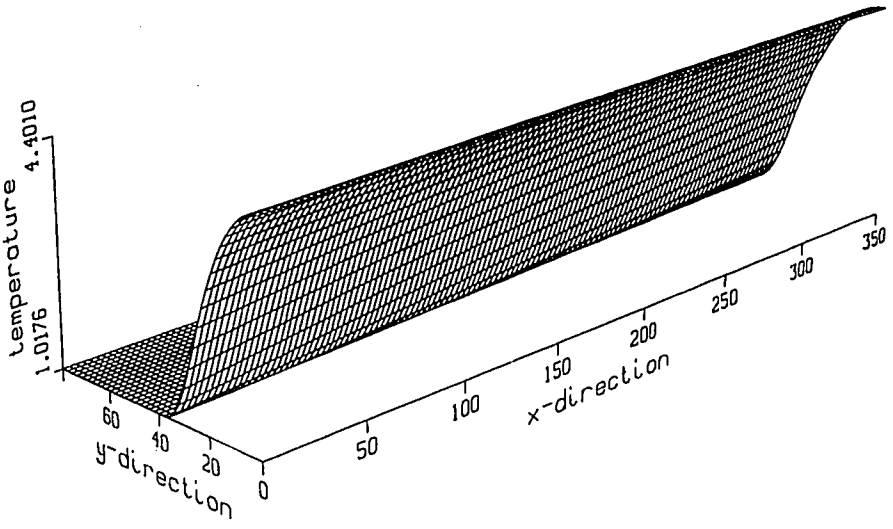

Figure 7: baseflow profile of T for the first case

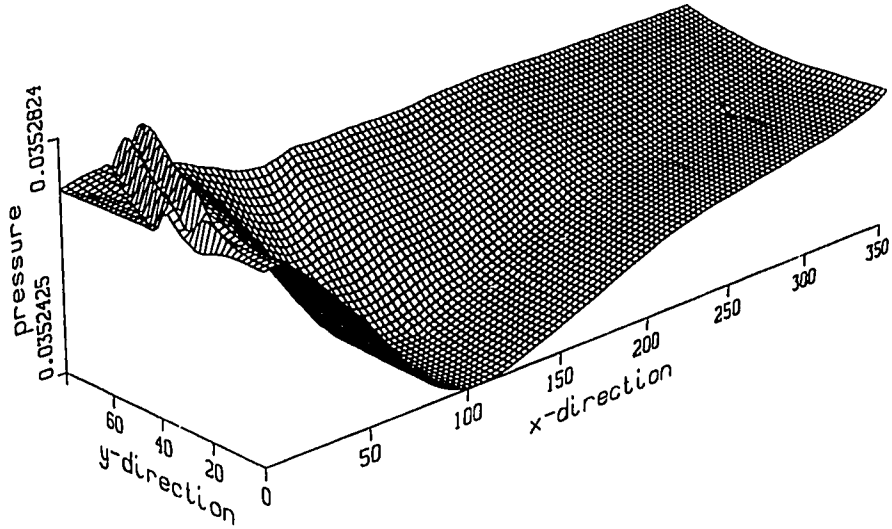

Figure 8: baseflow profile of p for the first case

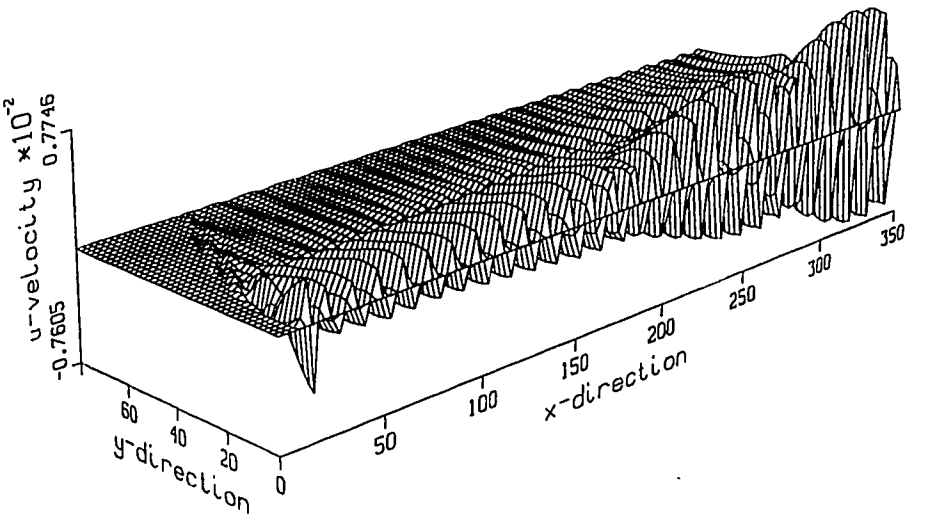

Figure 9: u' for $t = const.$ for the first case

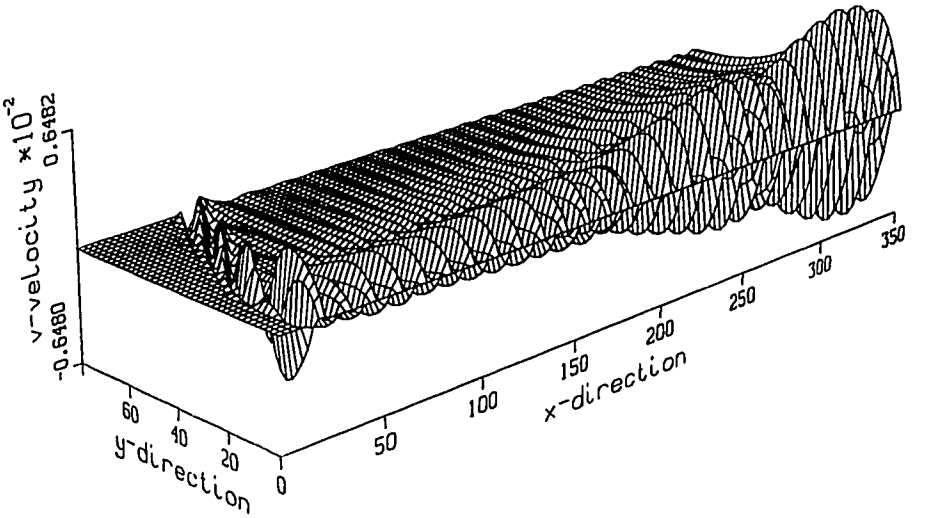

Figure 10: v' for $t = const.$ for the first case

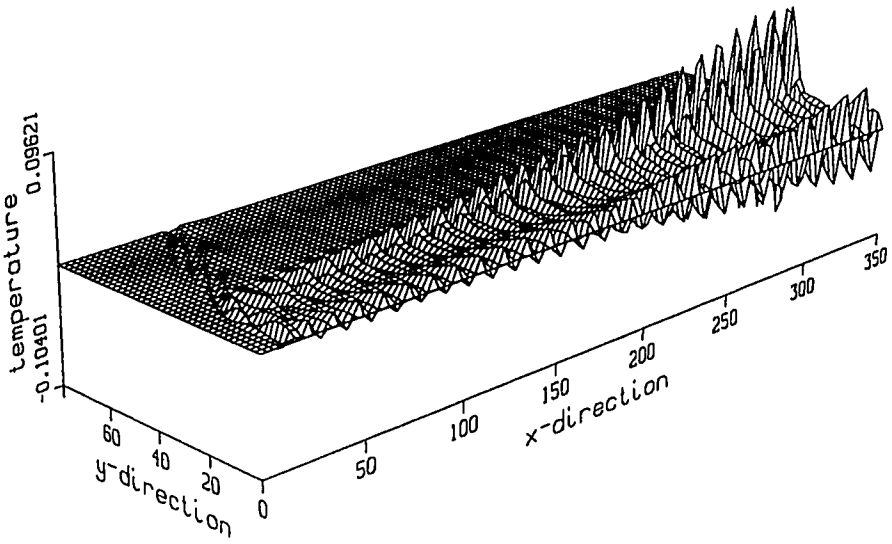

Figure 11: T' for $t = const.$ for the first case

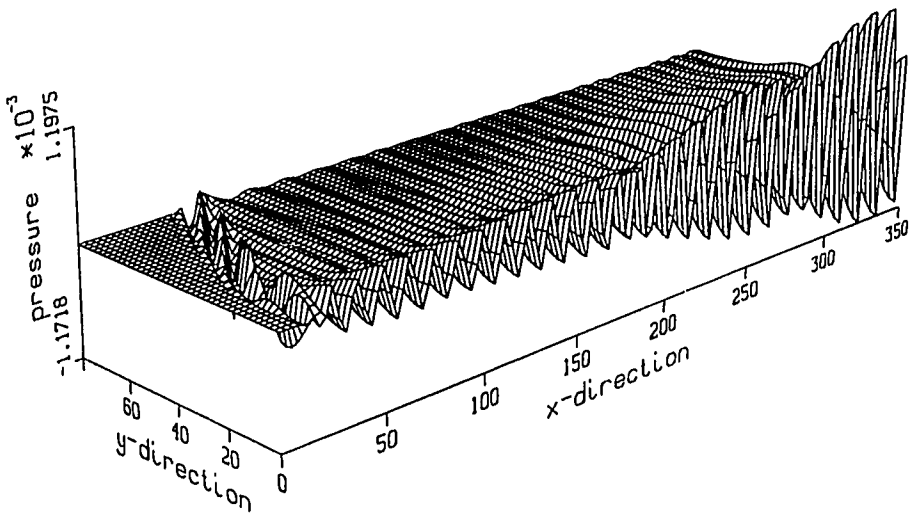

Figure 12: p' for $t = const.$ for the first case

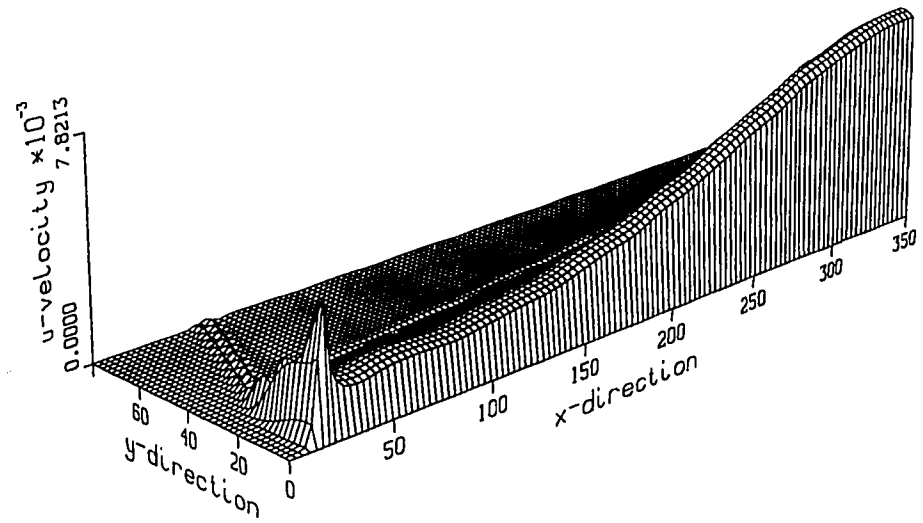

Figure 13: first harmonic of u for the first case

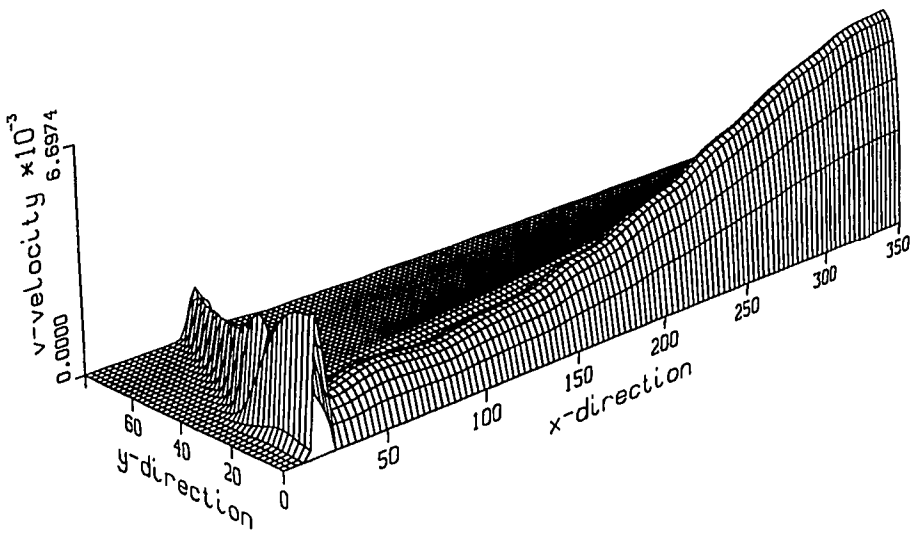

Figure 14: first harmonic of v for the first case

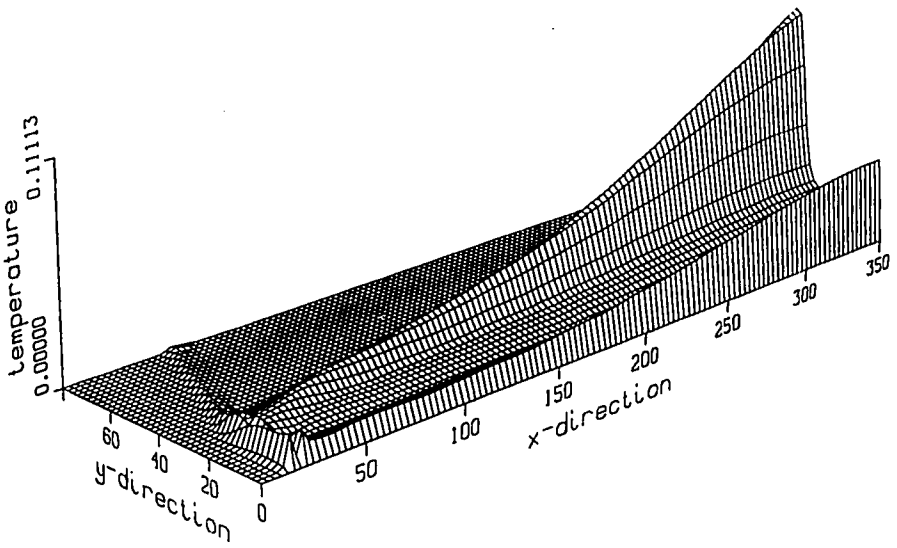

Figure 15: first harmonic of T for the first case

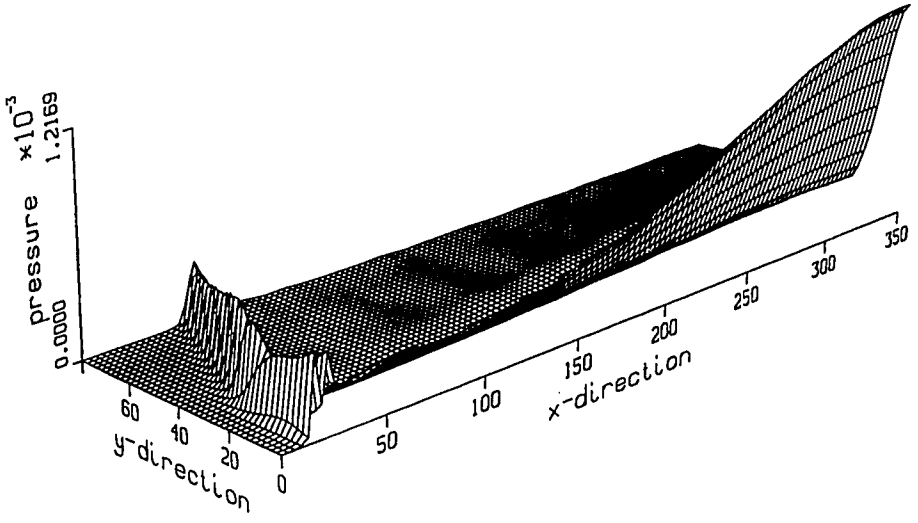

Figure 16: first harmonic of p for the first case

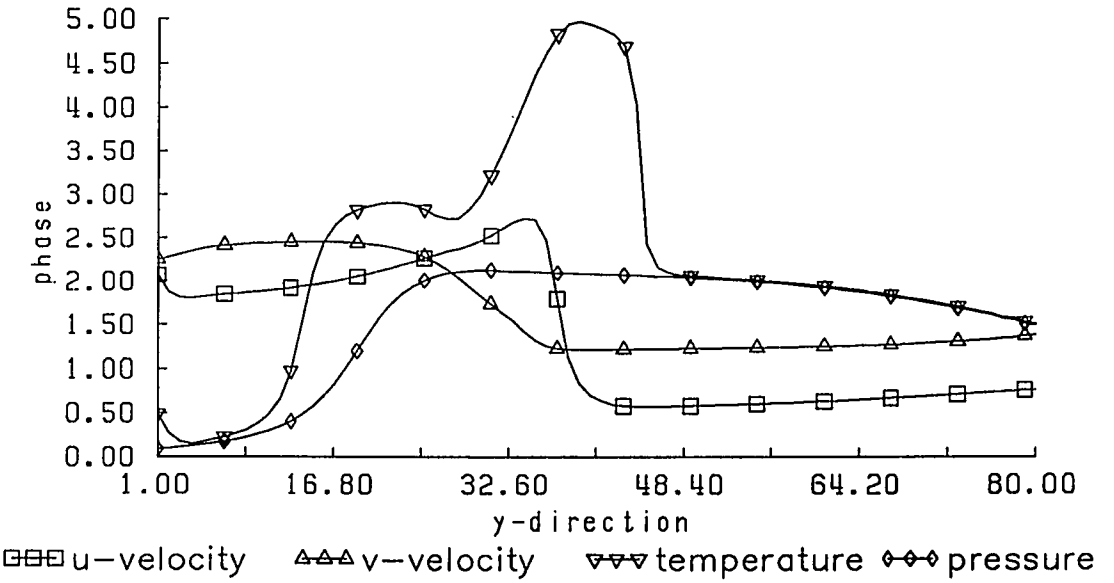

Figure 17: phase angle over y of the first harmonic for case 1

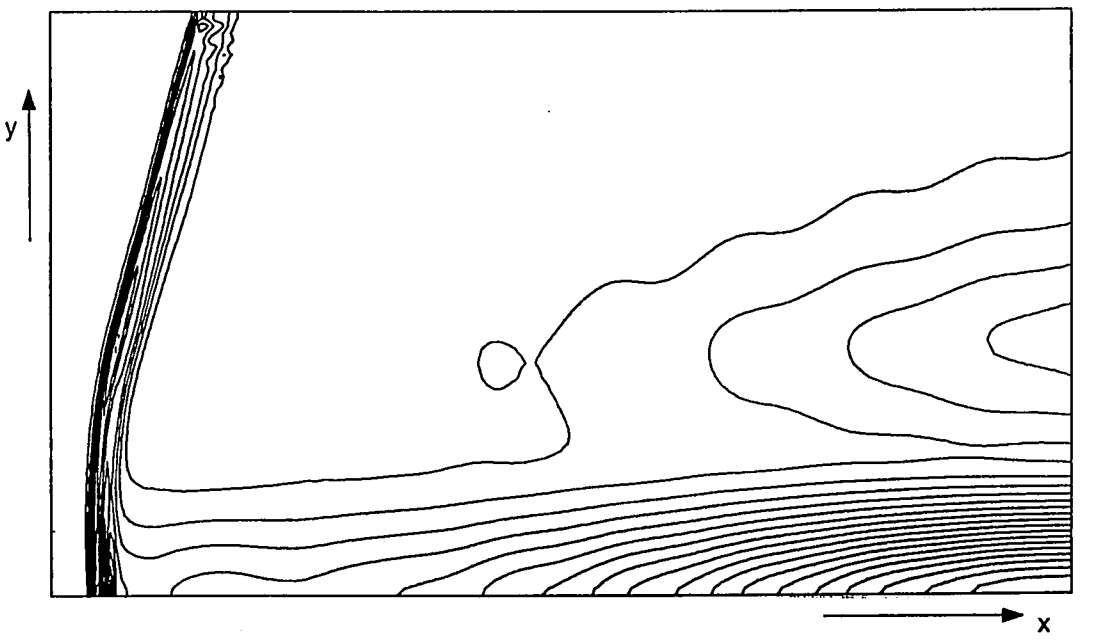

Figure 18: contours of constant pressure for the first harmonic of case 1 (from Fourier analysis)

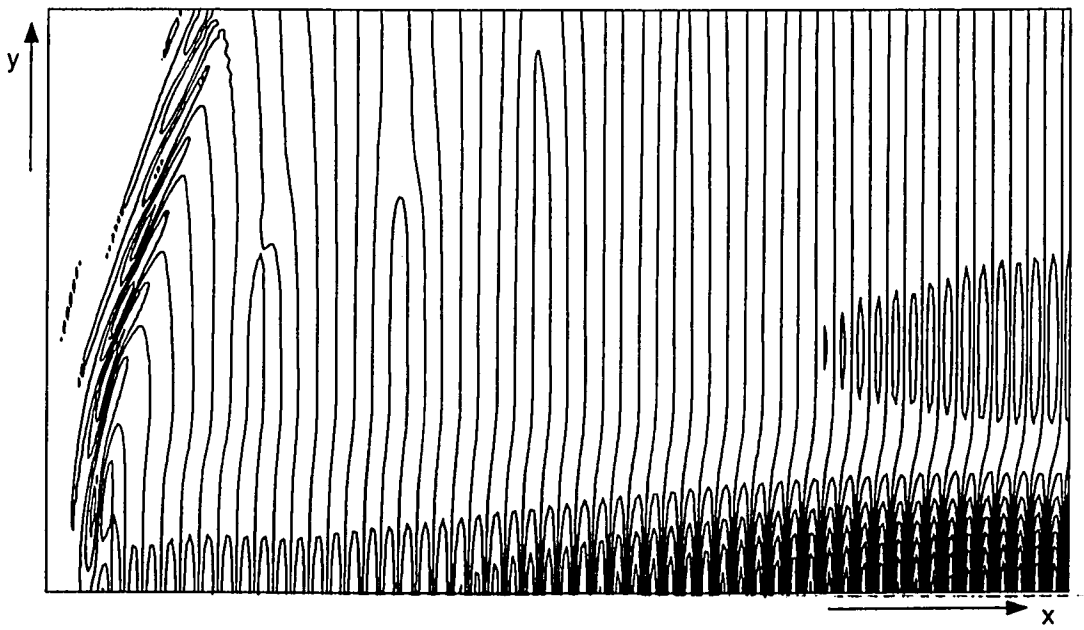

Figure 19: contours of constant pressure from instantaneous signal of case 1

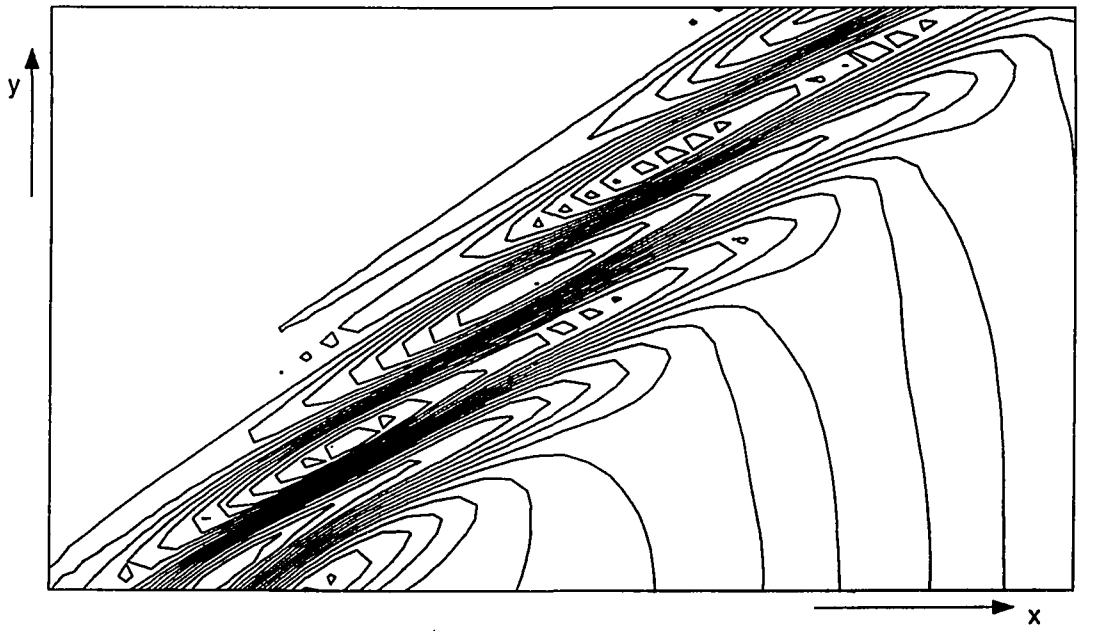

Figure 20: contours of constant pressure of the shock "bubbles" outside the boundary layer (case 1)

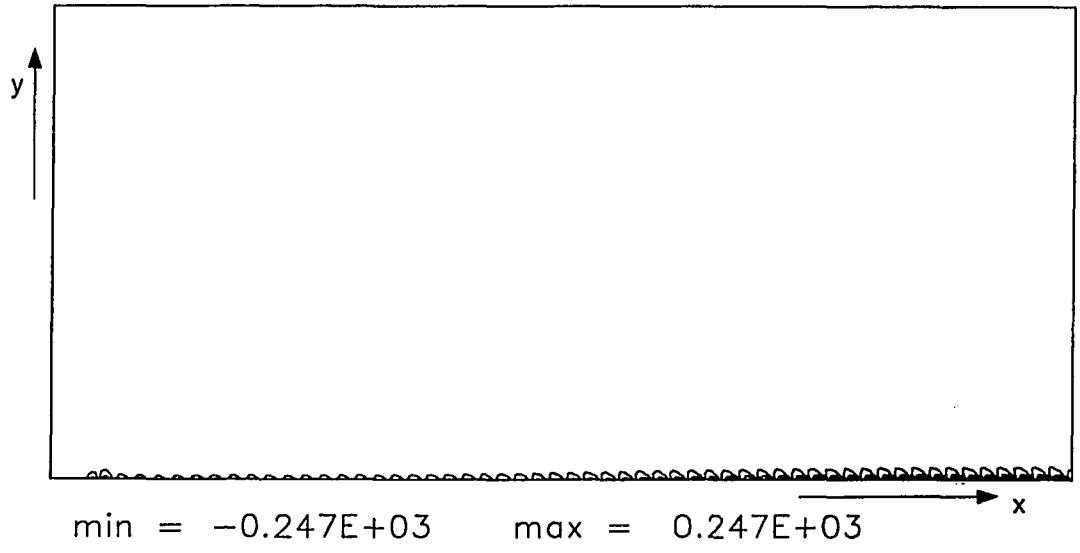

Figure 21: vorticity of the fluctuation in case 1

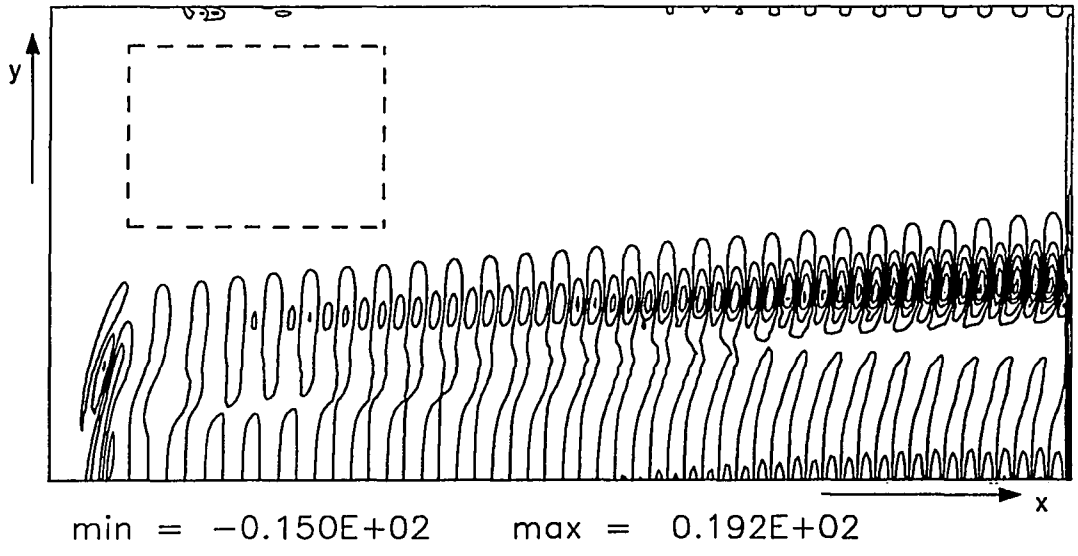

Figure 22: vorticity of the fluctuation in case 1 without wall vorticity

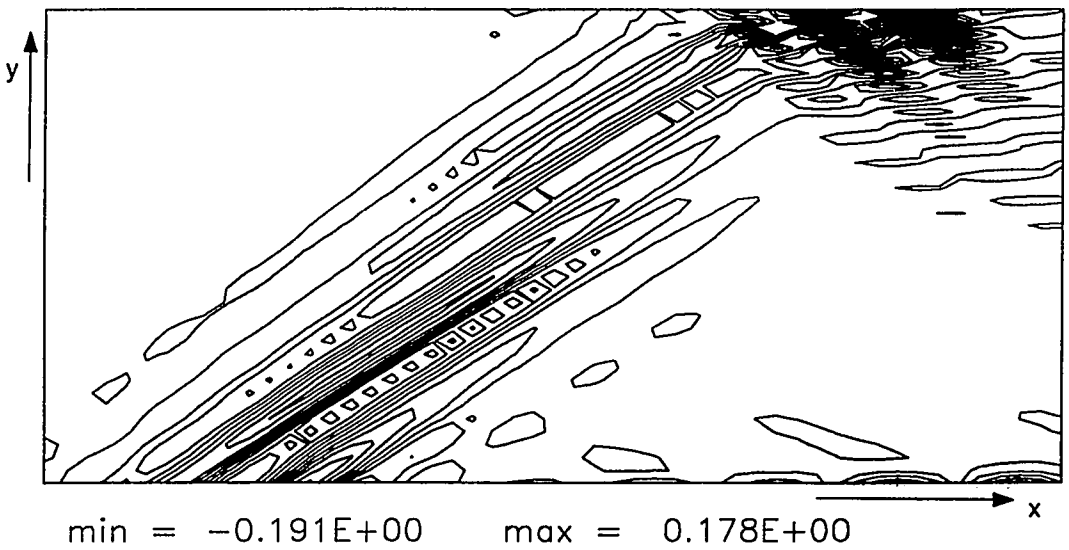

Figure 23: vorticity of the shock "bubbles" outside boundary layer (case 1)

Figure 24: contours of constant p from the first harmonic for case 1 (contour levels unequally spaced)

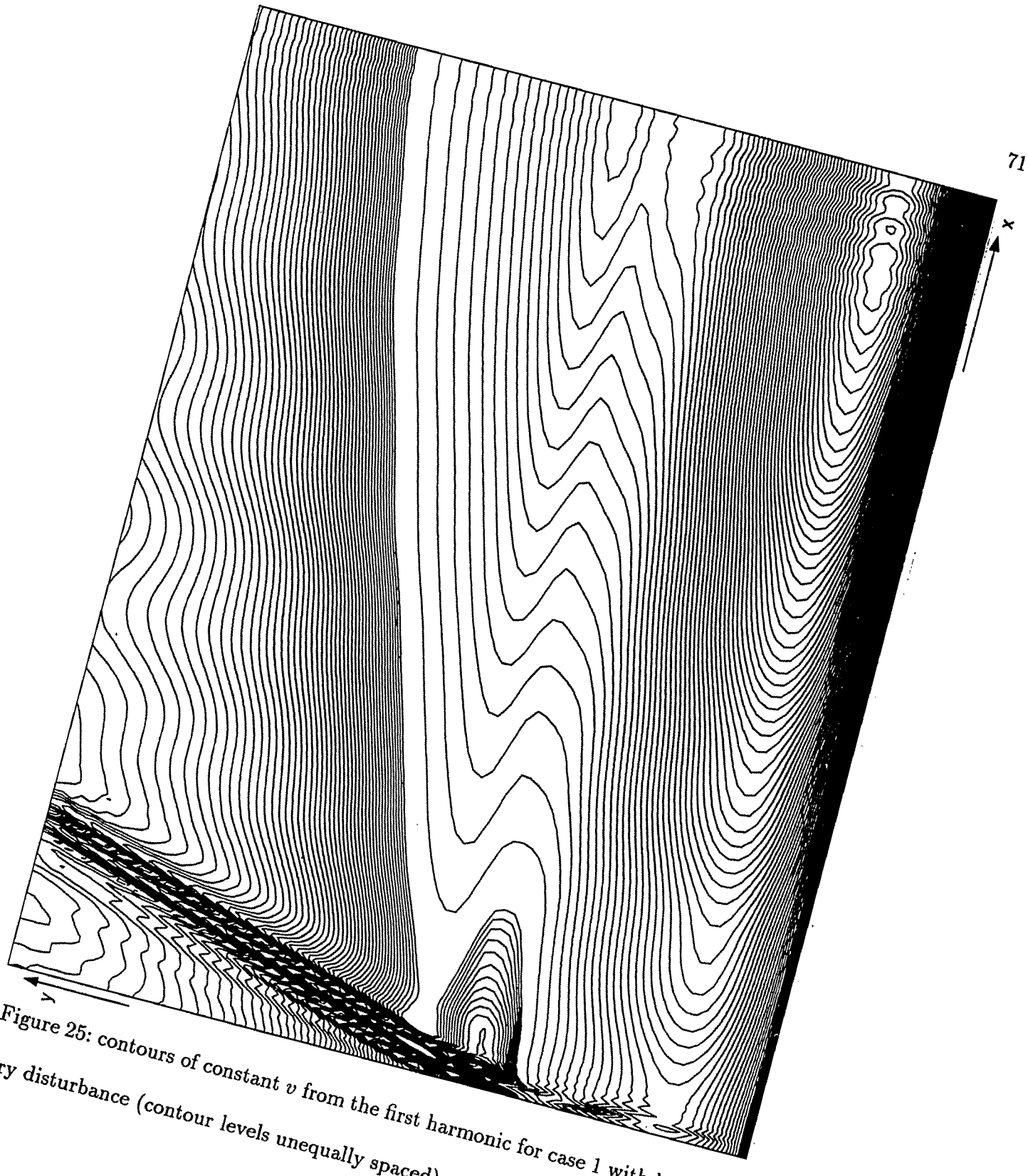

Figure 25: contours of constant v from the first harmonic for case 1 with left boundary disturbance (contour levels unequally spaced)

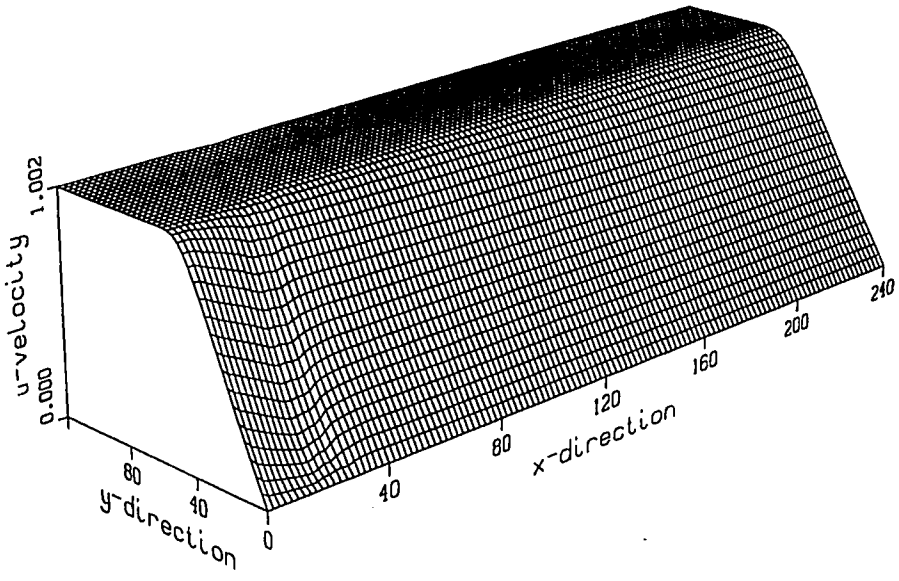

Figure 26: 0^{th} harmonic of u for case 2

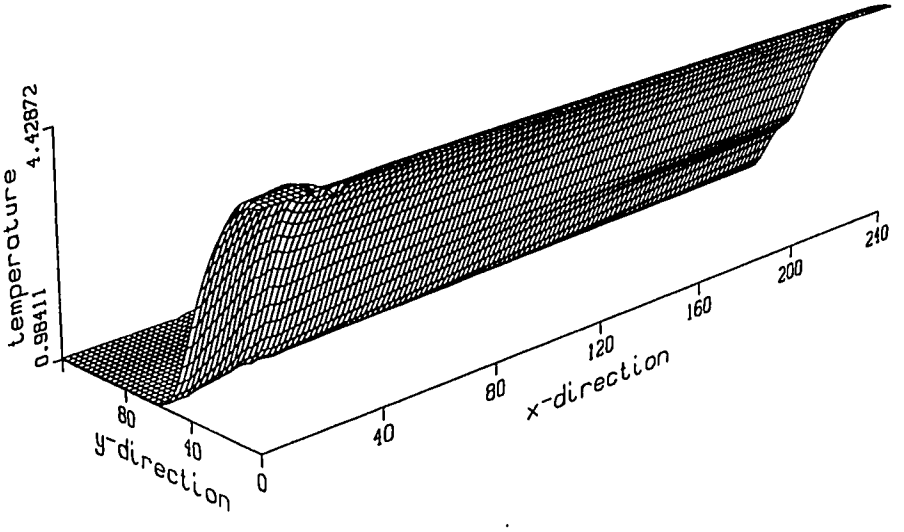

Figure 27: 0^{th} harmonic of T for case 2

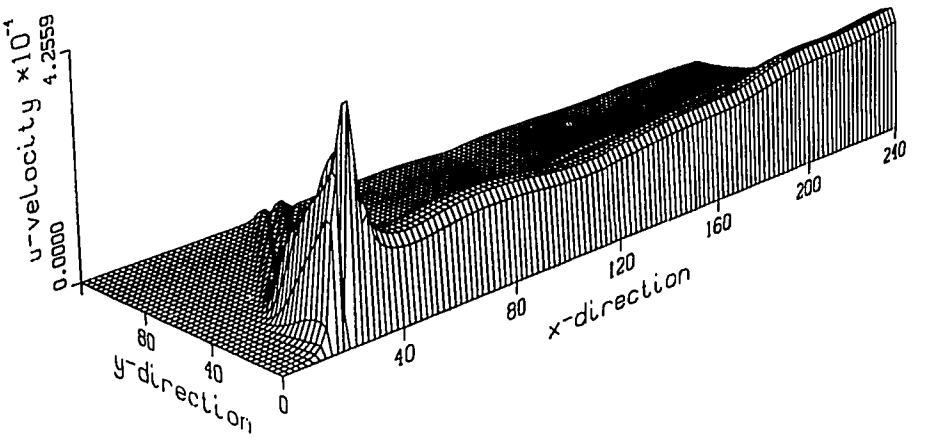

Figure 28: first harmonic of u at $v_{\max} = 0.0004$ for case 2

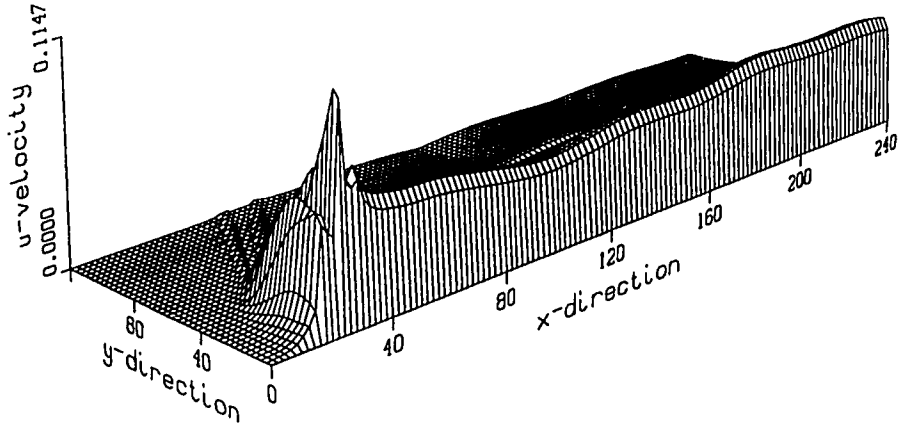

Figure 29: first harmonic of u at $v_{\max} = 0.11$ for case 2

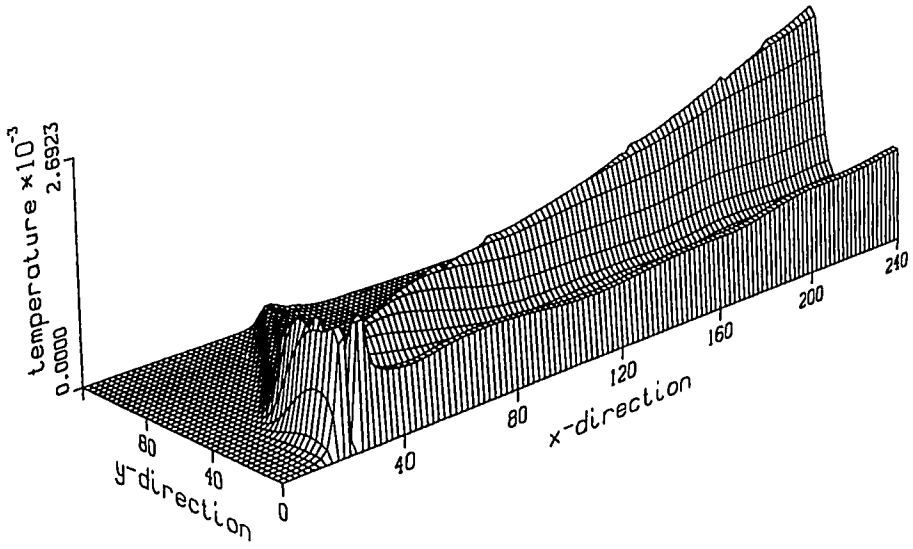

Figure 30: first harmonic of T at $v_{\max} = 0.0004$ for case 2

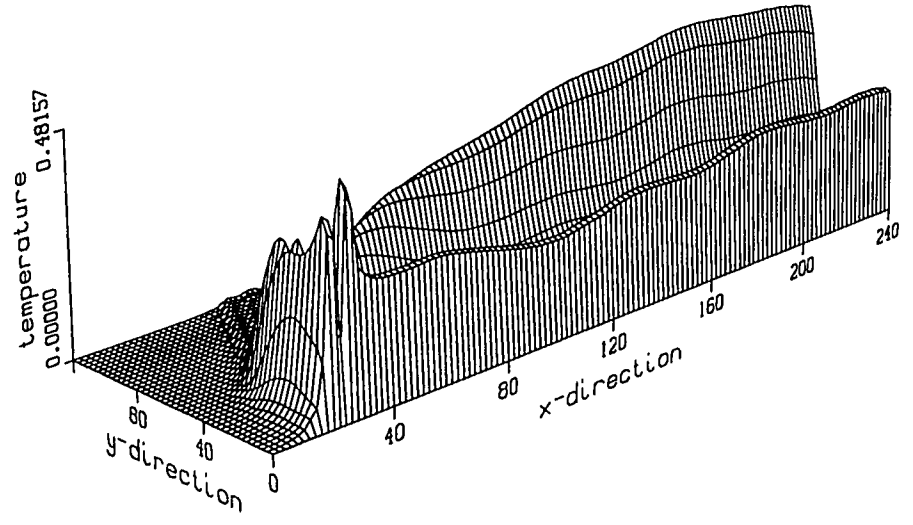

Figure 31: first harmonic of T at $v_{\max} = 0.11$ for case 2

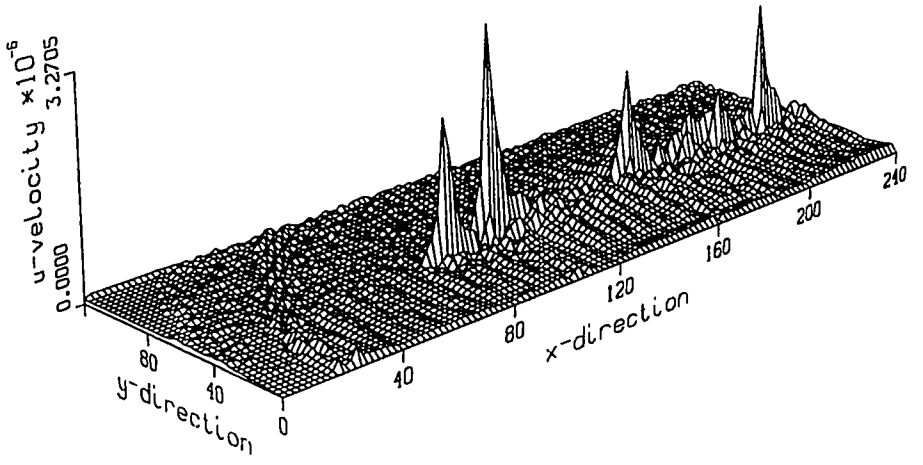

Figure 32: second harmonic of u at $v_{\max} = 0.0004$ for case 2

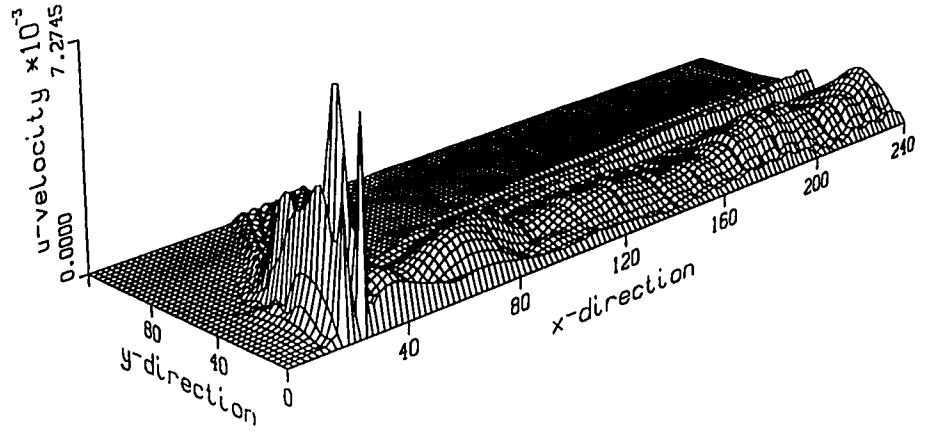

Figure 33: second harmonic of u at $v_{\max} = 0.11$ for case 2

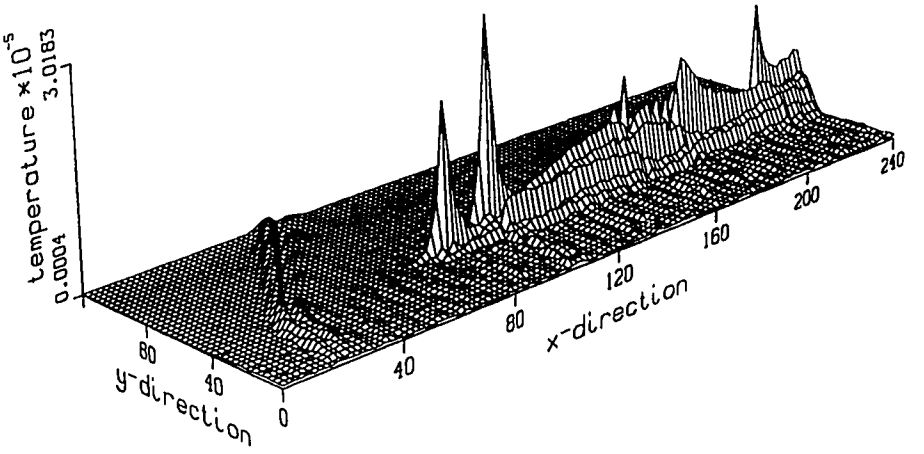

Figure 34: second harmonic of T at $v_{\max} = 0.0004$ for case 2

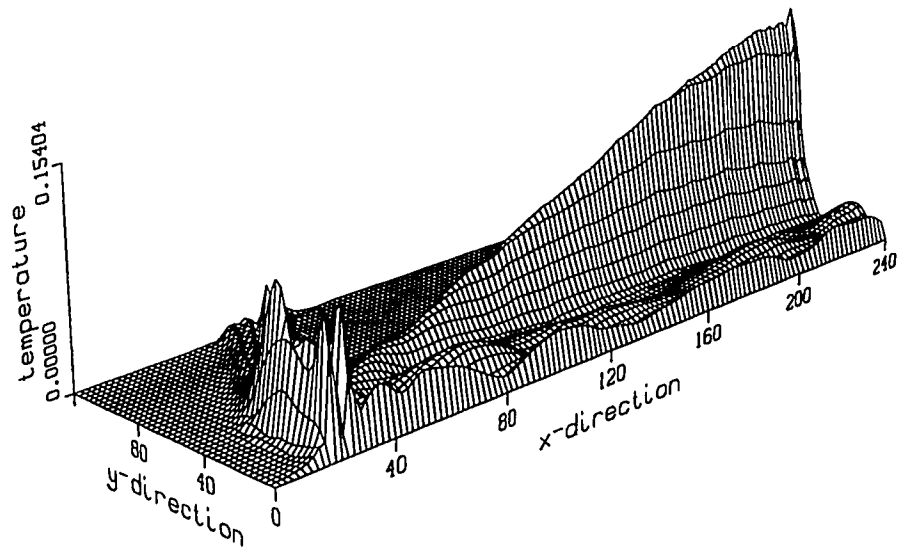

Figure 35: second harmonic of T at $v_{\max} = 0.11$ for case 2

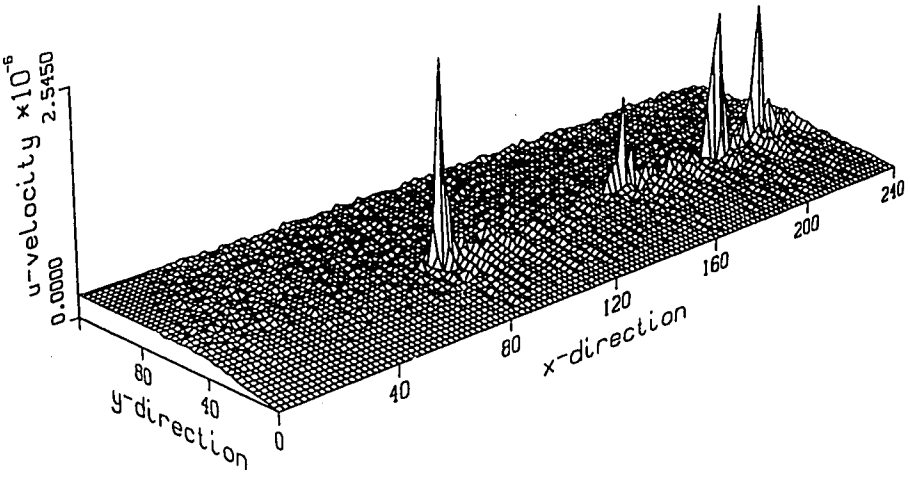

Figure 36: third harmonic of u at $v_{\max} = 0.0004$ for case 2

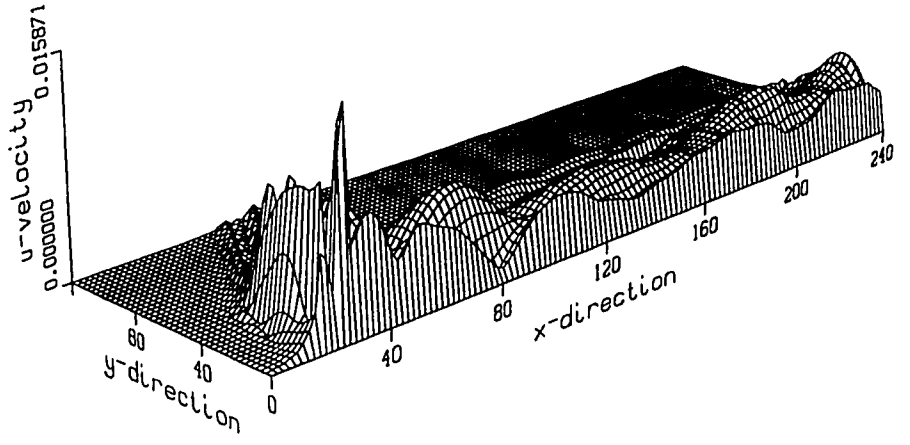

Figure 37: third harmonic of u at $v_{\max} = 0.11$ for case 2

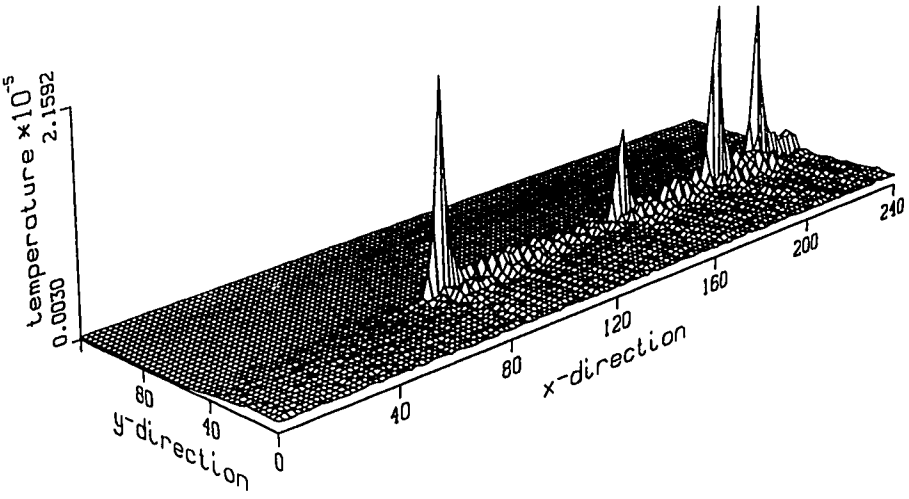

Figure 38: third harmonic of T at $v_{\max} = 0.0004$ for case 2

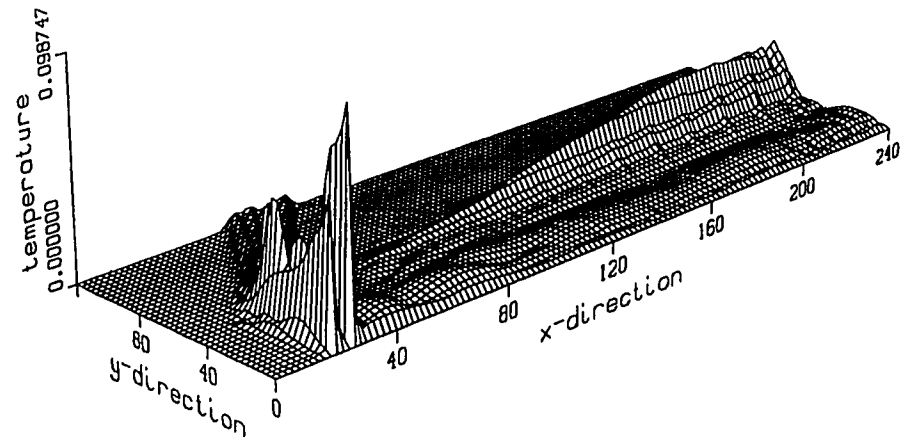

Figure 39: third harmonic of T at $v_{\max} = 0.11$ for case 2

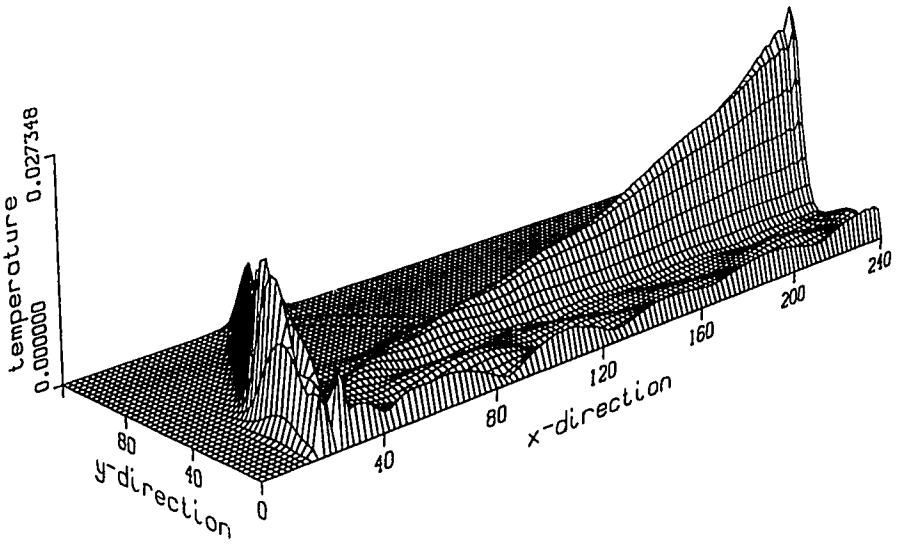

Figure 40: second harmonic of T at $v_{\max} = 0.04$ for case 2

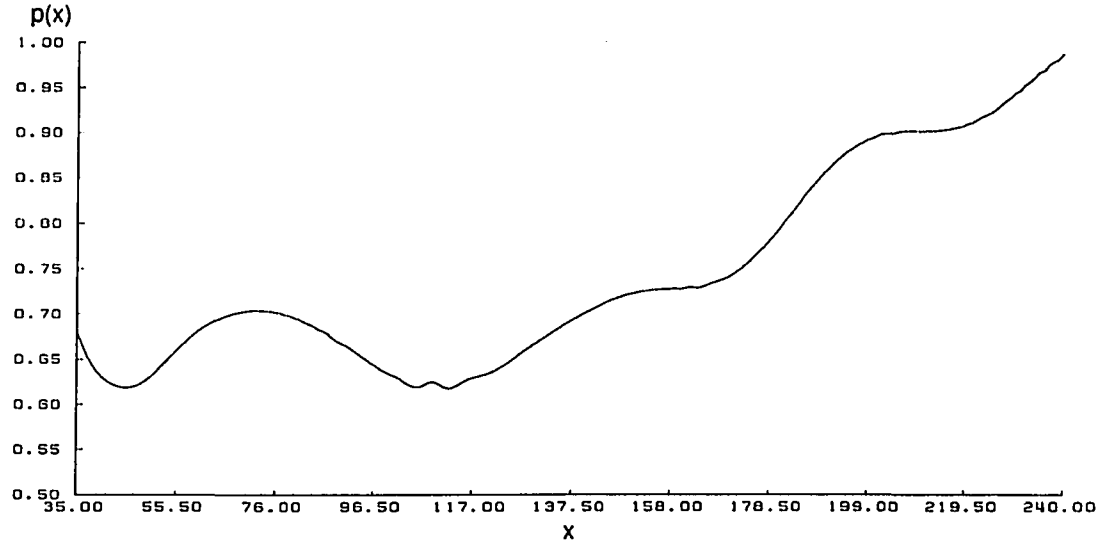

Figure 41: first harmonic of p at the wall at $v_{\max} = 0.0004$ for case 2

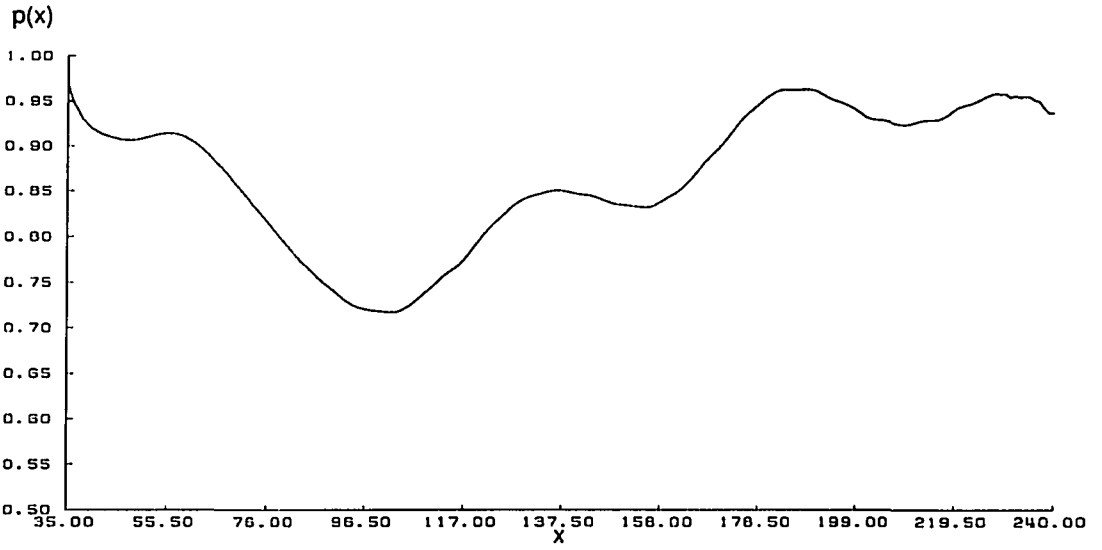

Figure 42: first harmonic of p at the wall at $v_{\max} = 0.11$ for case 2

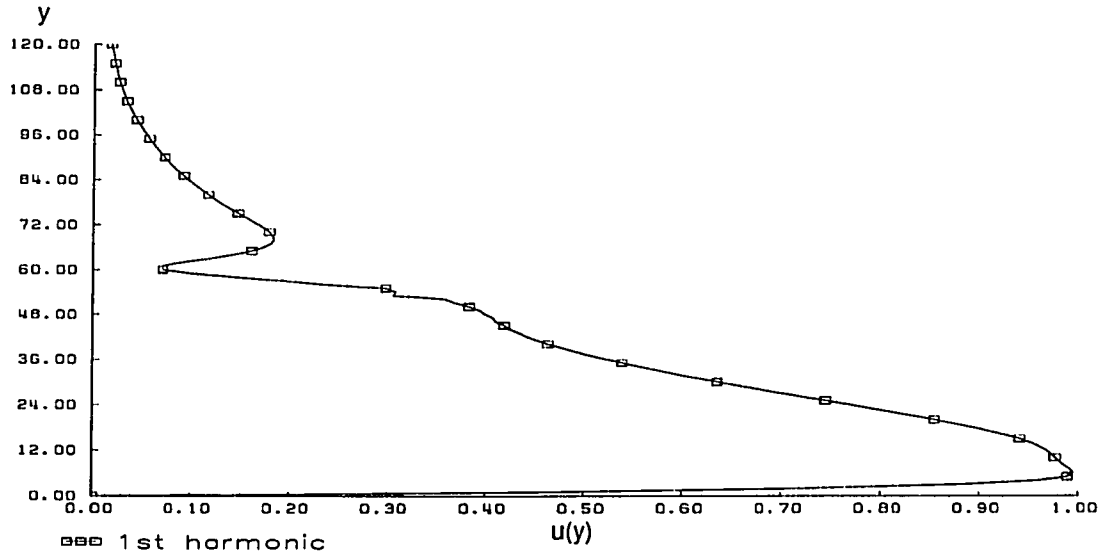

Figure 43: $u(y)$ at grid line 180 at $v_{\max} = 0.0004$ for case 2

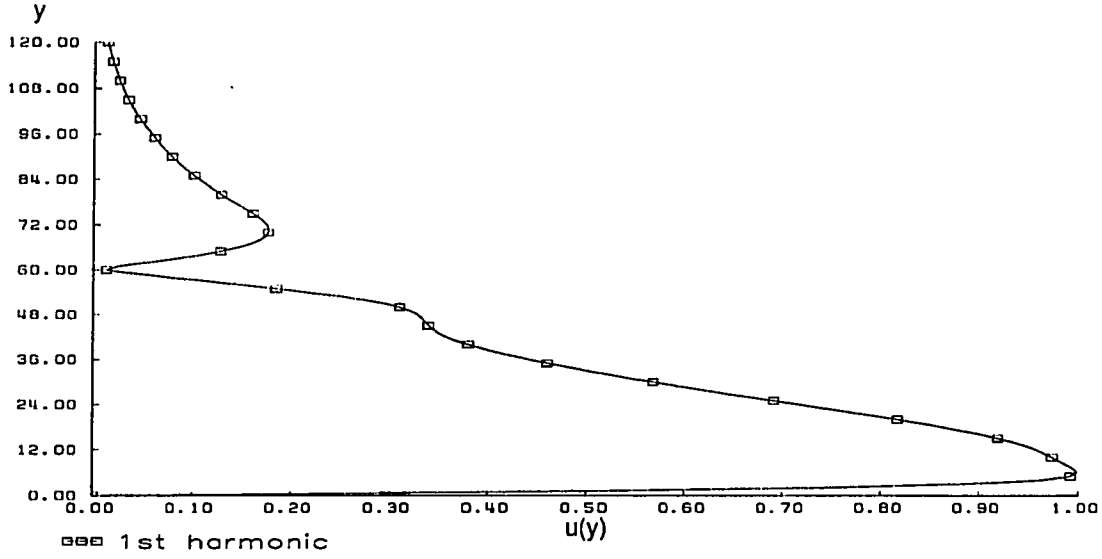

Figure 44: $u(y)$ at grid line 180 at $v_{\max} = 0.11$ for case 2

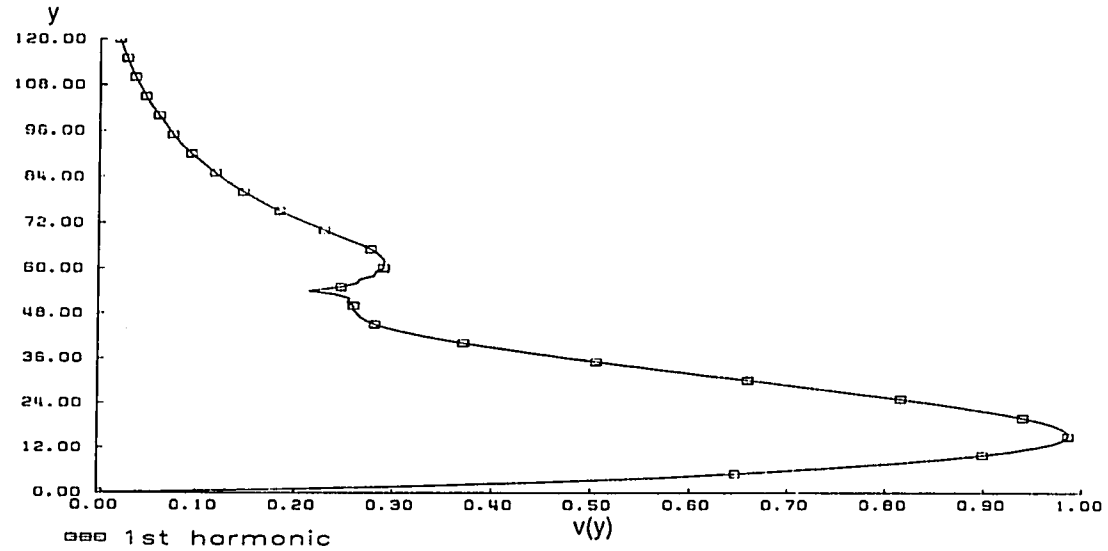

Figure 45: $v(y)$ at grid line 180 at $v_{\max} = 0.0004$ for case 2

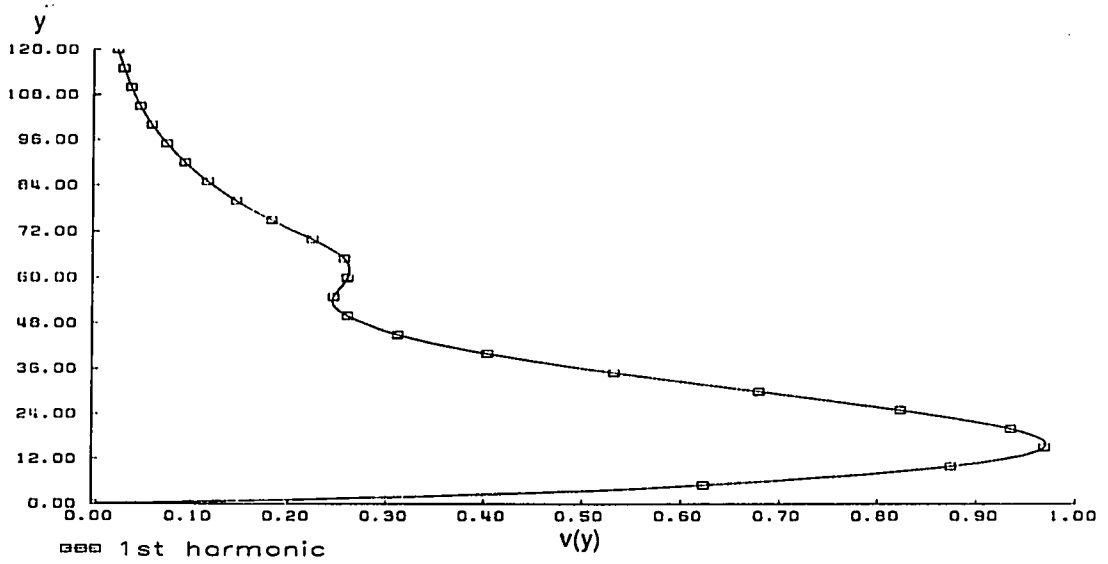

Figure 46: $v(y)$ at grid line 180 at $v_{\max} = 0.11$ for case 2

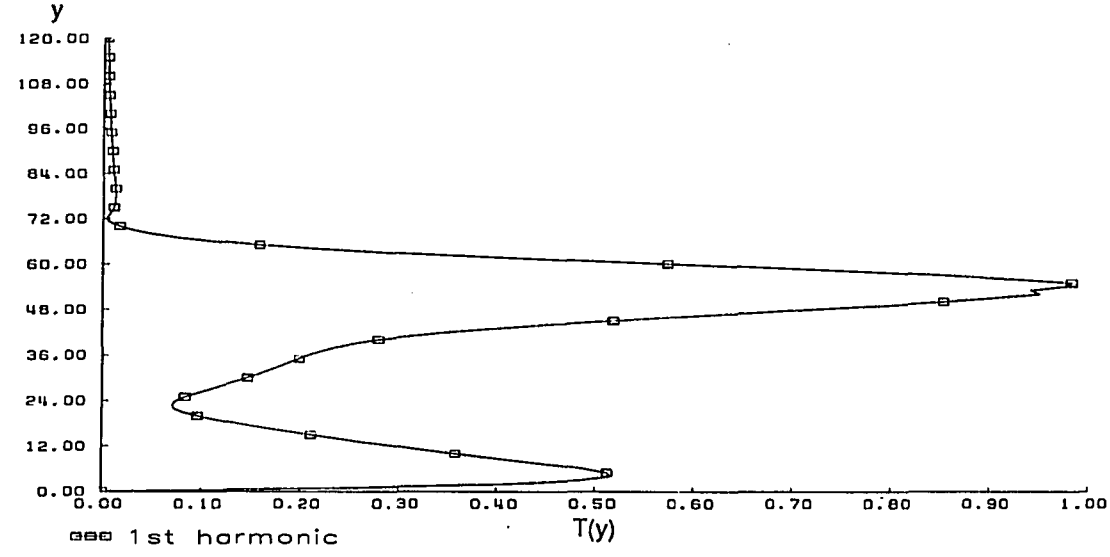

Figure 47: $T(y)$ at grid line 180 at $v_{\max} = 0.0004$ for case 2

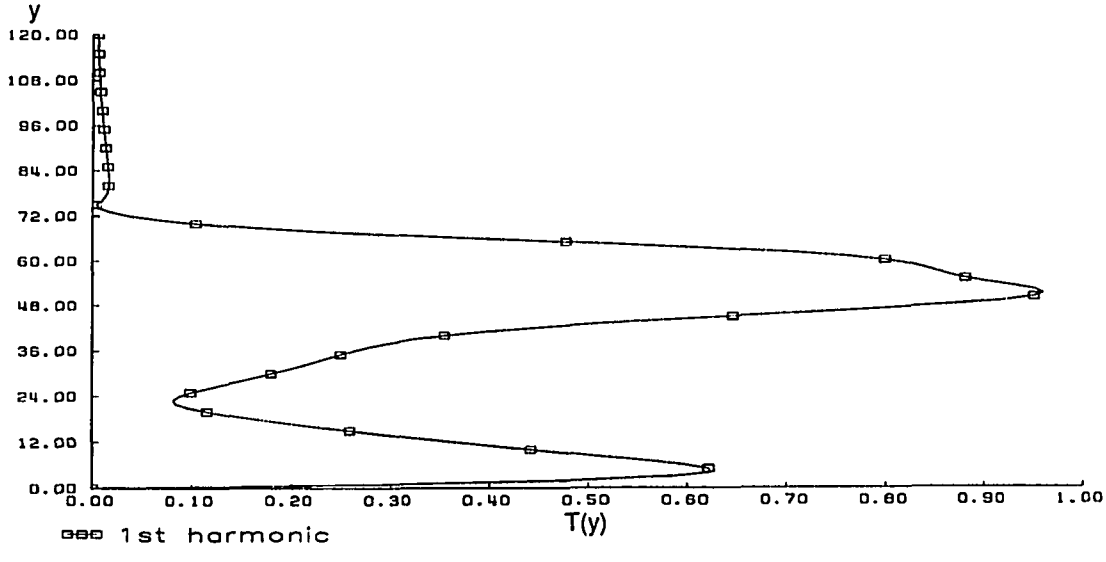

Figure 48: $T(y)$ at grid line 180 at $v_{\max} = 0.11$ for case 2

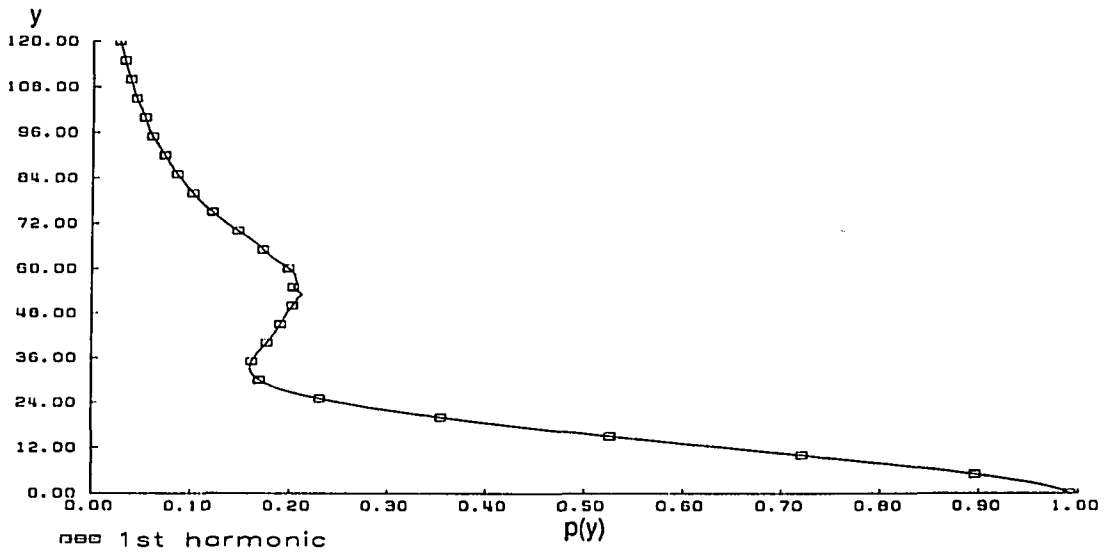

Figure 49: $p(y)$ at grid line 180 at $v_{\max} = 0.0004$ for case 2

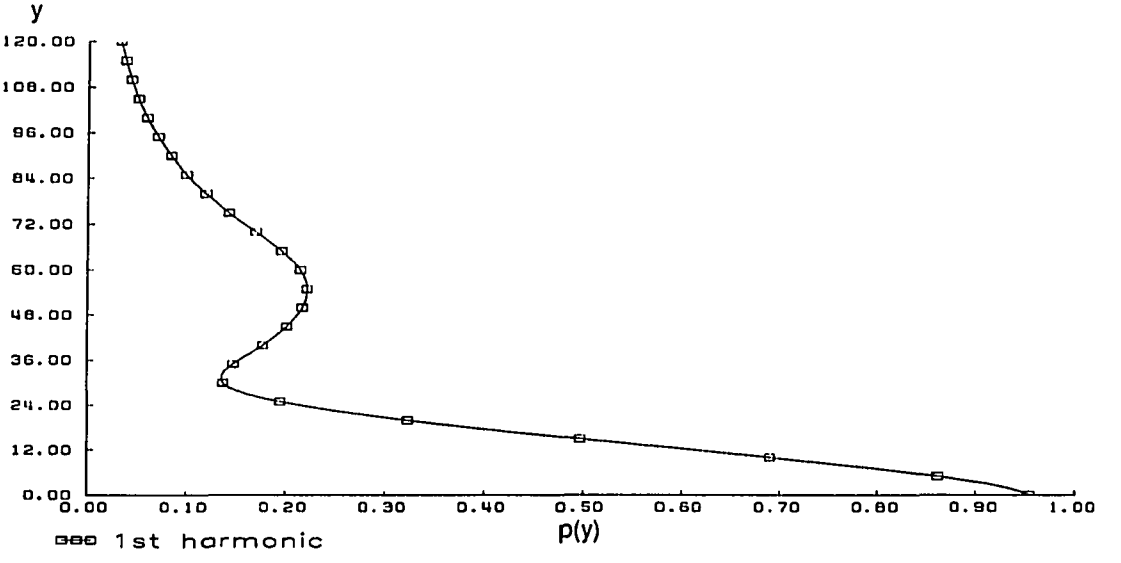

Figure 50: $p(y)$ at grid line 180 at $v_{\max} = 0.11$ for case 2

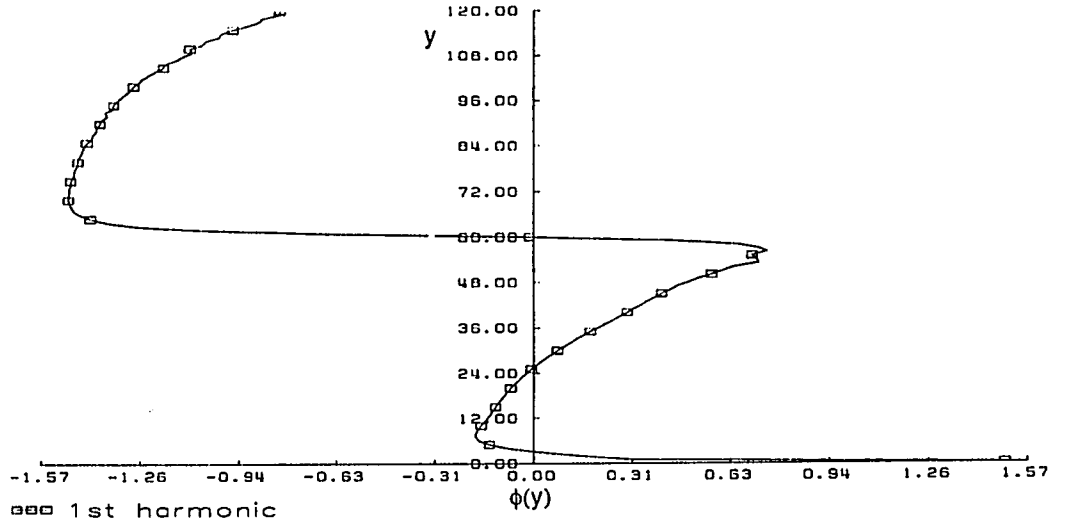

Figure 51: phase of u over y at grid line 180 at $v_{\max} = 0.0004$ for case 2

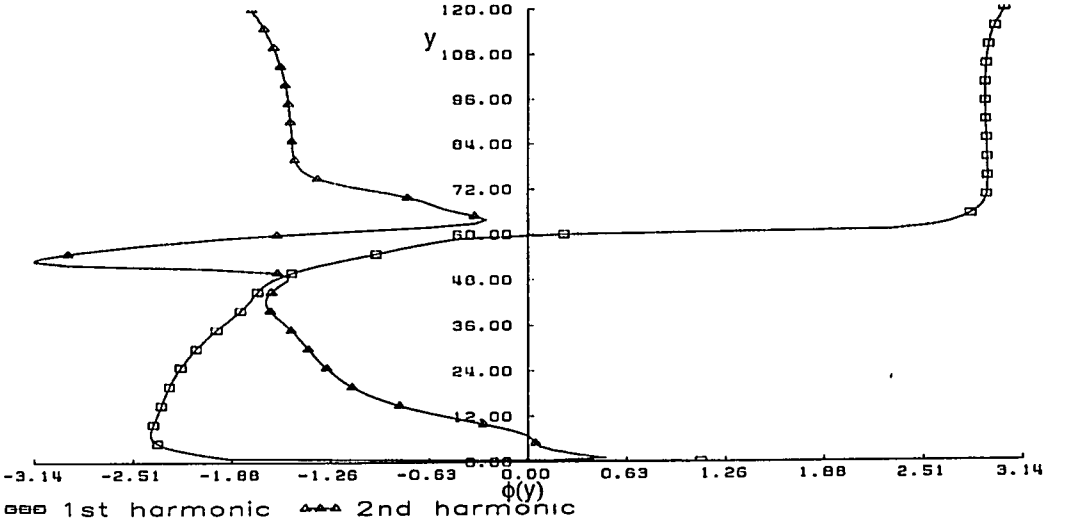

Figure 52: phase of u over y at grid line 180 at $v_{\max} = 0.11$ for case 2

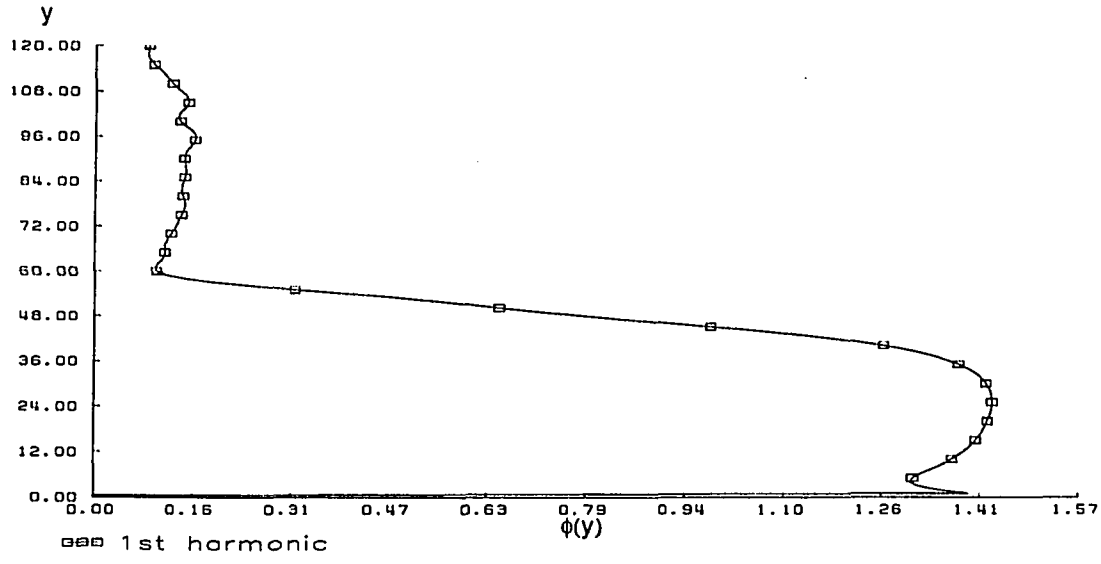

Figure 53: phase of v over y at grid line 180 at $v_{\max} = 0.0004$ for case 2

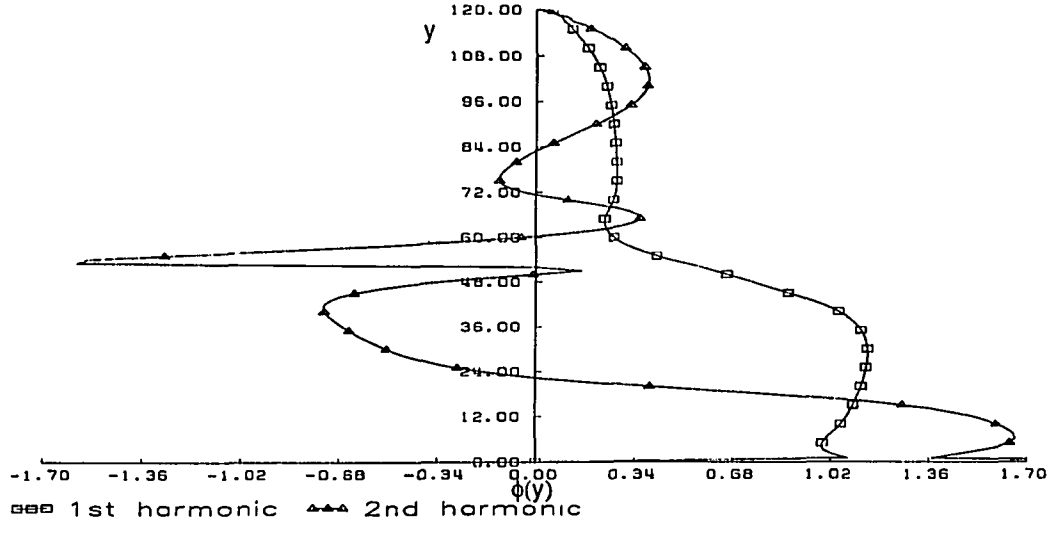

Figure 54: phase of v over y at grid line 180 at $v_{\max} = 0.11$ for case 2

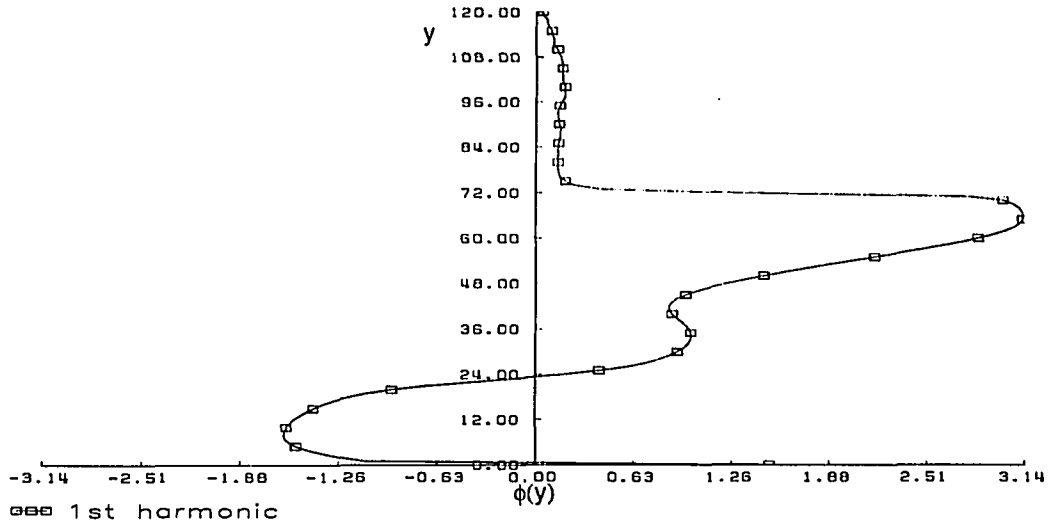

Figure 55: phase of T over y at grid line 180 at $v_{\max} = 0.0004$ for case 2

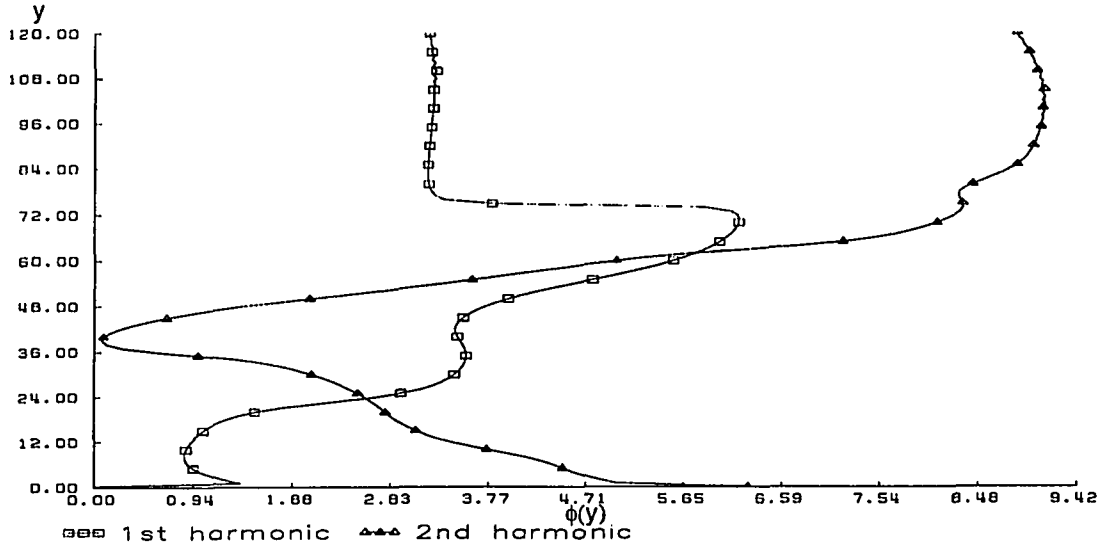

Figure 56: phase of T over y at grid line 180 at $v_{\max} = 0.11$ for case 2

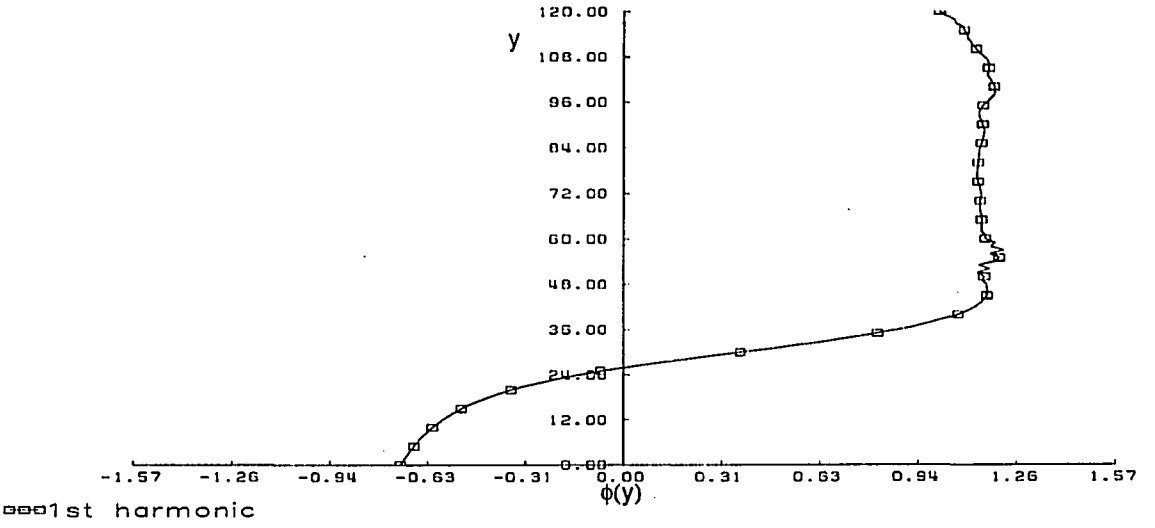

Figure 57: phase of p over y at grid line 180 at $v_{\max} = 0.0004$ for case 2

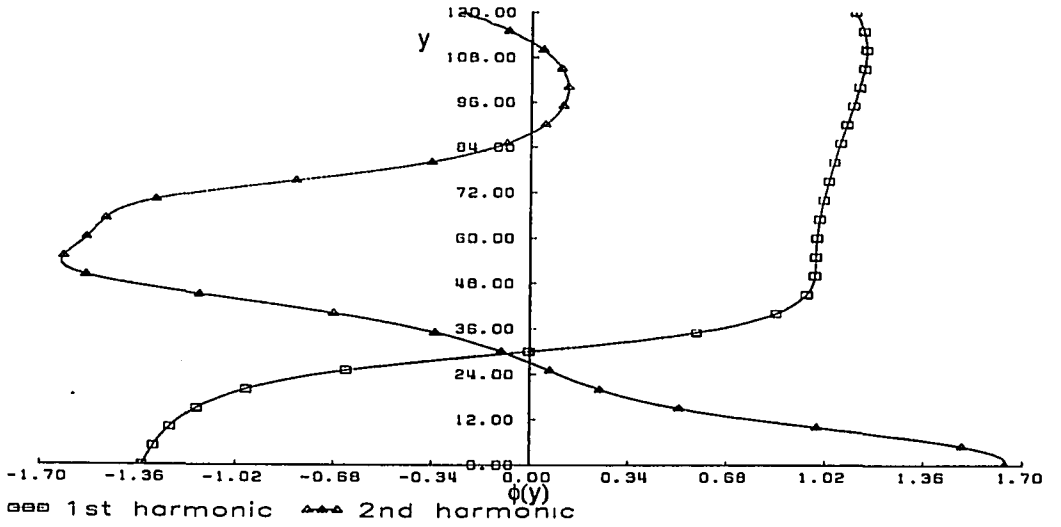

Figure 58: phase of p over y at grid line 180 at $v_{\max} = 0.11$ for case 2

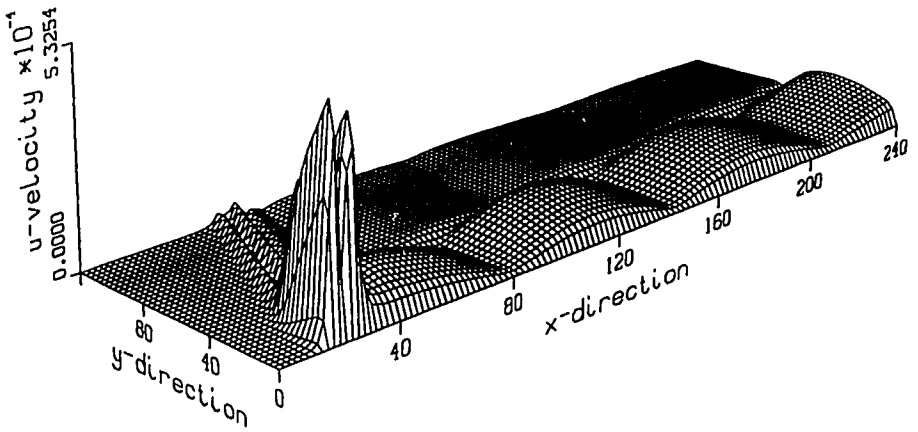

Figure 59: first harmonic of u at $v_{\max} = 0.0004$ for case 3

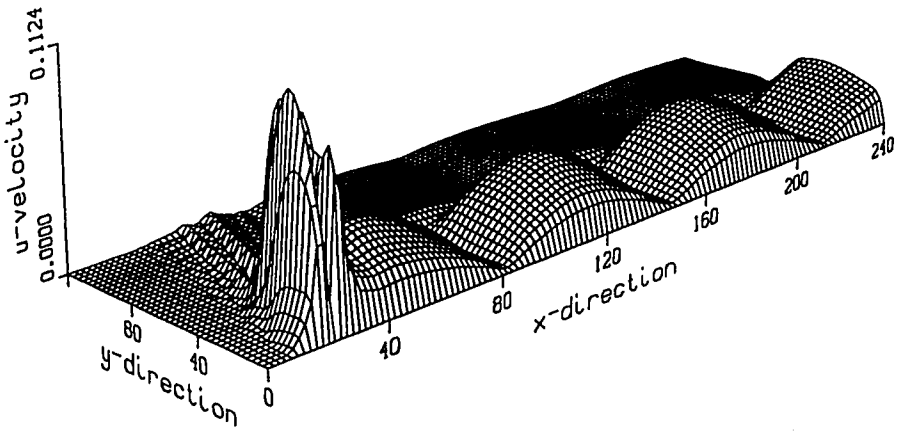

Figure 60: first harmonic of u at $v_{\max} = 0.125$ for case 3

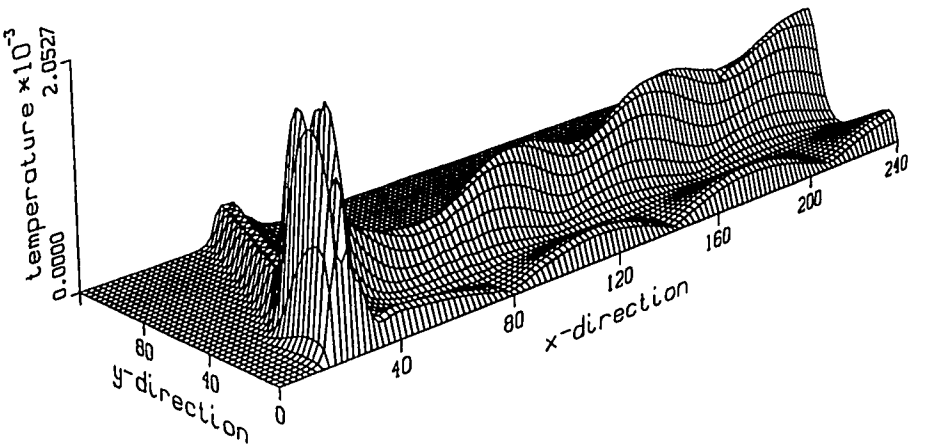

Figure 61: first harmonic of T at $v_{\max} = 0.0004$ for case 3

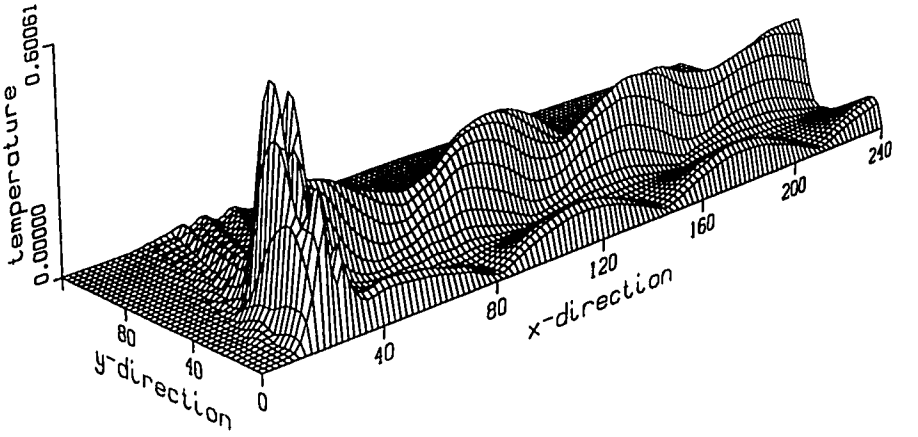

Figure 62: first harmonic of T at $v_{\max} = 0.125$ for case 3

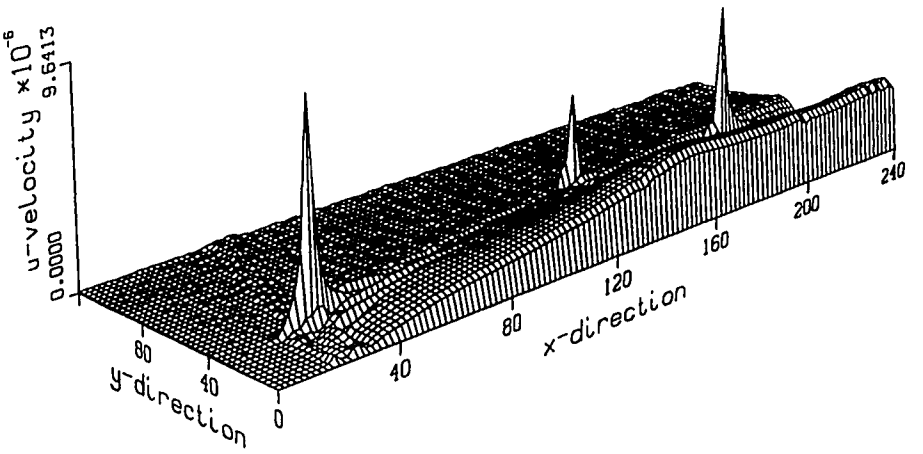

Figure 63: second harmonic of u at $v_{\max} = 0.0004$ for case 3

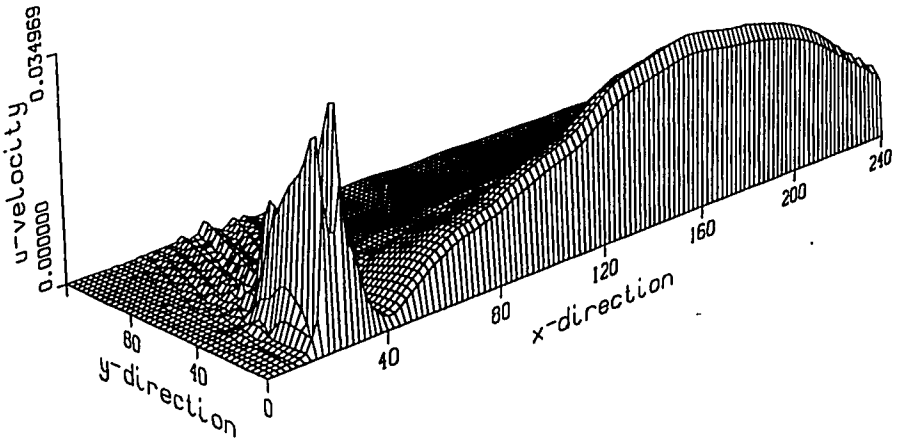

Figure 64: second harmonic of u at $v_{\max} = 0.125$ for case 3

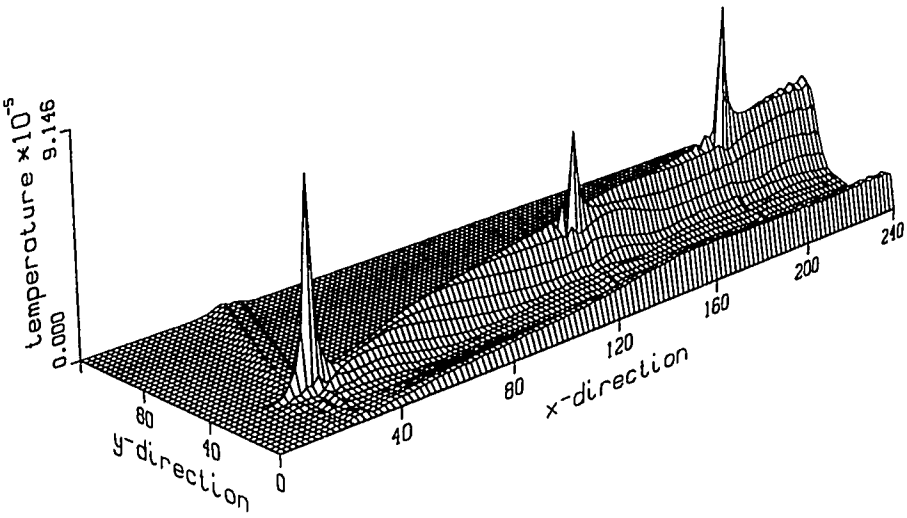

Figure 65: second harmonic of T at $v_{\max} = 0.0004$ for case 3

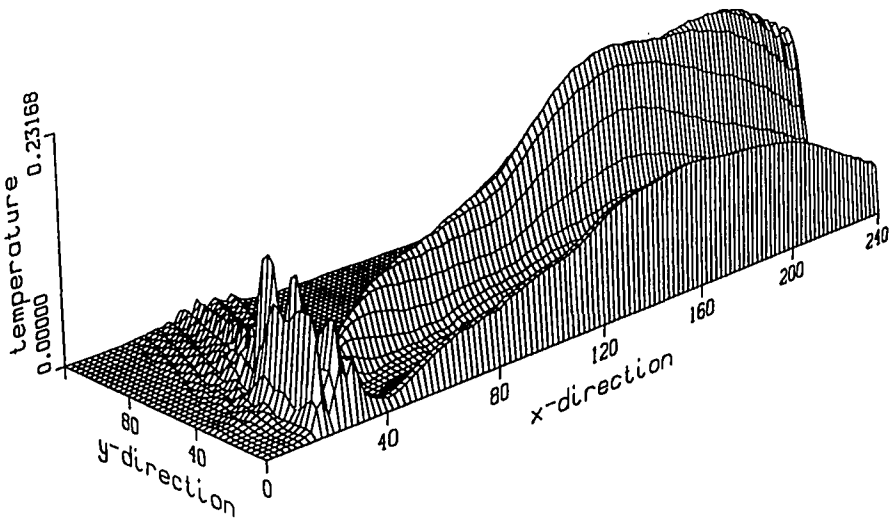

Figure 66: second harmonic of T at $v_{\max} = 0.125$ for case 3

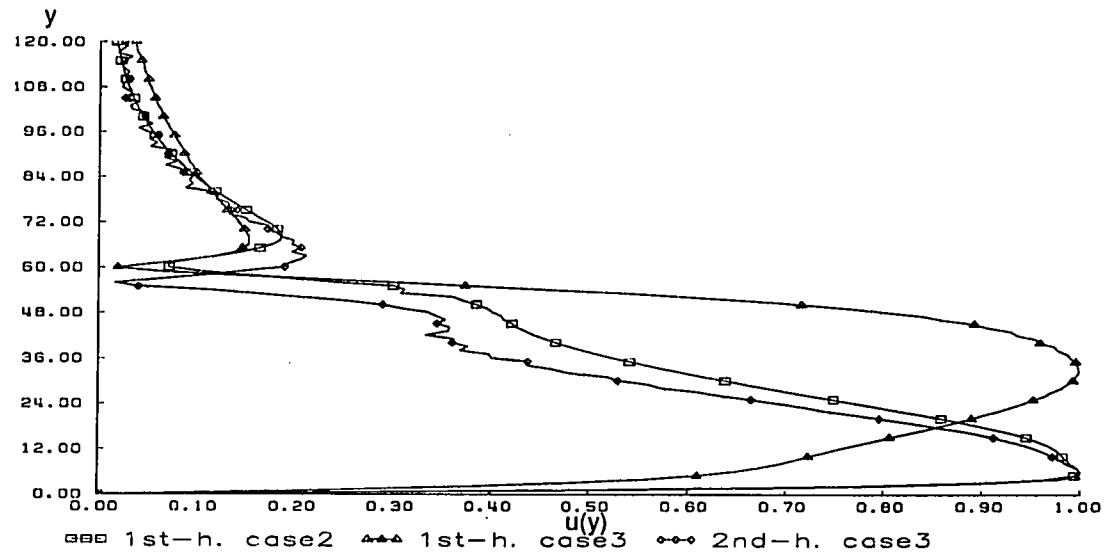

Figure 67: $u(y)$ of case 2 and 3 at $v_{\max} = 0.0004$

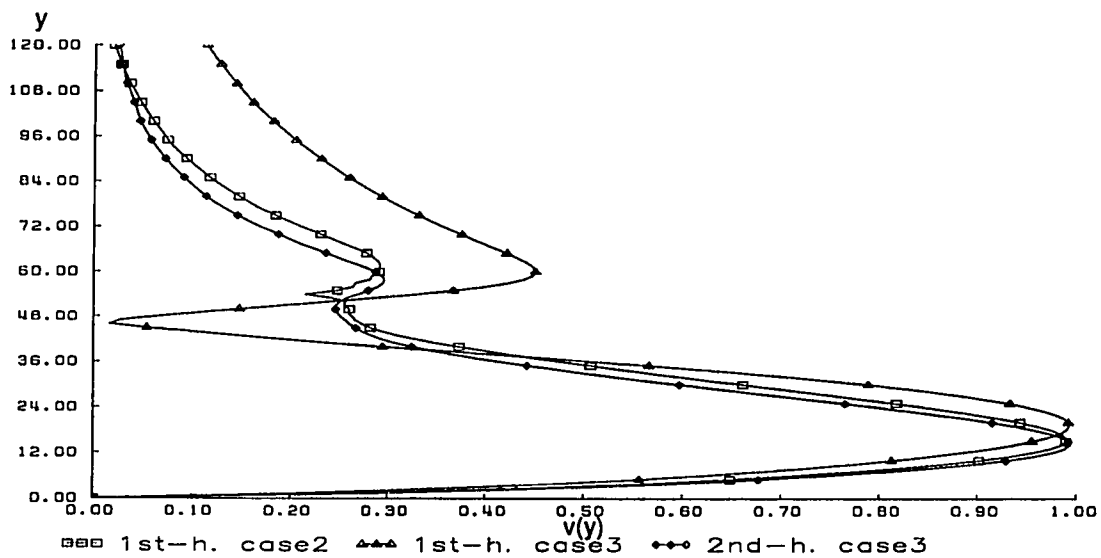

Figure 68: $v(y)$ of case 2 and 3 at $v_{\max} = 0.0004$

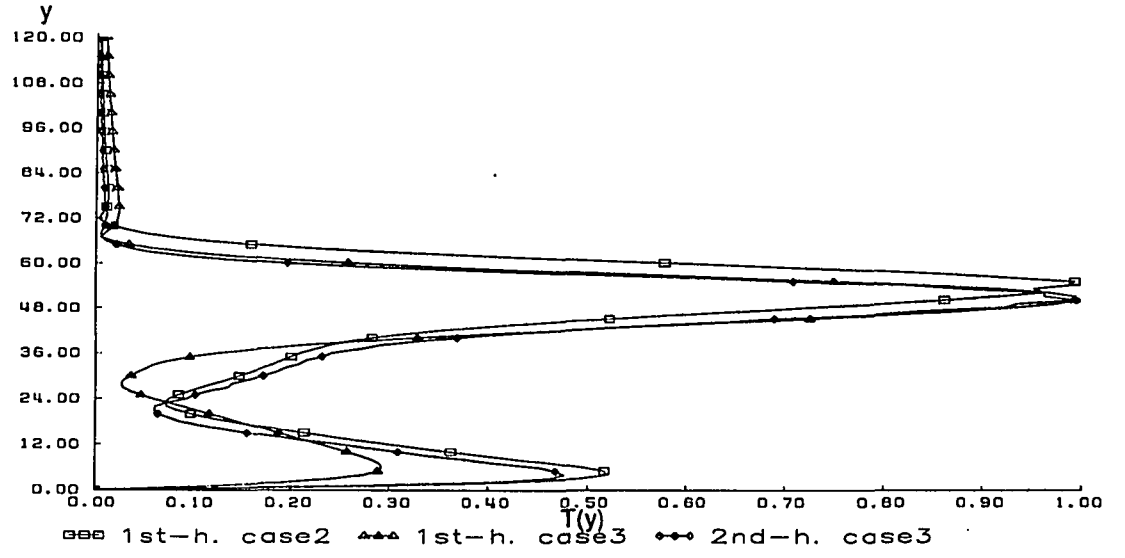

Figure 69: $T(y)$ of case 2 and 3 at $v_{\max} = 0.0004$

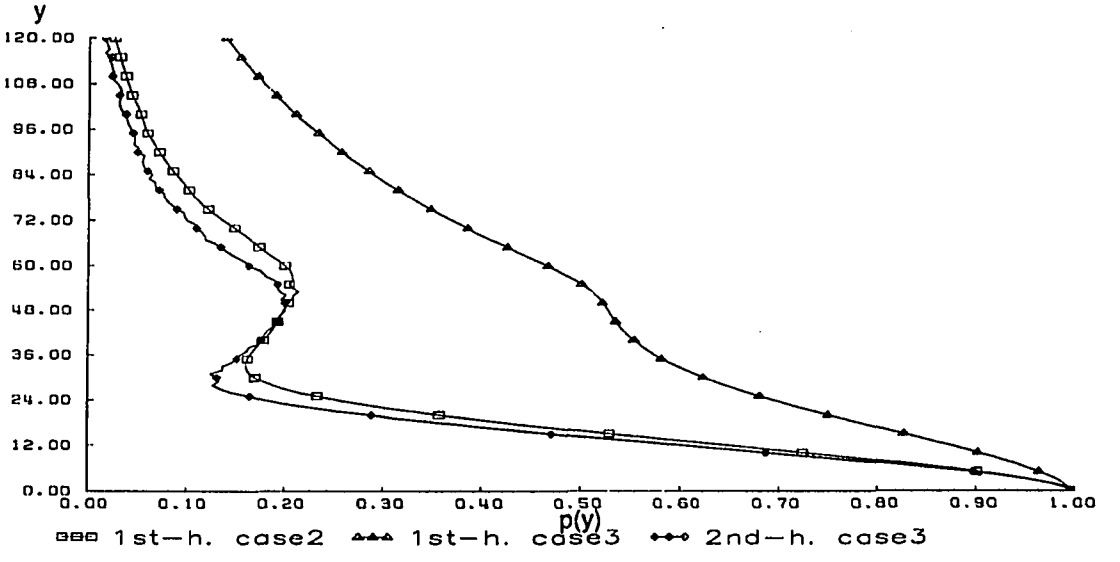

Figure 70: $p(y)$ of case 2 and 3 at $v_{\max} = 0.0004$

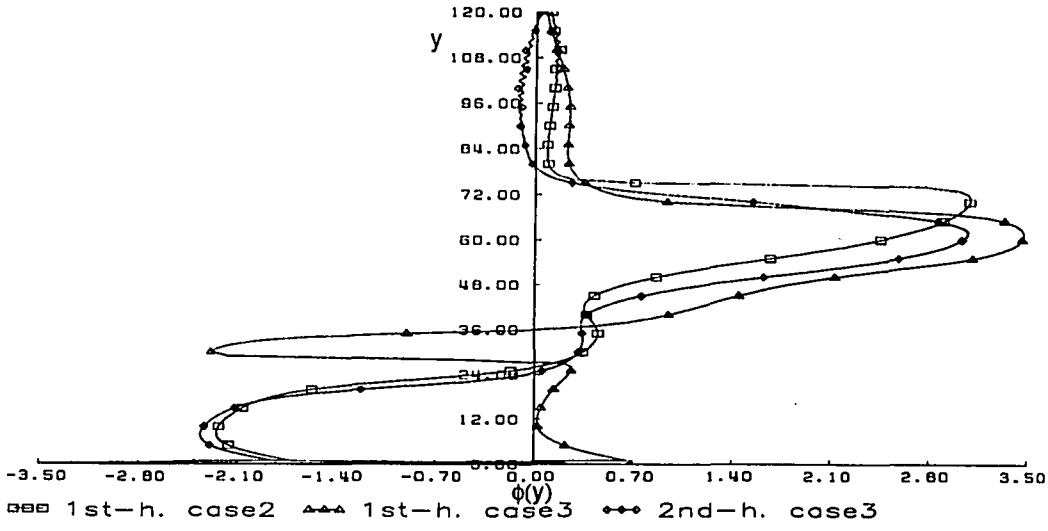

Figure 71: phase of $T(y)$ for case 2 and 3 at maximum amplitude level

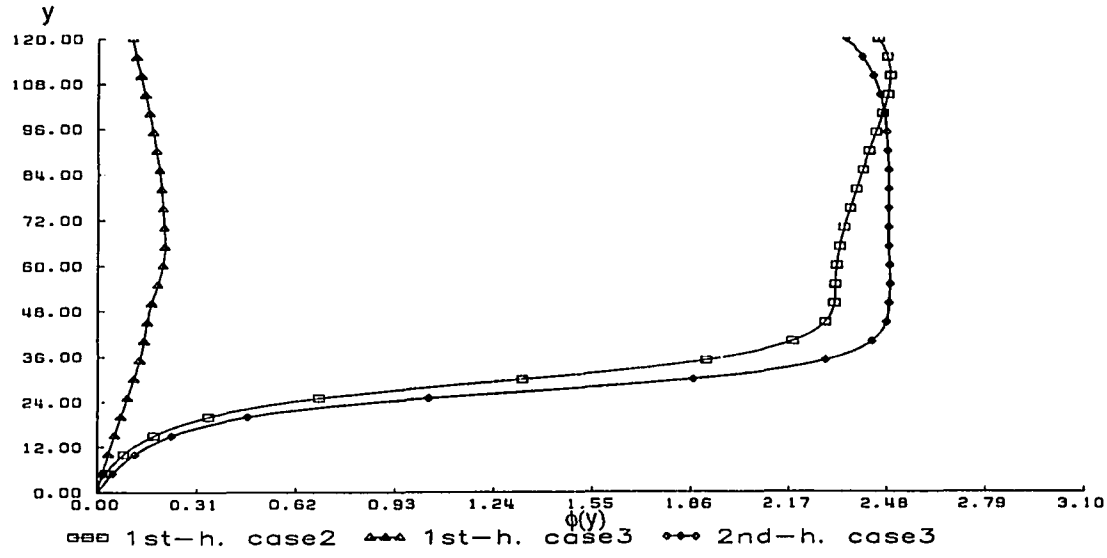

Figure 72: phase of $p(y)$ for case 2 and 3 at maximum amplitude level

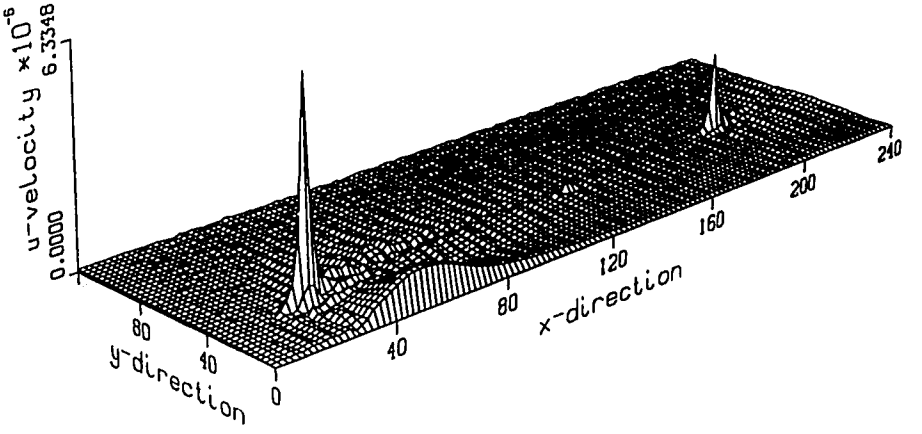

Figure 73: third harmonic of u at $v_{\max} = 0.0004$ for case 3

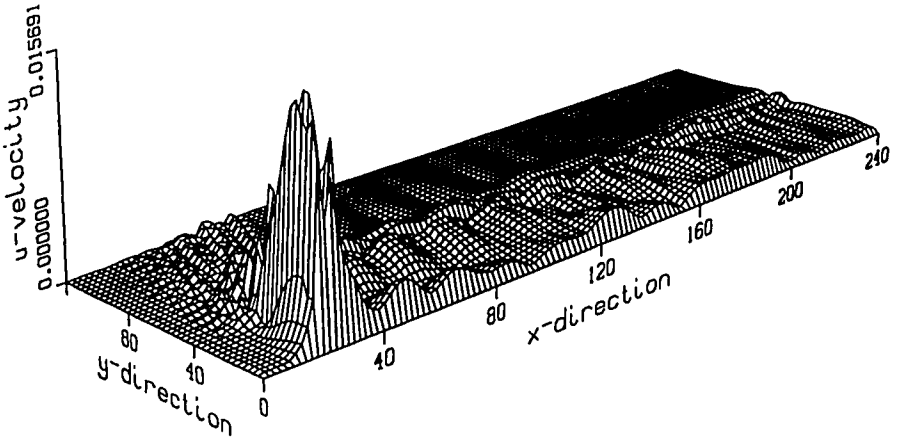

Figure 74: third harmonic of u at $v_{\max} = 0.125$ for case 3

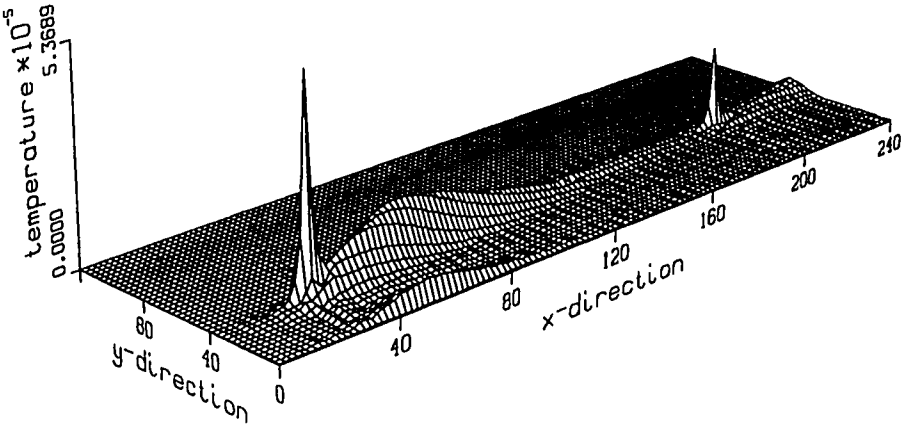

Figure 75: third harmonic of T at $v_{\max} = 0.0004$ for case 3 .

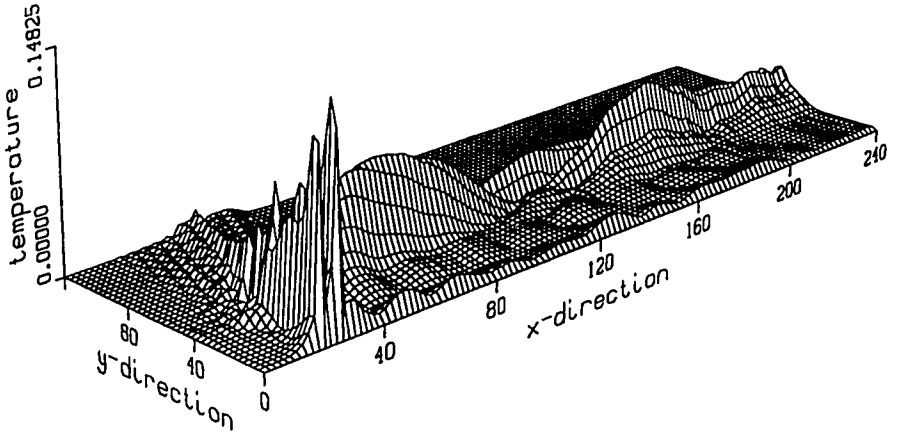

Figure 76: third harmonic of T at $v_{\max} = 0.125$ for case 3

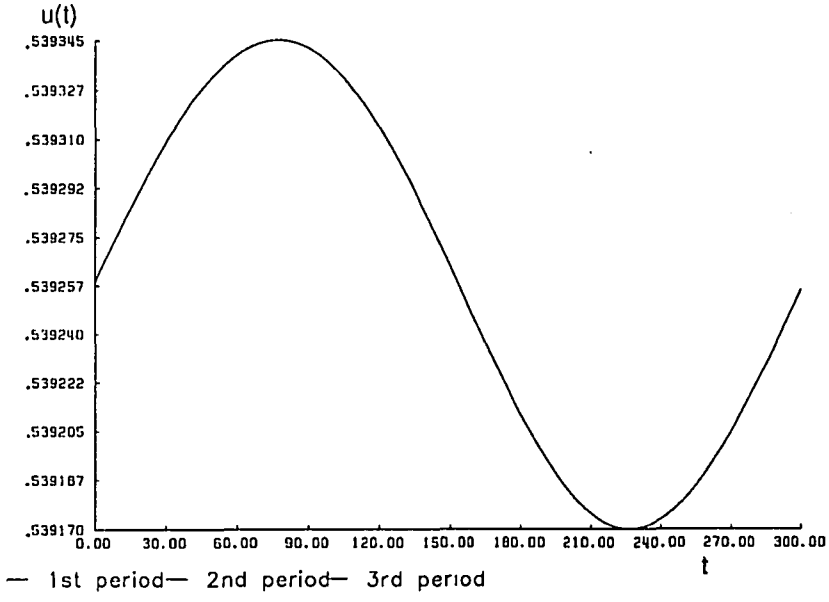

Figure 77: signal of u' sampled at one grid point over one period in time

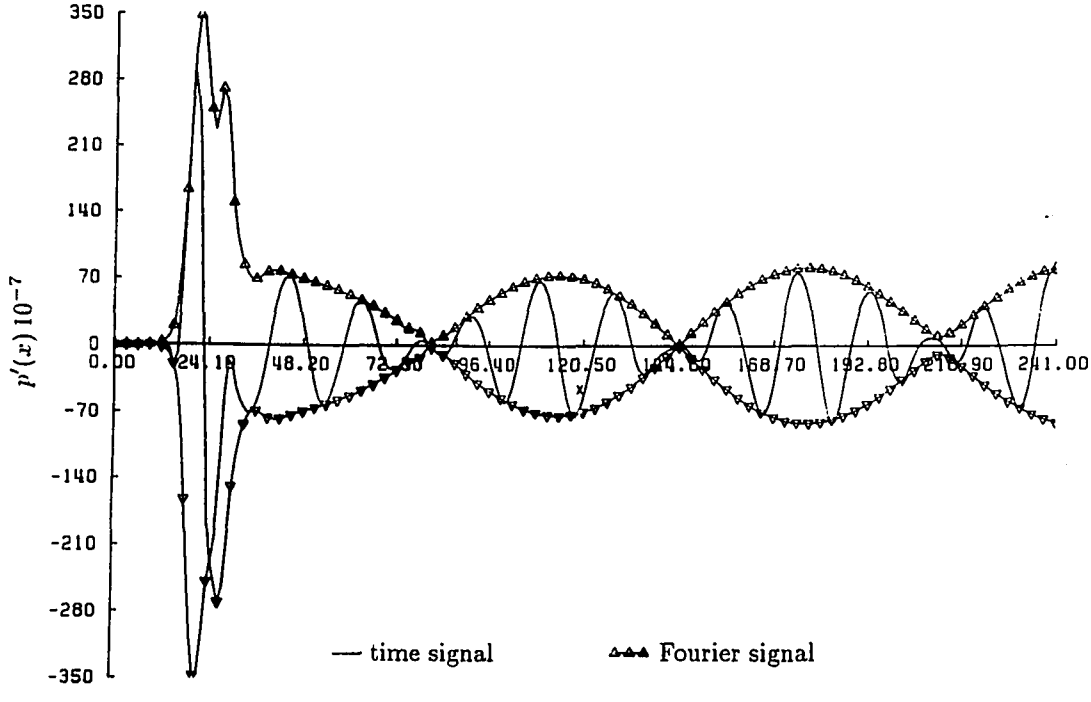

Figure 78: p' at wall from first harmonic and $t = \text{const.}$

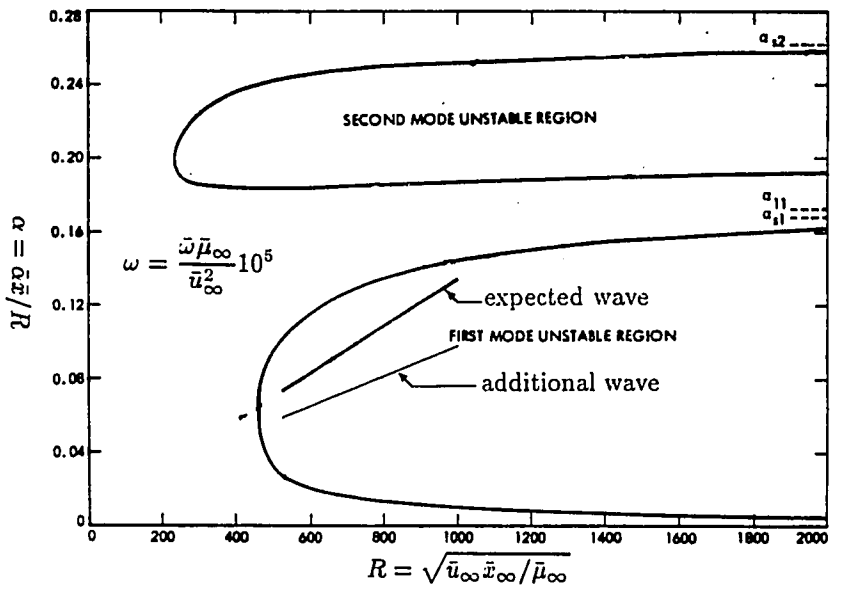

Figure 79: both waves occuring in the first harmonic of case 3 in the stability diagram

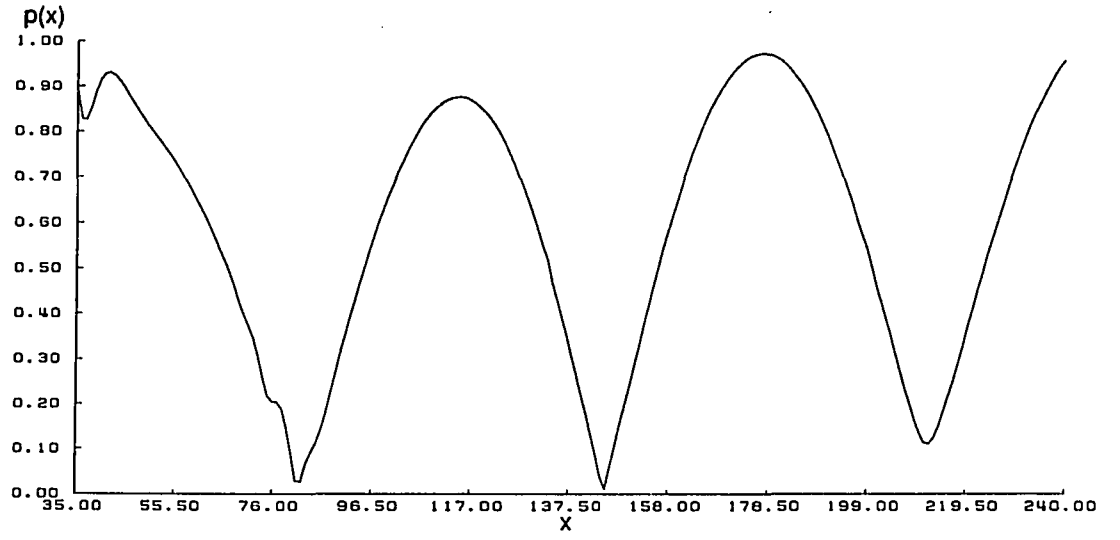

Figure 80: first harmonic of p at the wall at $v_{\max} = 0.0004$ for case 3

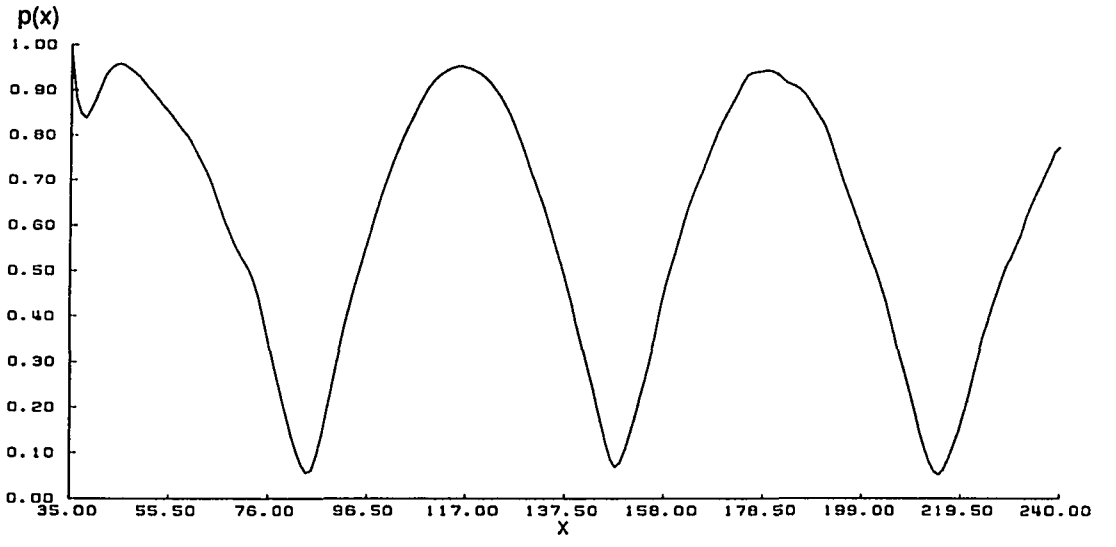

Figure 81: first harmonic of p at the wall at $v_{\max} = 0.125$ for case 3

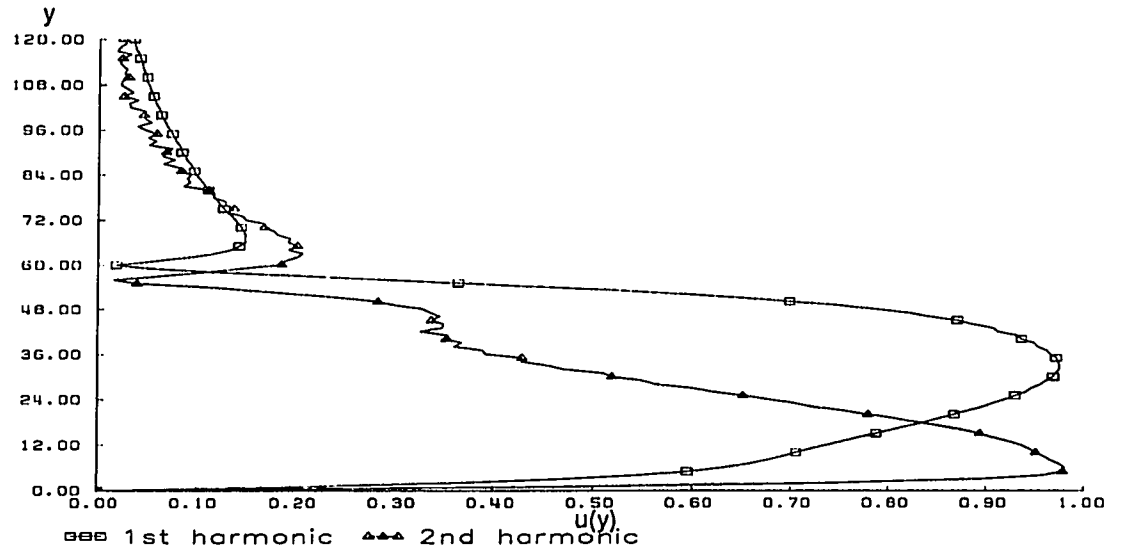

Figure 82: $u(y)$ at grid line 180 for $v_{\max} = 0.0004$ (case 3)

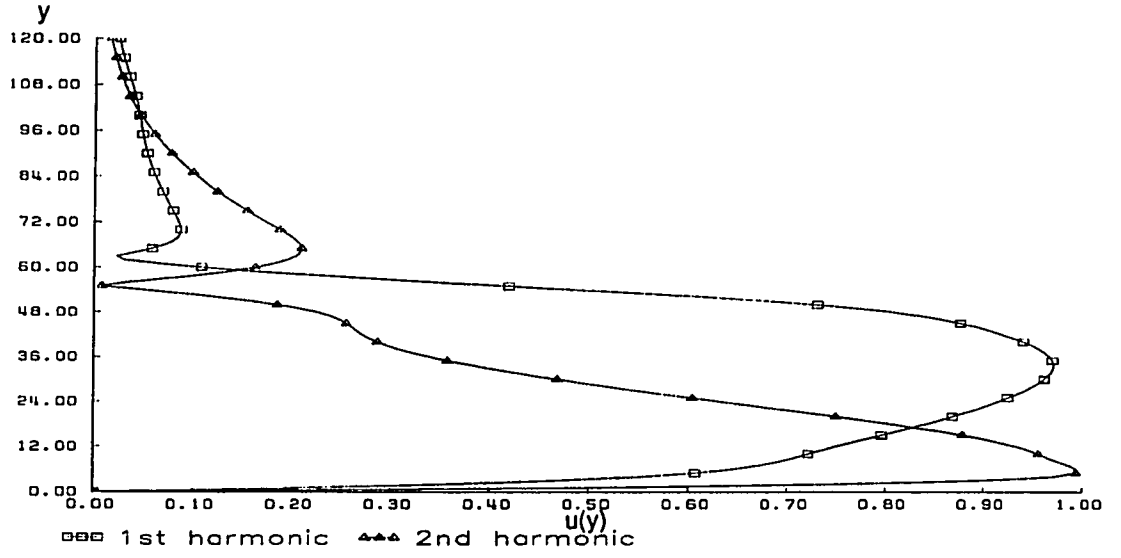

Figure 83: $u(y)$ at grid line 180 for $v_{\max} = 0.125$ (case 3)

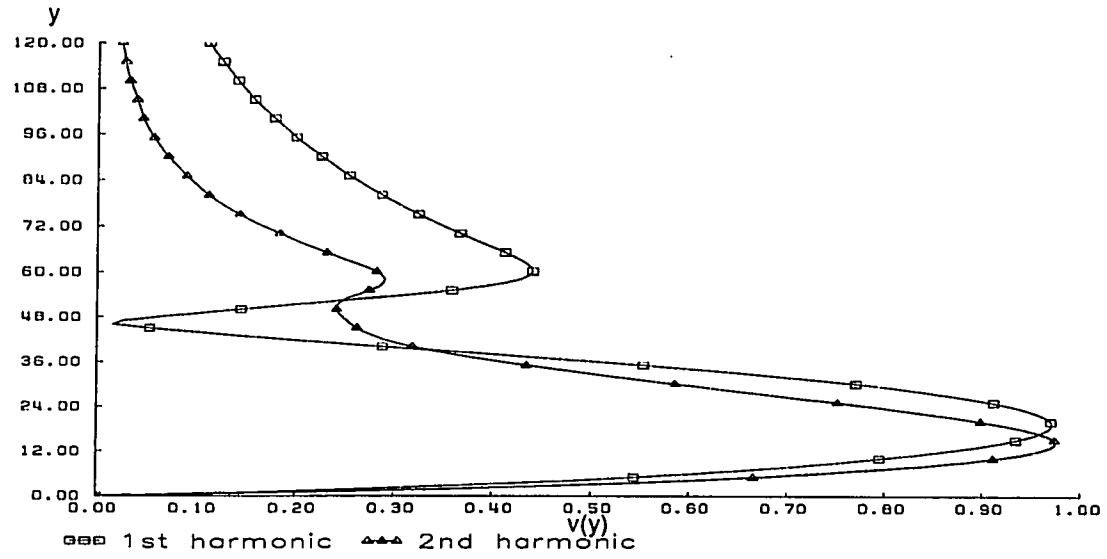

Figure 84: $v(y)$ at grid line 180 for $v_{\max} = 0.0004$ (case 3)

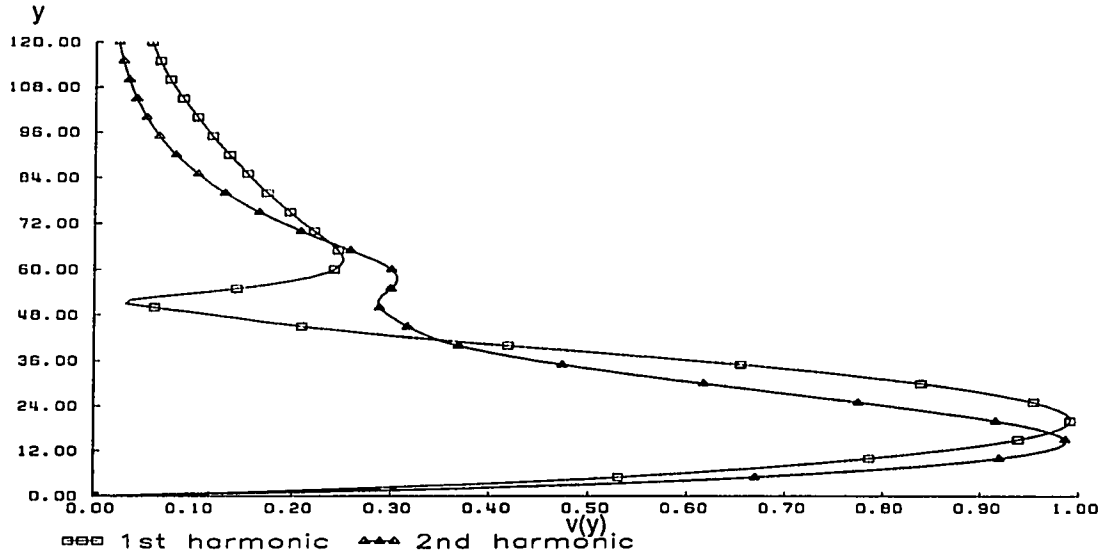

Figure 85: $v(y)$ at grid line 180 for $v_{\max} = 0.125$ (case 3)

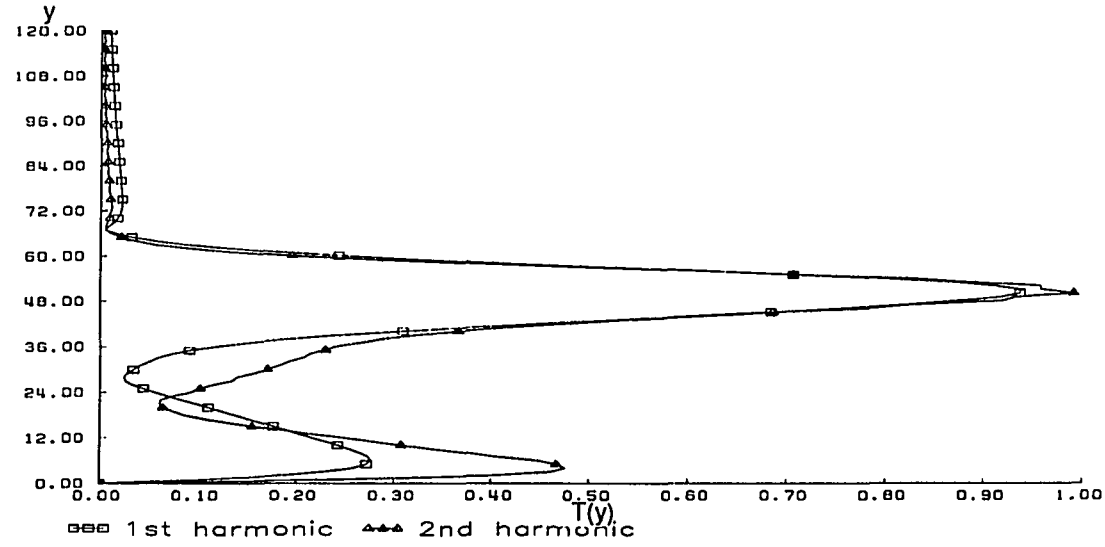

Figure 86: $T(y)$ at grid line 180 for $v_{\max} = 0.0004$ (case 3)

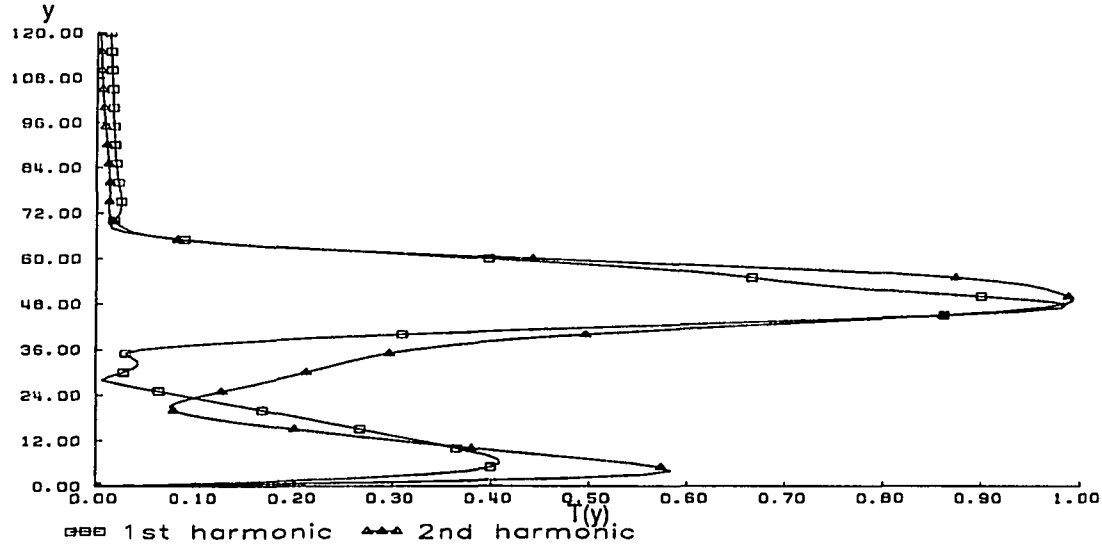

Figure 87: $T(y)$ at grid line 180 for $v_{\max} = 0.125$ (case 3)

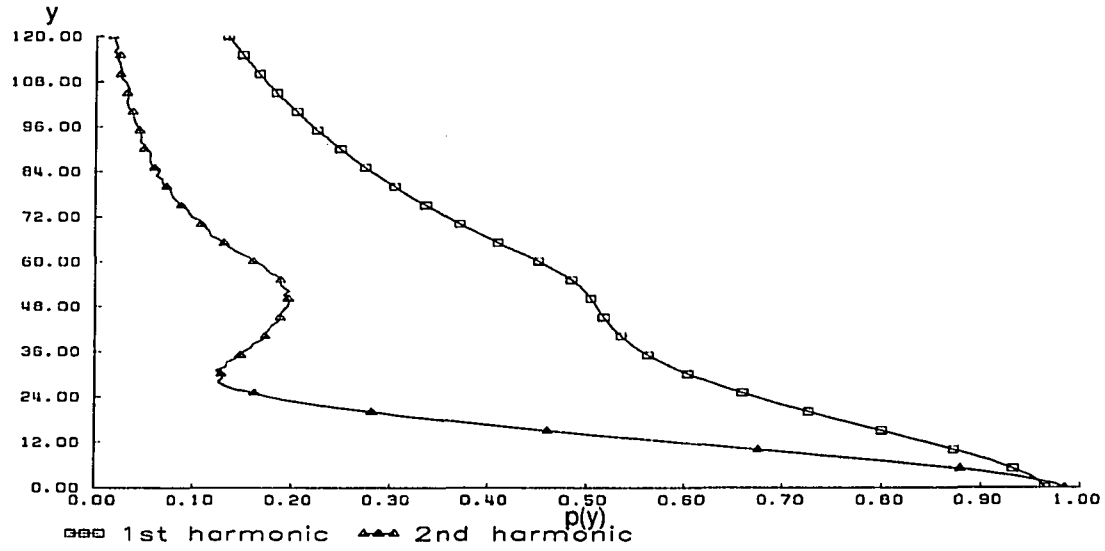

Figure 88: $p(y)$ at grid line 180 for $v_{\max} = 0.0004$ (case 3)

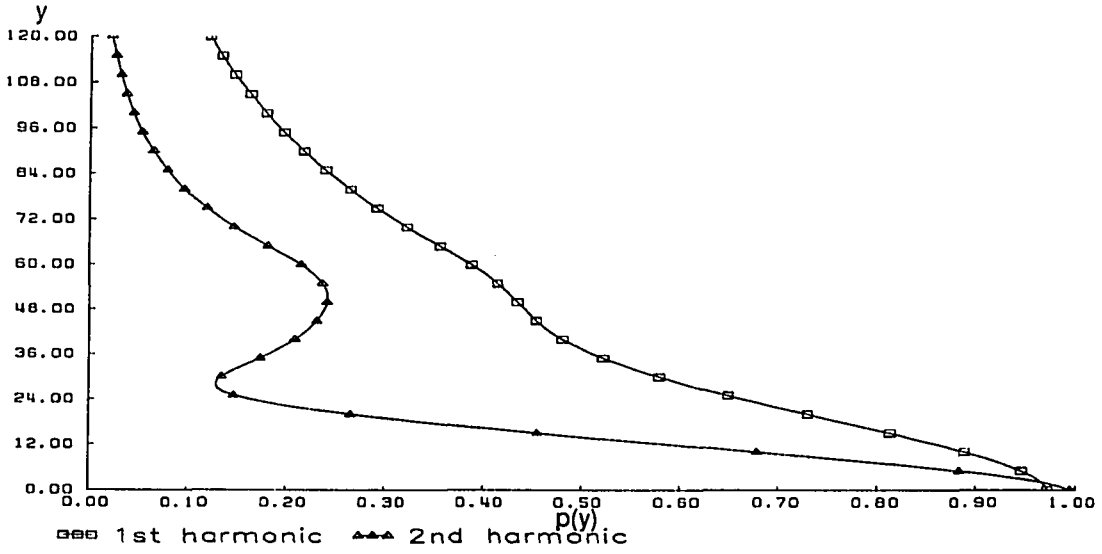

Figure 89: $p(y)$ at grid line 180 for $v_{\max} = 0.125$ (case 3)

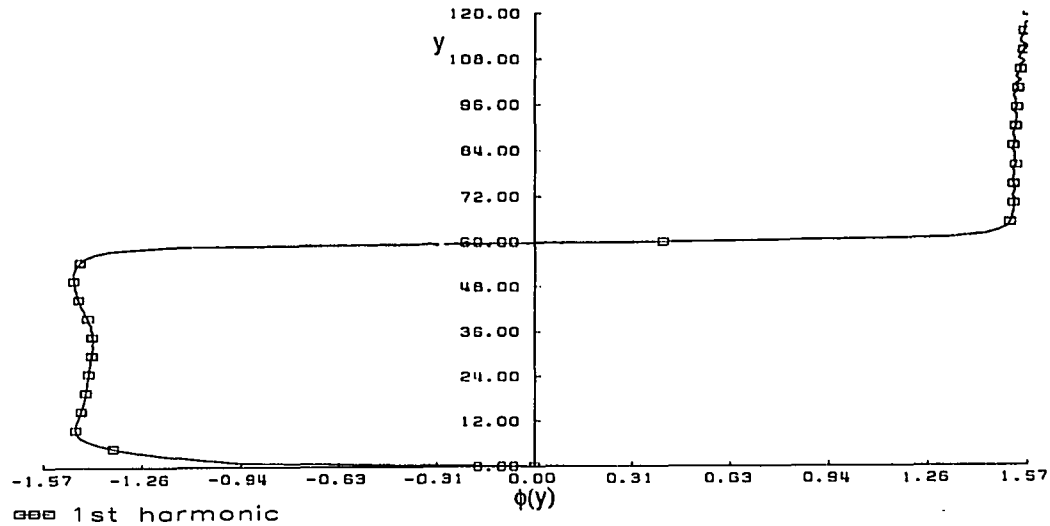

Figure 90: phase of $u(y)$ at grid line 180 for $v_{\max} = 0.0004$ (case 3)

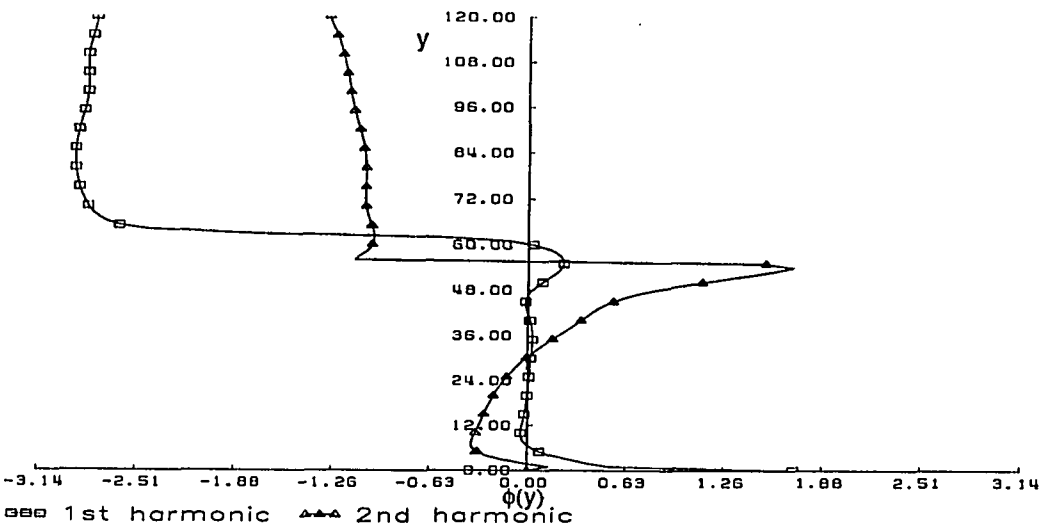

Figure 91: phase of $u(y)$ at grid line 180 for $v_{\max} = 0.125$ (case 3)

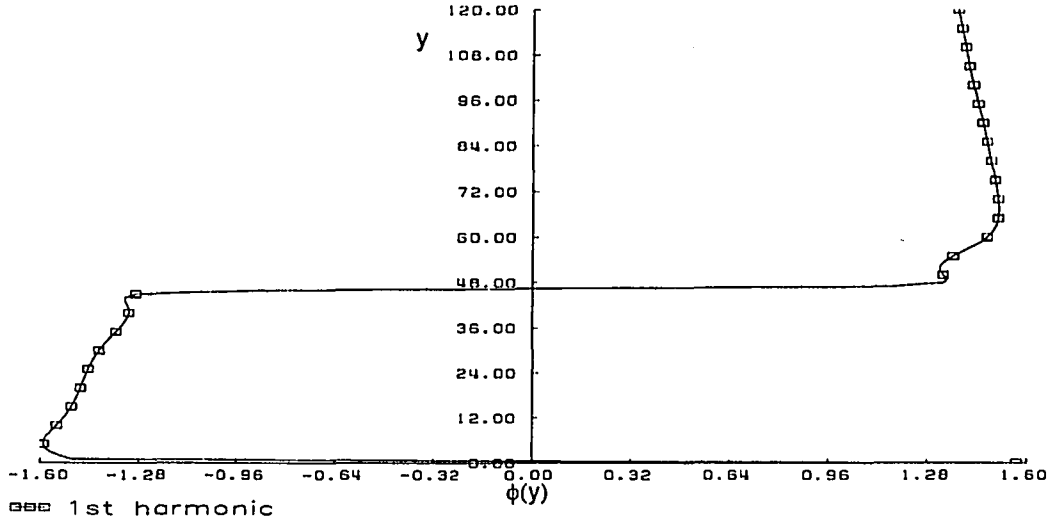

Figure 92: phase of $v(y)$ at grid line 180 for $v_{\max} = 0.0004$ (case 3)

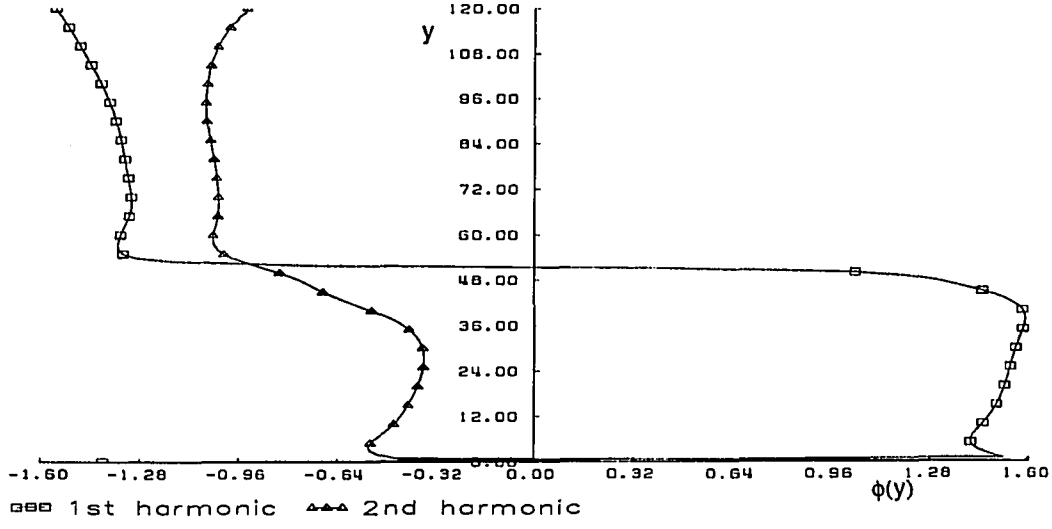

Figure 93: phase of $v(y)$ at grid line 180 for $v_{\max} = 0.125$ (case 3)

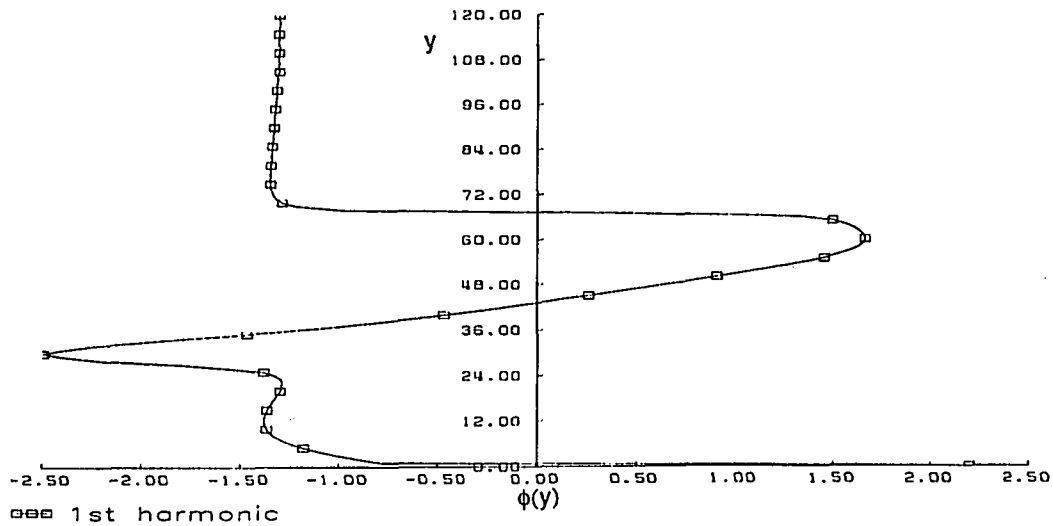

Figure 94: phase of $T(y)$ at grid line 180 for $v_{\max} = 0.0004$ (case 3)

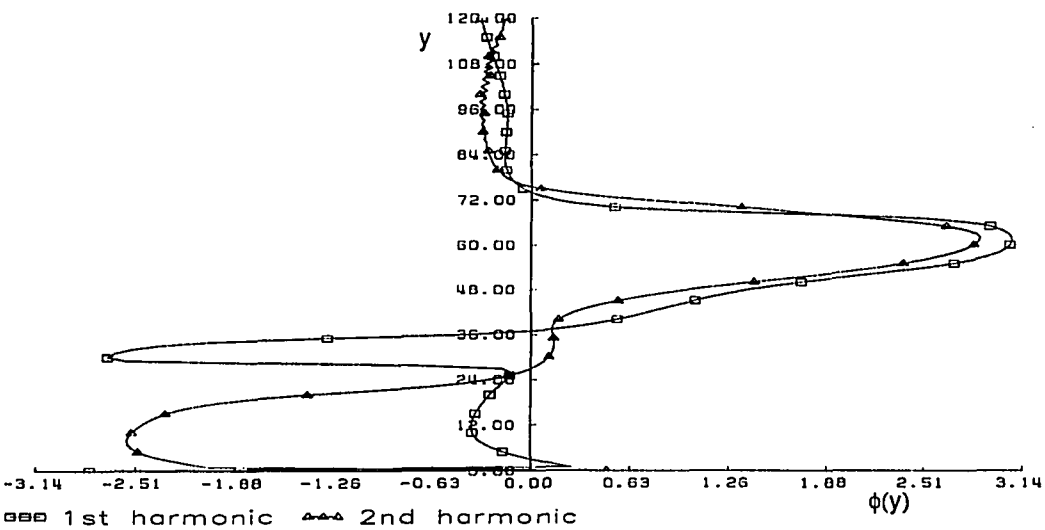

Figure 95: phase of $T(y)$ at grid line 180 for $v_{\max} = 0.125$ (case 3)

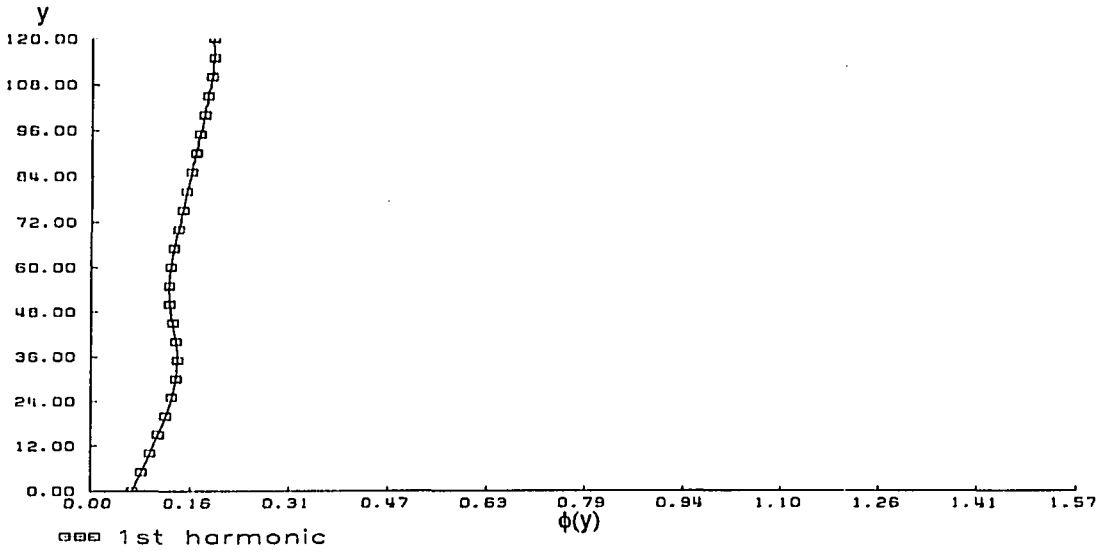

Figure 96: phase of $p(y)$ at grid line 180 for $v_{\max} = 0.0004$ (case 3)

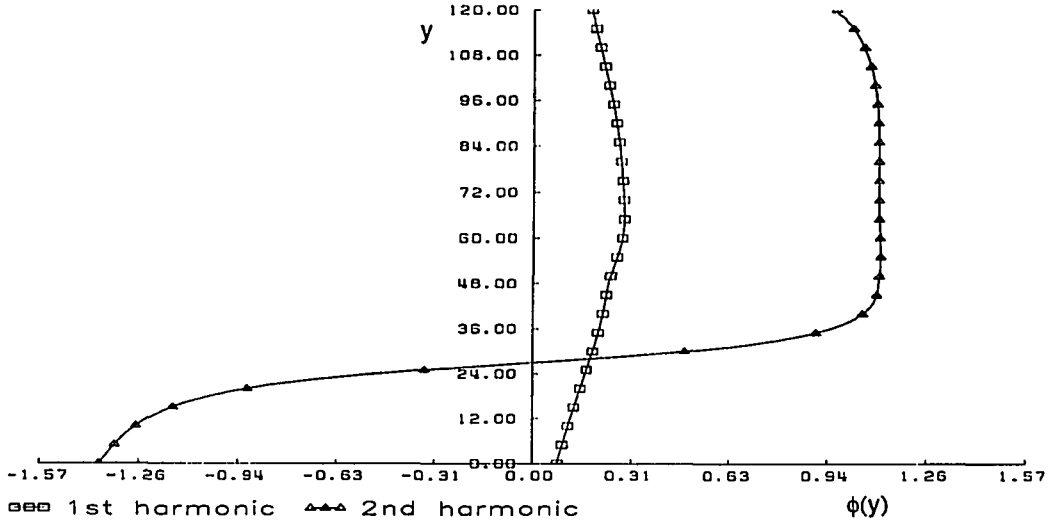

Figure 97: phase of $p(y)$ at grid line 180 for $v_{\max} = 0.125$ (case 3)

LIST OF REFERENCES

[1] Leslie M. Mack. Boundary layer stability. Technical Report Document No. 900-277, Rev. A, Jet Propulsion Laboratory, Pasadena, California, 1969.

[2] Leslie M. Mack. Review of linear compressible stability theory. In M. Y. Hussaini D. L. Dwoyer, editor, *Stability of Timedependent and Spatially Varying Flows*, pages 164 – 187. Springer, New York, 1985.

[3] Andreas Thumm. *Numerische Untersuchungen zum laminar-turbulenten Strömungsumschlag in transsonischen Grenzschichtströmungen.* PhD thesis, Universität Stuttgart, 1991.

[4] Werner Wolz, Institut für Aerodynamik und Gasdynamik, Universität Stuttgart. Private Communication, 1990.